

國立臺灣大學工學院材料科學與工程研究所

碩士論文

Graduate Institute of Materials Science and Engineering

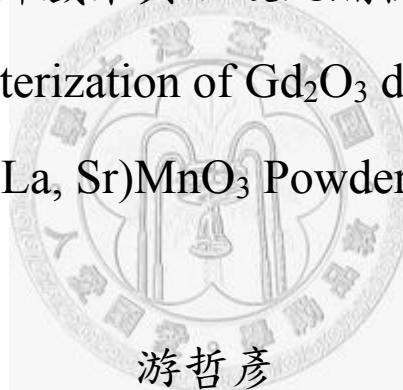
College of Engineering

National Taiwan University

Master Thesis

氧化釷添加氧化鈾纖維與錳酸鋇粉體之製備與分析

Synthesis and Characterization of  $Gd_2O_3$  doped  $CeO_2$  Fibers and  
(La, Sr) $MnO_3$  Powders



Je-Yan, Yu

指導教授：韋文誠 博士

Advisor: Wei Wen-Cheng, Ph.D.

中華民國97年7月

July, 2008

## 誌謝

94 年夏天，剛從台大化學系畢業的我，來到材料所這個全新的世界，開始我的碩士生涯。進入 Wei Group 這個大家庭，是我踏入這個新領域的第一步。在韋文誠老師的帶領下，接觸到了我過去從沒真正了解過的陶瓷材料，也看見了韋老師在研究上的執著與熱誠。在這豐富的研究生活中，老師不厭其煩的指導與叮嚀，甚至在論文完成的最後關鍵時刻，犧牲了自己寶貴的假日來幫助我完成論文，這些舉動無不讓我感動萬分。對於老師，我除了感激之外還是感激！另外，也要感謝林唯芳教授、郭俞麟教授及洪逸明教授於百忙之中抽空參加我的口試，給予指導。您們的建議與指教，都讓我獲益匪淺。

實驗室裡的夥伴對我的幫忙與支持，都讓我在遇到困難時，能找到解決的方法。彥友學長，你一針見血的建議總讓我看清問題的癥結，也使我更懂得如何解決困難。邦英學姊，你的熱心與精湛的 TEM 技術，在我心中僅有佩服二字而已，在這裡也要祝福學姐永遠幸福。頌恩學長，身為實驗室的創意王與體育老師，你真是做的太稱職了，任何看似不可能的樣品製備或實驗，在你眼中似乎都能輕易找到成功的路徑。浚傑學長，你圓融的處事態度及應對，總是最欣賞也最希望學習的，希望你未來的博士生涯能順利而圓滿。一中學長，雖然因為工作關係無法常在實驗室，但你卻永遠關心我們的近況，也在任何困難的時刻提供協助，真是謝謝你！右儒學長，你明快的決策與積極的實驗態度實在讓我佩服，一直以來也是你提供了我各種實驗上的寶貴建議。而佳明與銘璵學長，當你們面對畢業的壓力時，仍舊能一直給予當時還是碩一的我鼓勵。函育及家嘉，兩位我碩士班的同窗，能與你們一同努力實在是我最大的榮幸，去年一起到大陸報告、出遊時共同分享的緊張與快樂時光，都是我最珍貴的回憶。嫻雯及怡如兩位學妹，總是帶給實驗室歡笑，讓實驗室的生活不至枯燥乏味，希望妳們未來都能鴻圖大展。做為實驗室裡少數擁有豐富社會經驗的夥伴，居諭你所給予的眾多建議實在是惠我良多，也讓我對即將來臨的新生活有了更充分的準備。永遠都在用功的勤文、隨

時都認真工作的士岳、總是努力又看不準猜不透的敬閔，以及新進的研究生智淵還有專題生東祐，實驗室的未來還要靠你們努力，希望你們一切順利。另外，在我碩士生涯之初，給予我許多幫助的馨怡學姐及仁彰學長，也祝福你們未來一帆風順，在電腦模擬的領域發光發熱。

材料系辦的李玉玲小姐、林由莉小姐、呂碧玲小姐、周麗美小姐及張瑛梅小姐，謝謝妳們在行政事務上一直給予的眾多幫忙。材料系的李苑慈學姊、陳學人學長及高崇源學長，謝謝你們在儀器上的各項幫忙及協助，讓我能順利的取得實驗數據。鶯歌陶瓷中心的沈俊良先生及陳彥涵小姐，你們實在提供了太多我實驗中所需的分析儀器及分析技巧，謝謝你們過去這段時間的協助。鴻昇爐業的李老闆，一直以來你都是我爐子使用上發生問題時最可靠的求救對象。永成白鐵行的陳老闆，你的熱心我將永遠記在心裡，希望你兒子在未來大學四年的學生生涯能一切順利。

最後，當然要感謝我的家人。你們的支持一直是我能專心於學業的最大支柱，讓我沒有後顧之憂，能全力在這裡衝刺，謝謝你們。



## 摘要

在本研究中，選擇了兩種固態氧化物燃料電池的內部元件及一種單電池進行其製備及分析。

首先，利用化學共沉法合成氧化釷添加氧化鈷(GDC)之纖維。由於其較高的導電性，異價離子添加的氧化鈷是取代目前常見的釷安定氧化鋯(YSZ)電解質的適當材料。合成的 GDC 纖維透過 SEM、TEM、DTA/TG、XRD 及 ICP-AES 等技術進行其化學，結晶動力學及微結構等性質的分析。結果顯示纖維之合成過程屬於零級反應。且所合成之析出物的微結構會因檸檬酸及氫氧化鈉濃度之添加量不同而有所影響。除了纖維之外，膠粒、柱狀及片狀之析出物亦可透過不同比例之檸檬酸及氫氧化鈉濃度產生。

其次，當做固態氧化物燃料電池的陰極材料錳酸鋇鏷(LSM)，透過兩種溶膠凝膠法合成而得。其一為 Pechini 法，其二則是以聚丙烯酸(PAA)做為高分子添加劑的溶膠凝膠法。除了上述的分析技術，所合成之粉末也以 SEM-EDS 之技術進行全定量分析以得知其化學成分之分布。同時，LSM 粉體終於熱處理過程中所殘餘之碳含量則以碳硫分析儀進行分析，並以三點直流方式測定 LSM 與 YSZ 間之介面電阻。

最後，電解質支撐之固態氧化物燃料電池也於此研究中製備。透過網印技術，LSM 陰極薄膜及氧化鎳/氧化鋯(NiO/YSZ)陽極薄膜成功的披覆於氧化鋯的電解質支撐上。此氧化鋯電解質之電性利用交流阻抗分析儀進行分析。最後也報導所製備的三層燃料電池之單電池微結構。

**關鍵字：**固態氧化物燃料電池、電解質、氧化釷添加氧化鈷、纖維、化學共沉法、反應動力學、陰極、錳酸鋇鏷、Pechini 法、溶膠凝膠法



## Abstract

This study, two components in solid oxide fuel cell (SOFC) and one cell were fabricated and analyzed. First, fibrous  $\text{Gd}_2\text{O}_3$  doped ceria (GDC), which is the alternative material for electrolyte, was synthesized by chemical co-precipitate method. The chemical, growth and microstructural properties of the GDC fibers were characterized by scanning and transmission electron microscopies (SEM and TEM), differential thermogravimetry (DTA/TG), X-ray diffraction (XRD), and inductive coupling plasma-atomic emission spectroscopy (ICP-AES) technologies. The results of fiber synthesis reaction showed zero-order kinetics. The morphologies were closely affected by the concentrations of additives, citric acid and sodium hydroxide. Three types of morphologies, including spherical colloids, fibers, stick-in-bundles, and flakes could be synthesized by control the ratio of citric acid and sodium hydroxide.

Second, LSM powders were synthesized by Pechini method and a sol-gel process with PAA as chelating agent. Besides the analysis technologies mentioned above, the powders were also characterized by quantitative energy dispersive spectroscopy (EDS) to identify their compositional homogeneity. In addition, the residual carbon content in the LSM powders and their electrical resistance of the LSM/YSZ interface were also analyzed by carbon/sulfur analyzer and 3-terminal measurement, respectively.

Finally, an electrolyte supported SOFC was fabricated by screen printing. The electrical conductivity of 8Y-YSZ electrolyte analyzed by AC impedance and the microstructure of the tri-layer single cell were prepared and characterized.

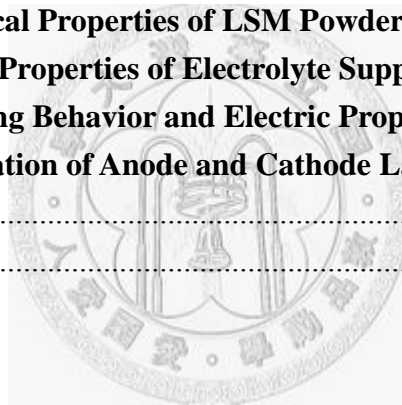
**Keywords:** SOFC, electrolyte, GDC, fiber, co-precipitation, reaction kinetics, cathode, LSM, sol-gel method, Pechini method



## Content

List of Figures .....	VI
List of Tables .....	X
Chapter 1 Introduction .....	1
Chapter 2 Literature Review .....	4
2.1 Electric Conductive Cerium Oxide .....	4
2.2 Synthesis of Oxide Fibers .....	11
2.2.1 AAO Template .....	11
2.2.2 Hydrothermal Precipitation .....	12
2.2.3 Electrospinning .....	13
2.2.4 Precipitation Method .....	16
2.3 Electrical Properties of Cerium Oxide .....	20
2.3.1 Theory of Oxygen Transport .....	20
2.3.2 Dopant Effect .....	22
2.3.3 Grain Boundary/Impurity Effects .....	27
2.3.4 Reduction Behavior of Ceria .....	28
2.4 Cathode Materials for SOFC .....	39
2.4.1 LaMnO <sub>3</sub> Materials .....	40
2.4.2 Synthesis of LSM Powders .....	42
Chapter 3 Experimental .....	46
3.1 Materials .....	46
3.2 Synthesis of Doped/Undoped Ceria Fibers .....	47
3.3 Fabrication of Cathode Powders .....	48
3.3.1 Sol-Gel Synthesis .....	48
3.3.2 Pechini Method .....	49
3.4 Single Cell Fabrication .....	49
3.4.1 Fabrication of Dense YSZ Thin Plate .....	49
3.4.2 Anode and Cathode Thin Film Fabrication .....	50
3.5 Characterization .....	50
3.5.1 ICP-AES Analysis .....	50
3.5.2 Density Measurement .....	51
3.5.3 Thermal Analysis .....	52
3.5.4 BET Measurement .....	53
3.5.5 Residual Carbon Analysis .....	53
3.5.6 Microstructural Analysis and Phase Identification .....	54
(1) SEM Observation .....	54

(2) TEM Observation .....	55
3.5.7 XRD Analysis .....	56
3.5.8 Electrical Properties Measurement.....	56
(1) DC Electrical Measurement.....	56
(2) Electrochemical Impedance Spectroscopy Measurement.....	58
<b>Chapter 4 Results and Discussions.....</b>	<b>68</b>
<b>4.1 Synthesis of CeO<sub>2</sub> (GDC and SDC) Fibers.....</b>	<b>68</b>
4.1.1 Effects of Sodium Hydroxide/Citric Acid .....	68
4.1.2 Kinetic Analysis of Fiber Synthesis .....	70
4.1.3 Morphology Evolution by Thermal Treatment.....	74
<b>4.2 Properties of LSM Powders.....</b>	<b>96</b>
4.2.1 Phase Formation of LSM.....	96
4.2.2 Quantitative Analysis of Composition .....	98
4.2.3 Reduction of Surface Area .....	100
4.2.4 Electrical Properties of LSM Powders .....	101
<b>4.3 Fabrication and Properties of Electrolyte Supported SOFC Single Cell.....</b>	<b>121</b>
4.3.1 Sintering Behavior and Electric Properties of 8YSZ Plate.....	121
4.3.2 Fabrication of Anode and Cathode Layers .....	123
<b>Chapter 5 Conclusions .....</b>	<b>131</b>
<b>References.....</b>	<b>134</b>



## List of Figures

Fig. 2.1	(a) Fluorite structure, $\text{CeO}_2$ structure of showing (b) oxygen ion and (c) cerium ion is selected as the original point, respectively. ....	8
Fig. 2.2	Temperature depend electrical conductivities of 8YSZ, 8YSZ in dry $\text{O}_2$ , 20GDC, LSGM and $\text{Bi}_3\text{NbO}_7\text{-Bi}_3\text{YO}_6$ , the dotted curve presents the electrical conductivity equal to 0.01 S/cm. Guo measured the 8YSZ sample in dry oxygen atmosphere, instead of air atmosphere.....	9
Fig. 2.3	Fluorite structure with one host cation replaced by a lower-valent cation, and created an oxygen vacancy. ....	10
Fig. 2.4	Scheme of electrospinning of ceramic fibers. ....	19
Fig. 2.5	Vacancy concentration dependence of the ionic conductivity from Eq. (8)...	33
Fig. 2.6	Ionic conductivity of aliovalent doped ceria at $800^\circ\text{C}$ against the radius of dopant cation. ....	34
Fig. 2.7	(a) Calculated binding energy of trivalent substitutional ions to an oxygen vacancy, (b) configuration of first, second and third neighbor oxygen vacancies with respect to the substitutional trivalent ion in a unit cell. ....	35
Fig. 2.8	Electrical conductivity of (a) pure ceria and (b) 20GDC system against oxygen partial pressure at different temperature .....	36
Fig. 2.9	Dopant radius dependence $P_{\text{O}_2}^*$ ( $t_i = 0.5$ ) of doped ceria with rare-earth dopant. ....	38
Fig. 3.1	Experimental flowchart of GDC fiber synthesis. ....	59
Fig. 3.2	Experimental flowchart of LSM powder synthesized by sol-gel process with PAA as gelling agent.....	63
Fig. 3.3	Experimental flowchart of LSM powder synthesized by Pechini method. ....	64
Fig. 3.4	(a) Top view of the electrodes, and (b) side view of the configuration scheme of 3-terminal electrical measurement. ....	65
Fig. 3.5	Thermal treatment procedures of LSM powders. All the treatment was conducted in atmosphere. The procedure of P-LSM and A-LSM was $2^\circ\text{C}/\text{min}$ to $400^\circ\text{C}$ , than holding for 1 hr. The ramp rate of P-LSM-S and A-LSM-S was $1^\circ\text{C}/\text{min}$ , and the isothermal treatment was 1 hr at $300^\circ\text{C}$ for P-LSM-S and 3 hr at $200^\circ\text{C}$ for A-LSM-S. ....	66
Fig. 3.6	Block diagram (original code) of 3-terminal electrical measurement monitoring software. ....	67
Fig. 4.1	Schematic diagram showing the change of reacting solution growing (a)	

	fibrous, (b) flake-shape, and (c) stick-in-bundle precipitates.....	78
Fig. 4.2	As-prepared cerium hydrocarbonate precipitates with the $[\text{NaOH}]/[\text{C}_6\text{H}_8\text{O}_7]$ ratio equal to (a) 0.8, in a flake shape, (b) 0.2, in a shape of stick-in-bundle. The solutions were aged at $90^\circ\text{C}$ for 24 hr. ....	79
Fig. 4.3	Concentration of $[\text{NaOH}]$ and $[\text{C}_6\text{H}_8\text{O}_7]$ illustrating the resulted morphologies of cerium hydrocarbonate precipitates aged at $90^\circ\text{C}$ for 24 hr. The starting concentration of cerium ion was (a) 0.025 m and (b) 0.1 m. In (a), the solid and dash lines represent the ratio of 0.5 and 0.8, respectively. The symbols with “*” were previous results reported by Sung. ....	80
Fig. 4.4	As-prepared cerium hydrocarbonate fibrous precipitates with a $[\text{NaOH}]/[\text{C}_6\text{H}_8\text{O}_7]$ ratio of 0.6 (sample 1) aging for (a) 12 hr and (b) 60 hr, respectively, and ratio of 0.8 (sample 15) aging for (c) 24 hr and (d) 62 hr, respectively. ....	81
Fig. 4.5	SEM micrographs showing the fibrous microstructures of 20 mol% (a) $\text{Gd}^{3+}$ doped and (b) $\text{Sm}^{3+}$ doped cerium hydrocarbonate fibers. ....	82
Fig. 4.6	Residual concentrations of $\text{Ce}^{3+}$ and $\text{Gd}^{3+}$ ions during aging period by ICP. ....	84
Fig. 4.7	Residual concentrations of $\text{Ce}^{3+}$ ions of fibrous, flake, and stick-in-bundle precipitates synthesis during aging period by ICP. The labeled numbers represent the sample numbers in Fig. 4.3. ....	85
Fig. 4.8	SEM micrographs of Gd doped cerium hydrocarbonate precipitate with (a) 2 hr, (b) 5 hr, (c) 7 hr 20 min, (d) 10 hr, (e) 12 hr, and (f) 24 hr aging period... ..	86
Fig. 4.9	Aspect ratio variation of Gd doped cerium hydrocarbonate precipitation (sample 1 in Table 3.2) against aging time. ....	87
Fig. 4.10	SEM microstructure of Gd doped cerium hydrocarbonate precipitate with 1 hr aging period, in which the specimen was sampled in D.I. water.....	88
Fig. 4.11	XRD patterns of as-prepared (a) pure cerium, (b) gadolinium doped, and (c) samarium doped hydrocarbonate fibers.....	89
Fig. 4.12	DTA/TG analysis results of GDC fibers with a ramp rate of $10^\circ\text{C}/\text{min}$ .....	90
Fig. 4.13	DTA/TG analysis results of GDC fibers with a ramp rate of $3^\circ\text{C}/\text{min}$ to (a) $220^\circ\text{C}$ and (b) $200^\circ\text{C}$ , then holding for 1 hr. ....	91
Fig. 4.14	XRD patterns of GDC fibers thermal treated at (a) $200^\circ\text{C}$ , (b) $300^\circ\text{C}$ , (c) $400^\circ\text{C}$ , and (d) $600^\circ\text{C}$ for 1 hr. ....	92
Fig. 4.15	(a) BF image and (b) negative CDF image of GDC fibers thermal treated at $600^\circ\text{C}$ for 1 hr. ....	93
Fig. 4.16	SEM images of $1200^\circ\text{C}$ thermally treated GDC (a) single fiber and (b) TEM bright field image revealing polycrystalline character, (c) SEM image of	

as-prepared GDC hydrocarbonate fibers with some agglomeration, and (d) fibrous morphologies in bundle.....	94
Fig. 4.17 Average grain size of GDC fiber plotted against thermal treatment temperature.....	95
Fig. 4.18 DTA/TG results of P-LSM powders. The temperature ramp rate was 10°C/min. ....	105
Fig.4.19 XRD patterns of P-LSM powders (a) as-prepared, and by different thermal treatment at the temperature of (b) 300°C, (c) 400°C, (d) 500°C, (e) 600°C, (f) 700°C, (g) 800°C, and (h) 900°C.....	106
Fig. 4.20 DTA/TG results of A-LSM powder. The temperature ramp rate was 10°C/min. ....	107
Fig.4.21 XRD patterns of A-LSM powders (a) as-prepared, and by different thermal treatment at temperature of, (b) 300°C, (c) 400°C, (d) 500°C, (e) 600°C, (f) 700°C, (g) 800°C, and (h) 900°C.....	108
Fig. 4.22 TEM micrographs showing (a) BF and (b) negative CDF of 800°C thermal treated P-LSM powders, and (c) BF and (d) negative CDF of A-LSM 800°C thermal treated powders.....	109
Fig. 4.23 Plot of specific surface area against thermal treated temperature of P-LSM and A-LSM.....	112
Fig. 4.24 SEM microstructures showing fracture surfaces of sintered (a) P-LSM-S, (b) A-LSM-S, and (c) H-LSM layers on YSZ substrates thermal treated at 1200°C for 1 hr. ....	113
Fig. 4.25 SEM micrograph showing fracture surface of porous P-LSM layer on YSZ electrolyte thermally treated at 1200°C for 1 hr. ....	114
Fig. 4.26 (a) Voltage curve profile with 7.5 mA current input and (b) linear I-V curve of 1200°C thermally treated A-LSM-S/YSZ half cell at 500°C.....	117
Fig. 4.27 Arrhenius plot of log(T/ASR) of various LSM layers prepared by spray coating, then thermal treating at 1200°C for 1 hr. ....	119
Fig. 4.28 SEM micrographs showing fracture surfaces of sintered P-LSM-S layers and YSZ thermally treated at (a) 1100°C and (b) 1200°C for 1 hr. ....	120
Fig. 4.29 Relative density and average grain size plotted against sintering temperature of YSZ tape.....	125
Fig. 4.30 SEM micrographs showing the top microstructures of 8Y-YSZ tape sintered at (a) 1200°C, (b) 1300°C, (c) 1400°C, (d) 1500°C, and (e) 1600°C for 1 hr in air. ....	126
Fig. 4.31 AC impedance results of 1500°C sintered 8Y-YSZ plate in static flowing air at	

	(a) 700°C, (b) 600°C, (c) 500°C, (d) 400°C, and (e) 300°C.....	127
Fig. 4.32	Plot of electrical conductivity against reciprocal absolute temperature.....	128
Fig. 4.33	SEM microstructures of fractures of LSM/YSZ interface co-sintered at (a) 1000°C, (b) 1100°C, (c) 1200°C, and (d) 1300°C for 1 hr.....	129
Fig. 4.34	SEM microstructures of (a) the fracture surface of LSM/YSZ/NiO-YSZ single cell final-treated at 1200°C for 1 hr, the top views of (b) LSM and (c) NiO-YSZ layers, and (d) closer-view of the fracture surface of YSZ electrolyte .....	130





## List of Tables

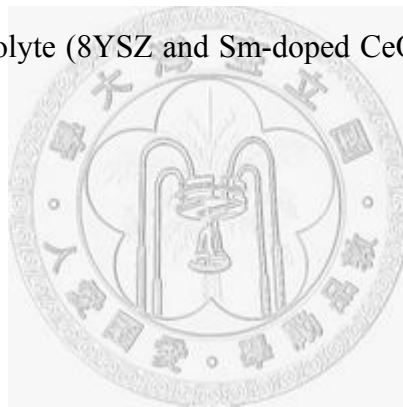
Table 2.1	Compariion of three fiber fabrication procedures .....	18
Table 2.2	Ionic conductivities and ionic transference number ( $t_i$ ) of rare earth doped ceria at 800°C.....	37
Table 2.3	Comparison of LSM fabrication procedures .....	45
Table 3.1	Formulations of the synthesis of cerium hydrocarbonate fiber, $[\text{Ce}^{3+}] = 0.025 m_c$ .....	60
Table 3.1	Continued .....	61
Table 3.2	Formulations for the synthesis of cerium hydrocarbonate synthesis, $[\text{Ce}^{3+}] = 0.1 m_c$ .....	62
Table 4.1	ICP quantitative results of Gd and Sm doped cerium hydrocarbonate fibers and correspondent formulation of GDC and SDC.....	83
Table 4.2	Quantitative analysis of P-LSM and A-LSM .....	110
Table 4.3	BET specific surface area of P-LSM and A-LSM thermal treated at various temperatures .....	111
Table 4.4	Characteristic length of TBP of YSZ and all the LSM thin layers calculated according to Saltykov equation .....	115
Table 4.5	Carbon content of LSM powders by the treatment in specified conditions	116
Table 4.6	ASR results of all the LSM layers on YSZ electrolyte thermal treated at 1200°C .....	118

## Chapter 1 Introduction

Solid oxide fuel cell (SOFC) is an electrical energy generator. Comparing with traditional power plant, SOFC transforms chemical energy into electrical energy directly without associated mechanical energy loss, which makes SOFC a high efficiency (to 85% theoretical maximum) and noiseless power generator. Several advantages of SOFC have been known in literature [\[U.S. Department of Energy, 2004\]](#). The cell adapts variety kinds of fuels without poisoning the electrodes. If hydrogen is fed as fuel, the by-products will be nothing but water vapor and heat exhaust. Besides, the additional by-product is carbon dioxide if hydrocarbon fuels are used.

8 mol% yttria-stabilized zirconia (8YSZ) is the most common electrolyte material for SOFC due to its high stabilization in reduced atmosphere at high operation temperature ( $\geq 800^{\circ}\text{C}$ ). The ionic conductivity of YSZ is almost independent of oxygen partial pressure when the oxygen partial pressure is higher than  $10^{-24}$  atm [\[Minh, 1993\]](#). But high operation temperature ( $\sim 800^{\circ}\text{C}$ ) is one of shortages as for SOFC applications. In contrast, ceria ( $\text{CeO}_2$ ) possibly works as an electrolyte at intermediate temperature (of  $650^{\circ}\text{C}\sim 500^{\circ}\text{C}$ ). This advantage makes ceria-cell able to shorten the start-up period of SOFC, and to reduce the material degradation rate. Therefore, the life time of SOFC may be extended dramatically.

In a SOFC, the cathode material must exhibit good electronic and ionic conductivities. On the other hand, its structure should be porous for gas diffusion. Porous structure of cathode is also helpful to suppress thermal shock during cycling operation. Essentially, match of coefficient of thermal expansion (CTE) of electrode and electrolyte is another important issue as engineering the materials. As a consequence, porous cathode consisted of perovskite type strontium-doped lanthanum manganite ((La,Sr)MnO<sub>3</sub>, LSM) in good conductivity (better than 100 S/cm at 1000°C<sup>[Kuo *et al.*, 1990]</sup>) and matched CTE to electrolyte (8YSZ and Sm-doped CeO<sub>2</sub>) is the primary interesting target of this study.



## Objectives

In this study, gadolinia and samaria doped ceria (GDC, SDC) fibers were synthesized by chemical co-precipitate method, as our previous patent application<sup>[Sung *et al.*, 2007]</sup>. The doped ceria fiber is a potential material to modify the surface of ceria- or zirconia-based electrolyte, by increase of the surface area of electrolyte. With the coating of doped ceria fibers, the area of triple-phase-boundary (TPB, the three phase boundary of ionic conductor, electrical conductor, and gas phase) tends to be increased.

Previous study<sup>[Sung, 2007]</sup> on morphology observation (aspect ratio) of synthesized

fibers, the concentrations of starting agents, such as citric acid and sodium hydroxide, are important issues. Other than fibers, the stick-in-bundle and flake-shape colloidal particles could be synthesized with different concentrations of starting agents. The chemical composition and kinetic reaction of fibers are interesting and essential for the development of fiber technology.

LSM powder for cathode was prepared by two sol-gel routes in this study, including Pechini method<sup>[Pechini 1967]</sup> and the sol-gel process with polyacrylic acid (PAA) as gelling agent<sup>[Hsu, 2003]</sup>. Binder-burn-out of organic additive is one of the important steps for the synthesis of high quality LSM powder. The chemical composition, the homogeneity and carbon residue of synthesized LSM powders is important for electric conductivity. Quantitative analysis with EDS is necessary to verify the relationship. The effect of the residual carbon on interface area specific resistance (ASR) between LSM and YSZ will be discussed with respect to various thermal treatments of the powders.

## Chapter 2 Literature Review

### 2.1 Electric Conductive Cerium Oxide

Cerium oxide ( $\text{CeO}_2$ ), also called ceria, shows light yellow color. The crystal structure of ceria at room temperature is a fluorite ( $\text{CaF}_2$ ) structure, as shown in Fig. 2.1<sup>[Chiang, 1997]</sup>. Ceria with tri-valent dopant (e.g.  $\text{Sm}^{3+}$ ) is a potential alternative electrolyte of SOFCs due to its several advantages over zirconia-based oxide. Fig. 2.2 compares the conductivities of some potential materials, including yttria stabilized zirconia (YSZ)<sup>[Yang et al., 2003][Guo et al., 2005]</sup>, gadolinia doped ceria (GDC)<sup>[Sin et al., 2004]</sup>,  $\text{La}_{1-x}\text{Sr}_x\text{Ga}_{1-y}\text{Mg}_y\text{O}_{3-\delta}$  (LSGM)<sup>[Ohnuki et al., 2006]</sup>, and  $\text{Bi}_3\text{NbO}_7\text{-Bi}_3\text{YO}_6$ <sup>[Abrahams et al., 2006]</sup> systems. All the samples in Fig. 2.2 were bulky specimens. The conductivity of 20GDC (20 mol% Gd) is about one order better than that of 8YSZ, especially in the temperature lower than 600°C.

The other materials, such as LSGM and bismuth-based systems show a higher conductivity (Fig. 2.2), but some known disadvantages, such as difficult to synthesize a pure perovskite LSGM phase, or reduction of Bi-based system, limit LSGM and Bi-based electrolytes for practical application in SOFCs.

For a SOFC, the conductivity should exceed 0.01 S/cm (Fig. 2.2). It is noted that the working temperature for YSZ system normally higher than 700°C, and higher than

550°C for LSGM and GDC systems. The working temperature, however, could be reduced by decreasing the thickness of electrolyte. Therefore, the necessary temperature for operating could be further reduced by decreasing its electrolyte thickness of anode or cathode supported SOFC.

Similar with zirconia-based electrolyte, the ionic conductivity of ceria material is controlled by the concentration of oxygen vacancies. The major oxygen vacancies are coming from the extrinsic addition of aliovalent oxides, such as Gd<sub>2</sub>O<sub>3</sub> and Sm<sub>2</sub>O<sub>3</sub>. The defect reaction of the dissolution of Gd<sub>2</sub>O<sub>3</sub> into CeO<sub>2</sub> lattice could be written in Kroger-Vink notation as follow.



Two Ce<sup>4+</sup> ions are substituted by two Gd<sup>3+</sup> ions, and result in an oxygen vacancy. Fig. 2.3 shows a unit cell of doped fluorite structure with vacancy defect. In GDC case, the host cation is Ce<sup>4+</sup> and the dopant is Gd<sup>3+</sup>. As showing in Eq. (2-1), to maintain the electrical neutrality, the following concentration relationship should exist.

$$2[Gd'_{ce}] = [V_o^{\bullet\bullet}] \quad (2-2)$$

and the ionic conductivity ( $\sigma_i$ ) could be expressed as follow.

$$\sigma_i = qn\mu \quad (2-3)$$

where q is the charge, n and  $\mu$  are the number of mobile oxygen vacancies and mobility

of oxygen ions, respectively. According to Eq. (2-2), the concentration of oxygen vacancies will linearly increase with the increasing of dopant concentration. The number of mobile oxygen vacancies ( $n$ ), however, will not linearly increase with the dopant due to the formation of defect association between  $Gd'_{ce}$  and  $V_o^{\bullet\bullet}$  at lower temperature. The defect association will consume the number of mobile oxygen vacancies. Therefore, the concentration and ionic conductivity of mobile oxygen decrease as the doping amount reaches its plateau even though the total number of oxygen vacancies increases linearly [Singhal *et al.*, 2003]. Similar phenomenon has also been reported for other cases with aliovalence dopant, such as  $Sm^{3+}$ . In Yahiro's study [Yahiro *et al.*, 1988], the conductivity of SDC increased with the increasing of Sm content, then decreased when the content of Sm was higher than 20 at%. Other results were also reported by Huang's [Huang *et al.*, 1997] and Zha's [Zha *et al.*, 2003] works. The optimal content of Gd or Sm ion was around 15 at%~17 at%. In addition, Yahiro *et al.* reported that the conductivity of 20SDC at 500°C is close to the conductivity of calcia stabilized zirconia (CSZ) at 900°C. This high conductivity of doped ceria apparently offered the possibility for a SOFC to work at intermediate temperature (500°C~700°C).

Although doped ceria shows better electrical conductivity than that of stabilized zirconia, the reduction behavior of doped ceria, as shown in the following equation,

made the electrolyte semi-conductive.



The reduction of  $Ce^{4+}$  to  $Ce^{3+}$  or to metallic Ce induces high electronic conductivity, showing n-type conductive behavior. The electric current flowing through the  $CeO_2$  electrolyte, instead of open circuit, lowers the terminal voltage from theoretical value, and further reduces the output power efficiency of SOFC. As the increase of electronic conductivity resulting from the reduction of cerium ions, the ionic transference number ( $t_i$ ) decreases.

Tuller and Nowick<sup>[Tuller *et al.*, 1975]</sup> found the linear relationship between oxygen partial pressure and reciprocal temperature at different  $t_i$  values of yttria doped ceria (YDC). Their study reported that the oxygen partial pressure difference between  $t_i = 0.99$  and  $t_i = 0.9$  is about four orders. The  $t_i$  value of the YDC could reach up to 0.99 only when the oxygen partial pressure higher than  $10^{-6}$  atm at  $800^\circ C$ , but this pressure could drop to about  $10^{-21}$  atm at  $450^\circ C$ .



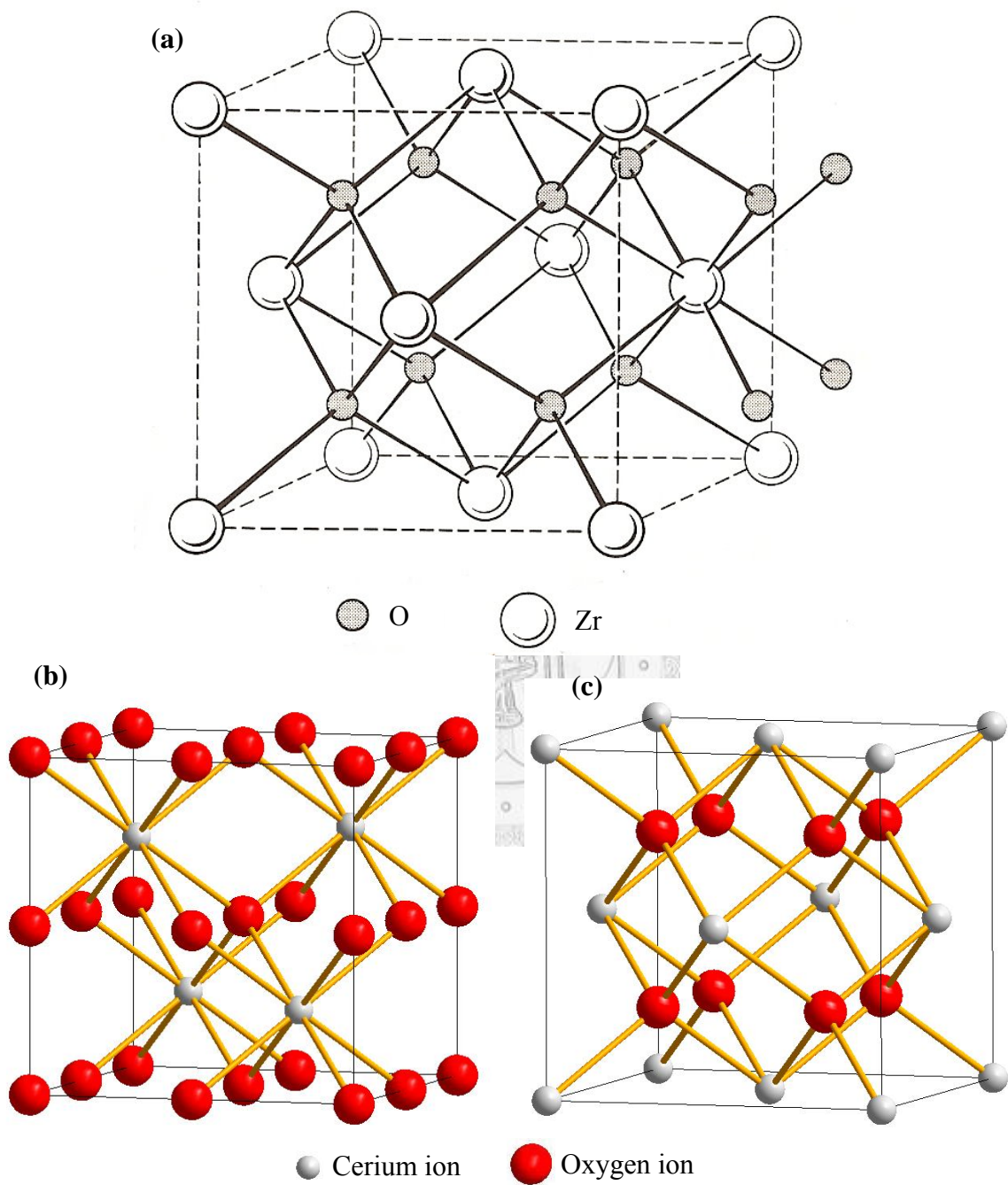


Fig. 2.1 (a) Fluorite structure<sup>[Chiang *et al.*, 1997]</sup>, CeO<sub>2</sub> structure of showing (b) oxygen ion and (c) cerium ion is selected as the original point, respectively.

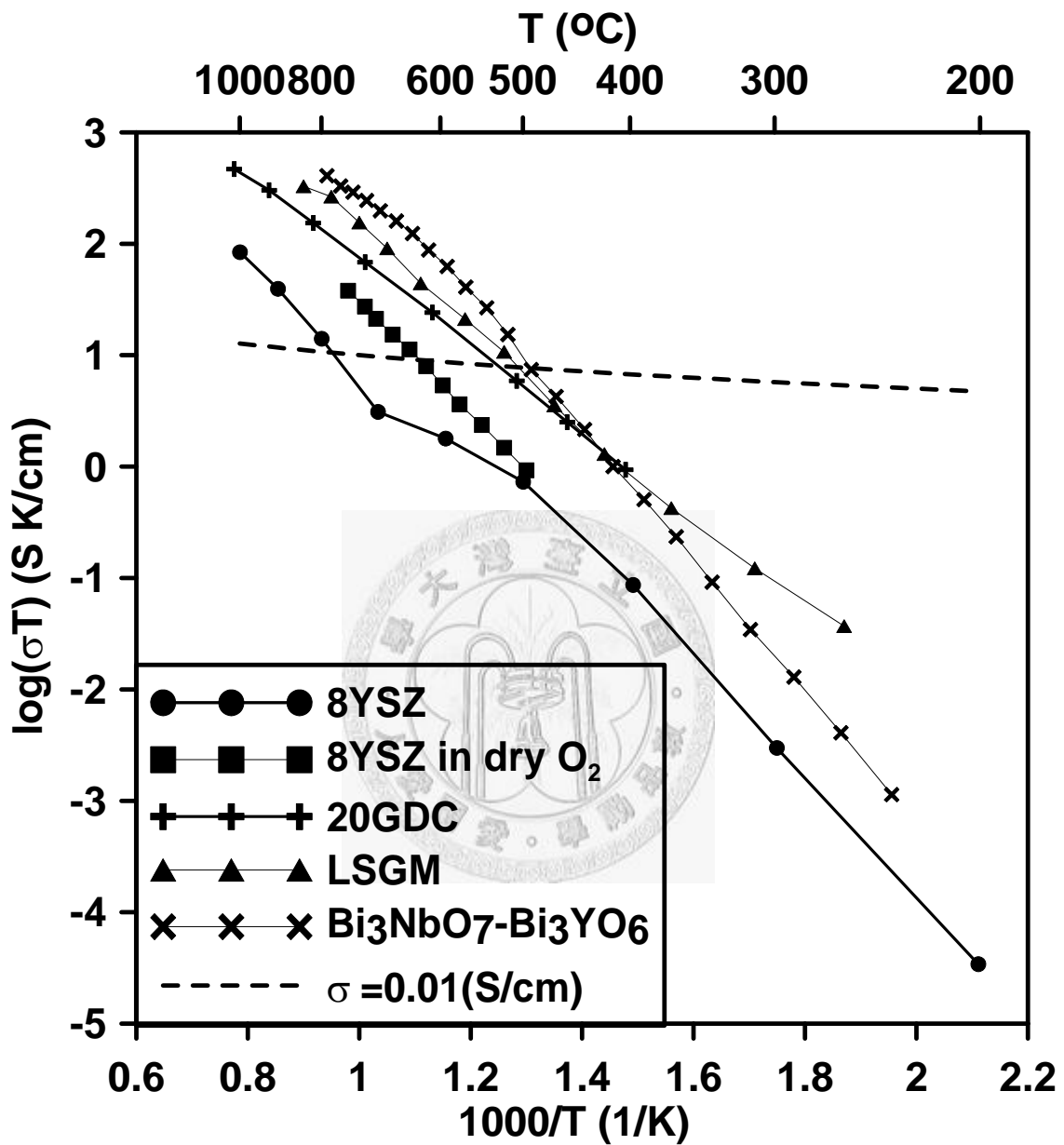


Fig. 2.2 Temperature depend electrical conductivities of 8YSZ<sup>[Yang et al., 2003]</sup>, 8YSZ in dry  $O_2$ <sup>[Guo et al., 2005]</sup>, 20GDC<sup>[Sin et al., 2004]</sup>, LSGM<sup>[Ohnuki et al., 2006]</sup> and  $Bi_3NbO_7-Bi_3YO_6$ <sup>[Abrahams et al., 2006]</sup>, the dotted curve presents the electrical conductivity equal to 0.01 S/cm. Guo<sup>[Guo et al., 2005]</sup> measured the 8YSZ sample in dry oxygen atmosphere, instead of air atmosphere.

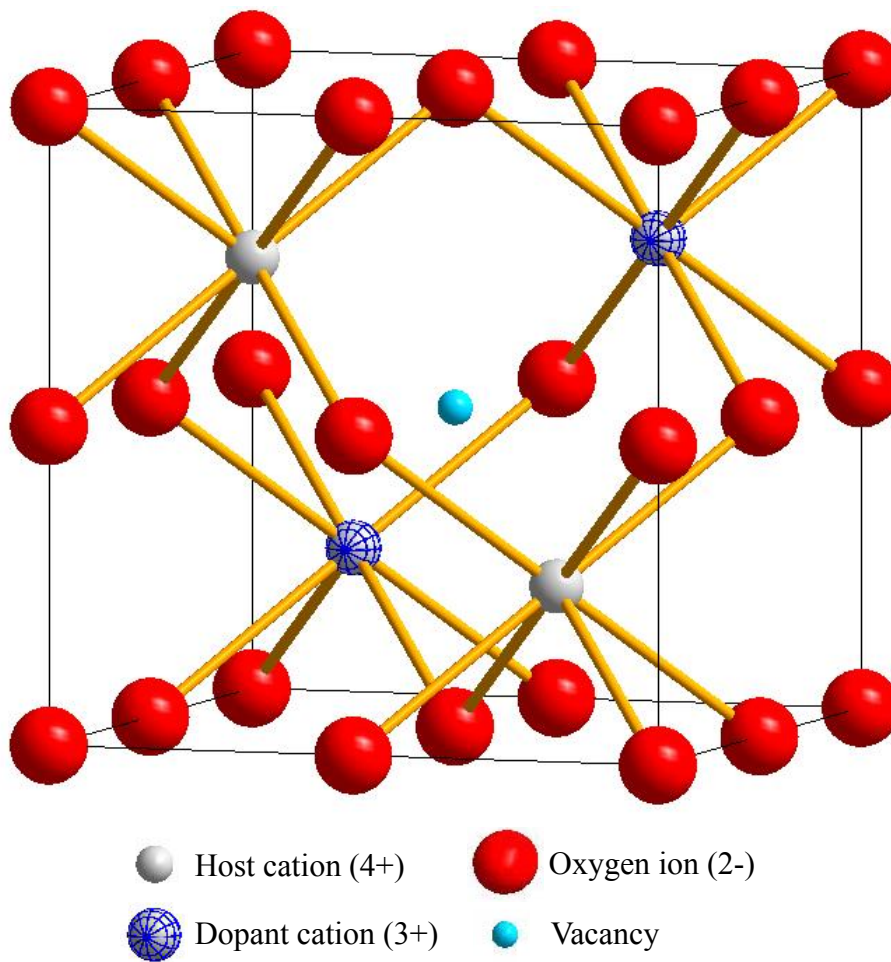
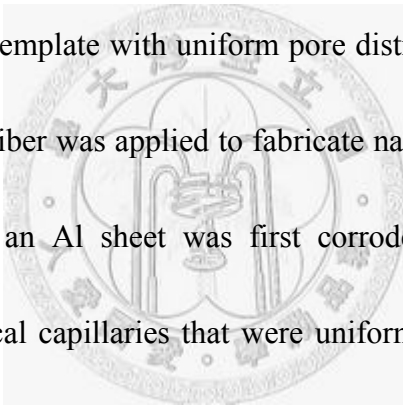


Fig. 2.3 Fluorite structure with one host cation replaced by a lower-valent cation, and created an oxygen vacancy.

## 2.2 Synthesis of Oxide Fibers

There are four different methods that were used to synthesize ceria or zirconia nanowires, nanorods, or fibers. Those included anodic alumina oxide (AAO) template, hydrothermal precipitate, electrospun (also called electrospinning), and base-acid precipitation methods. [Table 2.1](#) summarized the results from these procedures.

### 2.2.1 AAO Template

With an Al sheet as a template with uniform pore distribution and capillary size, a sol-gel procedure of oxide fiber was applied to fabricate nanowires in the capillaries. In Xu's research [\[Xu et al., 2003\]](#), an Al sheet was first corroded by phosphoric acid and obtained a sheet with vertical capillaries that were uniformly distributed on the sheet.  The average diameter of the capillary was about 200 nm and the depth was about 50  $\mu\text{m}$ . The capillary density is  $10^8\sim 10^{11}$  #/cm<sup>2</sup>. Zirconyl chloride ( $\text{ZrOCl}\cdot 8\text{H}_2\text{O}$ ) dissolving in alcohol solution was the precursor and the pH value was controlled to 2.0 with HCl. After immersing the Al- $\text{Al}_2\text{O}_3$  (AAO) template into precursor for different periods, the sheet was dried at room temperature for 1 hr and then thermal treated at 600°C for 6 hr. The zirconia nanowires were removed by dissolving AAO template in NaOH, and then rinsing the NaOH.

The dimensions of nanowires were the same as the capillary on the AAO sheet. The ring diffraction pattern from TEM indicated that the nanowires were polycrystalline with cubic phase. Different kinds of shape of zirconia could be synthesized with different immersion period. With a longer immersion period, nanowires could be synthesized. However, zirconia nanotubes would form with shorter immersion period.

### 2.2.2 Hydrothermal Precipitation

Hydrothermal treatment is a potential procedure to fabricate ceramic powder without calcination. The obtained particle size could be retained to nano-scale because that the calcination step can be skipped. Besides, there are the other advantages of this procedure, including homogeneous nucleation, relative lower synthesis temperature and weak agglomeration.

In Zhou's study<sup>[Zhou *et al.*, 2005]</sup>, a directly addition of NaOH into cerium nitration solution was applied. The formed yellow slurry underwent a hydrothermal treatment at 100°C for 10 h with an autogenous pressure and following thermal treatment at 350°C for 4 hr. Ceria nanorods with 100~300 nm in length and 13~20 nm in diameter were obtained. To compare with ceria nanorods, ceria powders synthesized with the same procedure without hydrothermal treatment were also fabricated. The ceria powders

exhibited irregular shape with an average particle size about 8 nm, and weak agglomeration was observed by TEM. Both powders showed pure cubic fluorite structure by XRD analysis.

CO catalytic oxidation was applied in both ceria nanorods (with hydrothermal treatment) and nanoparticles (without hydrothermal treatment). The results revealed that ceria nanorods showed better CO conversion than that of the ceria nanoparticles even though the nanoparticles have greater specific surface area than the nanorods by BET measurement. The adsorptive ability of CO to different plane of ceria results in this unusual phenomenon. According to their HRTEM results, ceria nanorods grew along [110] direction and enclosed by {110} and {001} planes, which could adsorb CO more easily. In contrast, the domain planes in nanoparticles were identified to be {111} which were less reactive with CO molecule. Due to the reactivity planes, the ceria nanorods were better as a catalyst for CO oxidation than nanoparticles.

### **2.2.3 Electrospinning**

This method is also called electrospun. [Fig. 2.4](#) shows the scheme of this method. A solution (or suspension) with certain viscosity was carried by a syringe pump with capillary. When applying a voltage onto the orifice of capillary, the pendant

hemispherical drop at the orifice would carry the charge and form a conical shape (Taylor cone). When a critical voltage is reached a critical value, the electronic force from the charge on the drop would overcome the surface tension of the solution (The Rayleigh instability), and a jet of solution could be ejected from one electrode (orifice) to the other<sup>[Subbiah *et al.*, 2005]</sup>. The solvent was evaporated during the spur, and the polymer-ceramic green fibers could be formed. This process is a good method to fabricate extreme long fibers and easy for manufacturing.

In Azad's study<sup>[Azad *et al.*, 2005]</sup>, a syringe pump was filled with solution consist of  $Y^{3+}/Zr^{4+}$  or  $Gd^{3+}/Ce^{4+}$  ions and PVP for electrospinning. High voltage ranging between 12 and 15 kV were applied onto the capillary of syringe pump to provide the electric field on the solution, and the flow rate was controlled to be from 0.03 to 0.12 ml/h. The fabricated fibers were then calcined at 1500°C (for YSZ fibers) and 1000°C (for GDC fibers). The YSZ and GDC fibers remained their morphologies without any breaking during the thermal treatment. The diameter of the 10GDC fiber was about 350 nm showing polycrystalline by 1000°C and 1200°C treatments. Raman spectrum analysis showed that there were no PVP polymers left in the fibers. Pure cubic fluorite structure of zirconia and ceria was observed. The viscosity of precursor for Yang's electrospinning was also provided by PVA. In their study<sup>[Yang *et al.*, 2005]</sup>, the applied

voltage was reduced to 7 kV, and the final diameter of ceria fibers was between 50 and 100 nm. The XRD analysis revealed that pure ceria was obtained after calcination at 500°C.

Besides electrospinning with solution, zirconia suspension could also be the precursor for the electrospinning used in Zhang's research<sup>[Zhang *et al.*, 2006]</sup>, of which the applied voltage would affect the morphology of the fiber product. With a voltage higher than 11.6 kV, necking of as-prepared fiber was observed. This phenomenon got more apparent with the increasing of applied voltage. In contrast, when the voltage was less than 11.6 kV, the fiber could not be formed due to the unstability of conical drop (shown in Fig. 2.4). The diameter of as-prepared fibers was linear proportion to the zirconia powder content in solution. The fibers could not be prepared when the solid content was lower than 1 wt%. On the other hand, due to the shrinkage of fiber during thermal treatment, the fiber could not be fabricated when the solid content was higher than 10 wt%, either. After sintering at 1200°C, the grain size of zirconia grew from 5~10 nm to about 150 nm. This final grain size limited the smallest diameter of the fibers to about 200 nm.



## 2.2.4 Precipitation Method

One of the requirements for an electrolyte used for SOFC includes high sintered density to maintain high ionic conductivity, and to avoid the cross-diffusion of oxygen and fuel. In order to reduce the sintering temperature of the ceramic electrolyte, the particle size of starting powders should be as small as possible. Besides, the spherical-like morphology of the starting powder could also favor particle flowing in mold and shape forming. In order to fabricate ultra fine powders with spherical shape, co-precipitate synthesis has been widely used due to its homogeneous and nano-scale particle synthesis. In addition, by using different synthesis conditions, different particle morphologies of the precipitates can be made.

Wang *et al.*<sup>[Wang *et al.*, 2003]</sup> fabricated spherical particles of SDC with a precipitant of ammonium hydrogen carbonate (AHC,  $\text{NH}_4\text{HCO}_3$ ). These SDC powders could be sintered up to >99% theoretical density (T.D.) at  $1200^\circ\text{C}$ . In Peng's research<sup>[Peng *et al.*, 2002]</sup>, glycine ( $\text{NH}_2\text{CH}_2\text{COOH}$ ) was used as a precipitant, a relative density higher than 95% of SDC pellet was obtained if sintering at  $1500^\circ\text{C}$ .

Therefore, almost no researchers focus on the fabrication of fibrous ceria-based particles from solution. However, in Hsu's study<sup>[Hsu *et al.*, 1988]</sup>, a solution with  $\text{Ce}(\text{SO}_4)_2$  and  $\text{H}_2\text{SO}_4$  aging at  $90^\circ\text{C}$  for 12 hr could appear Ce-contained rods, spheres, and the

mixture of rods and spheres in different material concentration ranges. The average size of spherical particles is in the range of 30 to 240 nm. Higher concentrations of cerium ions and  $\text{H}_2\text{SO}_4$  increased the particle size. The effect of the addition of  $\text{Na}_2\text{SO}_4$  was investigated, which also influenced the average particle size. Besides, in a certain concentration window of each starting species, Ce-contained rods with the dimension of 2  $\mu\text{m}$  in length and submicron in width could be obtained in the same aging period of the spherical synthesis.



Table 2.1 Comparison of three fiber fabrication procedures

Methods	AAO template	Hydrothermal precipitate	Electrospinning	Precipitation
Precursor	ZrOCl <sub>2</sub> ·8H <sub>2</sub> O alcohol solution with HCl	NaOH added cerium slurry	Water based solution with PVP/zirconia powder suspension	Ce(SO <sub>4</sub> ) <sub>2</sub> , H <sub>2</sub> SO <sub>4</sub> and Na <sub>2</sub> SO <sub>4</sub>
Aspect ratio	up to 250	20~30	N/A	N/A
Crystalline	Polycrystalline	Single crystalline	Polycrystalline	N/A
Characters	Nanowires or nanotube fabricated	Higher CO oxidation activity than CeO <sub>2</sub> nanoparticles	Possibility for long fibers and easy manufacture	Rods, spherical particles, or the mixture could be fabricated
Reference	[Xu <i>et al.</i> , 2003]	[Zhou <i>et al.</i> , 2005]	[Zhang <i>et al.</i> , 2006] [Azad <i>et al.</i> , 2005] [Yang <i>et al.</i> , 2005]	[Peng <i>et al.</i> , 2002]

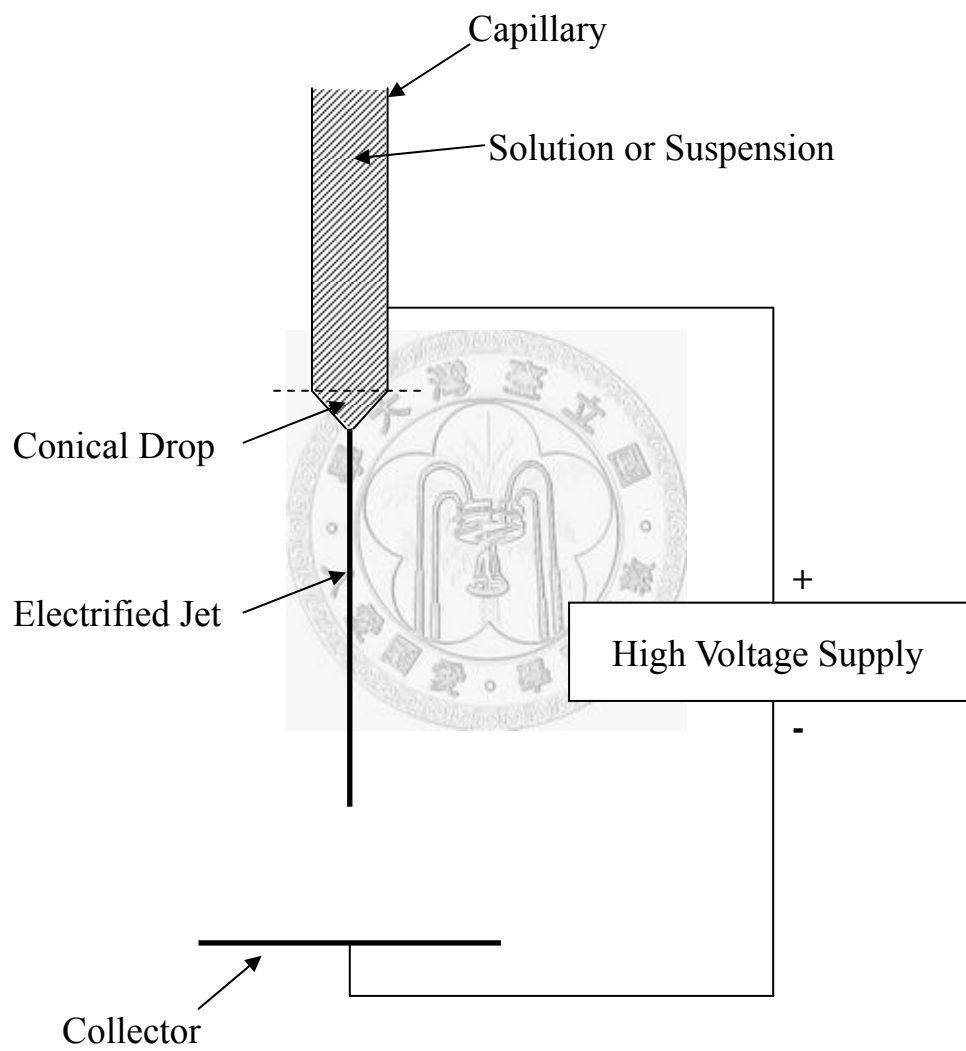


Fig. 2.4 Scheme of electrospinning of ceramic fibers.

## 2.3 Electrical Properties of Cerium Oxide

### 2.3.1 Theory of Oxygen Transport [Singhal *et al.*, 2003][Kilner, 2000][Inaba *et al.*, 1996]

The electrical conductivity ( $\sigma$ ) of an ionic conductor could be expressed by Arrhenius equation as following,

$$\sigma T = A \exp\left(\frac{-E_a}{kT}\right) \quad (2-5)$$

where  $A$  is a pre-exponential factor,  $k$  is Boltzmann constant and  $E_a$  is the activation energy of electrical conduction. This equation is derived from Eq. (2-3). The mobility  $\mu$  is related to the self-diffusion coefficient,

$$\mu = \frac{q}{kT} D \quad (2-6)$$

where  $q$  is charge, and  $D$  is the self-diffusion coefficient, which could be further expressed by random walk theory in 3-dimension as shown below.

$$D = \frac{z}{6} f(1-c)a_0^2\nu_0 \exp\left(-\frac{\Delta G_m}{kT}\right) \quad (2-7)$$

where  $z$  is the coordination number of the diffusive ion,  $1/6$  is the geometry constant of a simple cubic structure,  $f$  is correlation factor which presents the deviation from randomness of the ionic jumping,  $a_0$  is the jumping distance,  $\nu_0$  is the jumping frequency,  $\Delta G_m$  is the free energy of migration. The equivalent sites for oxygen ions to transport, in fact, are partially occupied by oxygen ions. The fraction of the occupied sites is the term  $c$ , and  $(1-c)$  is the fraction of the unoccupied sites. According to thermal

dynamic theory,  $\Delta G_m = \Delta H_m - T\Delta S_m$ . Eq. (2-7) could be expanded as following,

$$D = \frac{z}{6} f(1-c)a_0^2 v_0 \exp\left(\frac{\Delta S_m}{k}\right) \exp\left(-\frac{\Delta H_m}{kT}\right) \quad (2-8)$$

Defining  $\gamma$  as

$$\gamma = \frac{z}{6} f \exp\left(-\frac{\Delta S_m}{k}\right) \quad (2-9)$$

and substitute Eq. (2-8) and Eq. (2-9) into Eq. (2-6), the mobility could be expressed as

$$\mu = \frac{q}{kT} \gamma(1-c)a_0^2 v_0 \exp\left(-\frac{\Delta H_m}{kT}\right) \quad (2-10)$$

In a crystal with vacancy sites for vacancies to transport, there are N sites per unit cell.

In Eq. (2-3), n is the number of mobile oxygen vacancies, and this number is the product of N and c. Thus

$$\sigma = N\gamma \frac{q^2}{kT} c(1-c)a_0^2 v_0 \exp\left(-\frac{\Delta H_m}{kT}\right) \quad (2-11)$$

Now replace the term (1-c) with  $[V_o^{\bullet\bullet}]$ , the concentration of oxygen vacancies, then the

alternative expression of Eq. (2-11),

$$\sigma = N\gamma \frac{q^2}{kT} [V_o^{\bullet\bullet}](1-[V_o^{\bullet\bullet}])a_0^2 v_0 \exp\left(-\frac{\Delta H_m}{kT}\right) \quad (2-12)$$

It is noted that the term  $([V_o^{\bullet\bullet}](1-[V_o^{\bullet\bullet}]))$  will increase linearly with  $[V_o^{\bullet\bullet}]$  at extremely low  $[V_o^{\bullet\bullet}]$  and reach a maximum at  $[V_o^{\bullet\bullet}] \cong 1-[V_o^{\bullet\bullet}]$ . Therefore, an ideal expression of the trend of ionic conductivity depending on  $[V_o^{\bullet\bullet}]$  is shown in Fig. 2.5.

### 2.3.2 Dopant Effect

In an ionic conductive material, such as ceria, the charge carrier is oxygen ion vacancy (or oxygen), which dominates the ionic conductivity of ceria according to Eq. (2-12). For a pure ceria, the oxygen vacancy is coming from the intrinsic defects (Frenkel or Schottky), of which the concentration is remarkable at high temperature only. For this reason, the conductivity of pure ceria is poor.

Fig. 2.5 is the plot of the ionic conductivity of ionic conductor against the vacancy concentration<sup>[Kilner, 2000]</sup>. It is noted that the ionic conductivity shows linear behavior

with the  $[V_o^{**}]$  at extremely low  $[V_o^{**}]$  region. According to Eq. (2-2), the conductivity is also proportional to the concentration of dopant and mobility of the ions.

Fig. 2.5 depicts that the ionic concentration will reach a maximum value when  $[V_o^{**}]$  is around 0.5. But the experimental results showed that the maximum ionic conductivity

occurring at the dopant concentration apparently lower than the predicted value. In

Yahiro's work<sup>[Yahiro et al., 1988]</sup>, 20SDC ( $\text{Sm}_{0.2}\text{Ce}_{0.8}\text{O}_{1.9}$ , 10 mol%  $\text{Sm}_2\text{O}_3$  doping) exhibits

the highest ionic conductivity in SDC system. In this case, the concentration of oxygen

vacancies is only 5%. Similar doping amount of  $\text{Gd}_2\text{O}_3$  in ceria was reported by several

researchers<sup>[Zha et al.,2003][Zhang et al.,2006]</sup>, who reported that the optimal content of  $\text{Gd}_2\text{O}_3$  was

lied between 7 and 10 mol%. This phenomenon is explained by the formation of defect

associations (or clusters), e.g.,  $\{Sm'_{Ce}V_o^{\bullet\bullet}\}^{\bullet}$  and  $\{Gd'_{Ce}V_o^{\bullet\bullet}\}^{\bullet}$ . These associates consume the vacancies and the linear relationship is no longer effective. Because of the existence of the defect association, the mobility of associated defects is greatly reduced. Therefore, the temperature dependence of the electrical conductivity of doped ceria could be divided into at least two regions. In high temperature region, the energy in lattice could overcome the binding energy of defect association and the oxygen vacancies are free to diffuse. The activation energy ( $E_a$ ) for ionic conduction is only the migration energy ( $E_m$ ). In low temperature region, the activation energy is including the binding energy of defect association ( $E_{as}$ ) and the migration energies<sup>[Singhal *et al.*, 2003]</sup>. A slope transition could be found in a diagram of  $\ln(\sigma T)$  against  $1/T$  at a critical temperature ( $T_{crit}$ ). Jung<sup>[Jung *et al.*, 2002]</sup> reported that the critical temperature was also affected by the amount of dopant. 20SDC system could reduce its critical temperature down to 591°C from 673°C of 5SDC system. The trend of  $E_a$  varied with doping contents was similar with the trend of critical temperature and showed the lowest  $E_a$  value in 20SDC system.

Originally, the substitutional defect with negative charge and oxygen vacancy with positive charge are attracted to each other and form the defect association due to the Coulombic force below the critical temperature. In this case, for the same charge of



substitutional defect (ex: monovalent  $Gd'_{Ce}$  or divalent  $Ca''_{Ce}$ ), the binding energy of defect association and the ionic conductivity should be at a similar level no matter what the doped ion is<sup>[Skinner *et al.*, 2003]</sup>. However, the experimental results showed a lot of differences in conductivity for different kinds of additive treated at 800°C. The results in Fig. 2.6 revealed that the ionic radii of dopant ions would apparently affect the ionic conductivity of doped ceria<sup>[Yahiro *et al.*, 1988][Mogensen *et al.*, 2000]</sup>. The information of ionic radii were reported by Shannon<sup>[Shannon, 1976]</sup>. From Fig. 2.6, the ionic conductivity first increases with the increasing of ionic radius (from 0.0985 nm of  $Yb^{3+}$  to 0.1079 nm of  $Sm^{3+}$ ) until the radius reach 0.109 nm, and then decreases. In the other Yahiro's<sup>[Yahiro *et al.*, 1988]</sup> work, alkaline earth ion doped ceria was investigated. The same trend was found that calcia doped ceria showed the highest conductivity where the radius of calcium ion is 0.112 nm. It could be concluded that for rare earth or alkaline earth oxides doped ceria, the critical doping ionic radius which gives the highest conductivity of doped ceria is around 0.11 nm<sup>[Inaba *et al.*, 1996]</sup>. The reason of this phenomenon was explained by the effect of the elastic strain energy around the substitutional defect. After aliovalent ions doping, there is elastic strain remained in the lattice. The remained strain is resulted from the radius mismatch of the host cation and the doping one.

In general, the highest ionic conductivity would be exhibited when the radius of

dopant ion is closest to the host ion, which results in the least elastic strain and the minimal association energy between dopant ion and oxygen vacancy<sup>[Inaba *et al.*, 1996]</sup>. Fig. 2.6, however, reveals that  $\text{Sm}^{3+}$  (0.1079 nm in radius) exhibits the highest electrical conductivity. The ions such as  $\text{Yb}^{3+}$  (0.0985 nm),  $\text{Er}^{3+}$  (0.1004 nm) or  $\text{Y}^{3+}$  (0.1019) which have the ionic radii closer to  $\text{Ce}^{4+}$  (0.097) show a lower electrical conductivity comparing with  $\text{Sm}^{3+}$ . The reason was provided by L. Minervini<sup>[Minervini *et al.*, 1999]</sup>.

In Minervini's work, the binding energy of defect association was recalculated. The association pair model was the substitutional defect to the first, second and third neighbor oxygen vacancy. The plot of binding energy of these three association pairs against ionic radii is shown in Fig. 2.7(a). Fig. 2.7(b) shows the schematic positions of these oxygen vacancies in a unit cell of ceria.

In Fig. 2.7(a), the first and second neighbor lines of binding energy are associated with different effects. Coulombic interaction between substitutional defect and vacancy always favors the first neighbor position. Smaller ions show higher binding energy with vacancy due to its higher charge density. On the other hand, the relaxation of lattice (crystallographic effect) always favors the second neighbor position. The relaxation of lattice is coming from the  $\text{Ce}^{4+}$  ion adjacent to the second neighbor vacancy and it's also related to the dopant ionic radius. The ion in this configuration could relax the attractive

force between positive charge vacancy and negative charge substitutional defect. These two effects cancel each other and form an equivalent binding energy for first and second neighbor vacancies when the dopant ionic radius is about 0.105 nm. In Fig. 2.7 (a), the equivalent binding energy which is also the minimum value is shown in the crossover point of the lines of first and second neighbor oxygen vacancy.  $Gd^{3+}$  ion has the closest ionic radius with the position of the crossover point. The cations smaller than  $Gd^{3+}$  prefer to bind with the first neighbor vacancy. In contrast, the cations larger than  $Gd^{3+}$  have higher binding energy with the second neighbor vacancy. According to Minervini's work, the optimal radius of dopant ion is around 0.105 nm (close to the radii of  $Gd^{3+}$  and  $Sm^{3+}$ ) should have lowest binding energy of defect associate and result in the highest ionic conductivity, which agree with the experimental results.

As mentioned above, for both rare earth and alkaline earth ions, the critical ionic radius is around 0.11 nm that would give the highest conductivity. Therefore, Sm- and Gd-doped ceria should have the highest ionic conductivity which was confirmed by Balazs<sup>[Balazs et al., 1995]</sup>. However, Gd-doped ceria showed surprising low ionic conductivity in Yahiro's work<sup>[Yahiro et al., 1988]</sup>, which was against the general trend. There is one possible explanation for this disagreement, which will be described in next section.

### 2.3.3 Grain Boundary/Impurity Effects

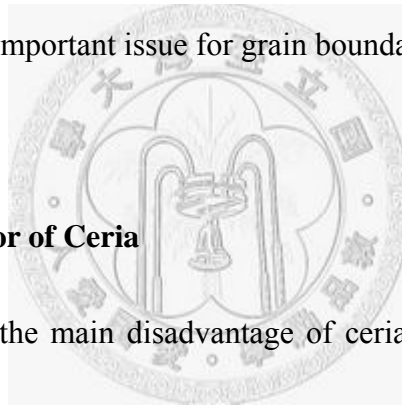
In order to reduce the grain interior resistance, Ralph *et al.* [Ralph *et al.*, 1997] tried to reduce the strains in ceria lattice by a double-doping method. The results, however, indicated that the local lattice strain around the substitutional defect was an important issue that affected the bulk conductivity. Therefore, GDC system still showed a higher grain interior conductivity comparing with the Ce-Sm-Y and Ce-La-Yb systems. On the other hand, the double-doped system performed higher grain boundary conductivity than that of GDC system. HRTEM analysis indicated that the high resistance of grain boundary on GDC system is resulted from the segregation of Gd and Si, which is a very common impurity in ceramics.

The segregation of Si would lead to the formation of an insulting, glassy film at the grain boundary, which reduce the total ionic conductivity of doped ceria. The influence of Si to grain boundary conductivity was investigated by Zhang [Zhang *et al.*, 2006]. The grain boundary conductivity apparently decreased as the impurity content of Si increased from 30 ppm to 200 ppm. Besides, the amount of Si also affects the concentration of doped  $Gd_2O_3$  that gives the highest ionic conductivity.

Moreover, Gd-rich boundary resulted in a space-charge layer at the grain boundary. Inside the space-charger layer, the concentration of oxygen vacancies was depleted, and

the negative charge Gd substitutional defects would restrict the crossover of oxygen vacancies and lead to high grain boundary resistance. The same phenomena in yttria doped zirconia and ceria systems were reported by Guo<sup>[Guo, 1995][Guo et al., 2003]</sup>.

Ralph's work gave an explanation for the huge difference of the electrical conductivity of GDC system mentioned in Section 2.3.2. Gd-doped ceria apparently exhibited higher grain boundary resistance than the other systems, such as double-doped ceria due to the segregation of Gd and impurity. For this reason, the sample preparation procedure would be a very important issue for grain boundary conductivity.



#### 2.3.4 Reduction Behavior of Ceria

It is well known that the main disadvantage of ceria is its reduction behavior at high temperature and reduced atmosphere. The reduction will induce the electronic conductivity and ceria will show an n-type conductive behavior as the reaction shown in Eq. (2-2). The raising of electronic conductivity leads to the reduction of oxygen transference number ( $t_i$ ). The value  $t_i$  could be expressed as follow,

$$t_i = \frac{\sigma_i}{\sigma_i + \sigma_e} \quad (2-13)$$

where  $\sigma_i$  is the ionic conductivity and  $\sigma_e$  is the electronic conductivity. An equation similar with  $\sigma_i$  (Eq. (2-3)) could be used to describe  $\sigma_e$ ,

$$\sigma_e = en_e\mu_e \quad (2-14)$$

where  $e$  is the charge of electron,  $n_e$  is the concentration of electron and  $\mu_e$  is the mobility of electron. The temperature dependence reductive reaction coefficient  $K$  is,

$$K = [V_o^{\bullet\bullet}]n_e^2P_{O_2}^{1/2} = K_0 \exp\left(\frac{-\Delta H}{kT}\right) \quad (2-15)$$

where  $\Delta H$  is the enthalpy difference of the reduction reaction. Therefore, the concentration of electron is,

$$n_e = (K/[V_o^{\bullet\bullet}])^{1/2}P_{O_2}^{-1/4} = (K_0/[V_o^{\bullet\bullet}])^{1/2}P_{O_2}^{-1/4} \exp\left(\frac{-\Delta H}{2kT}\right) \quad (2-16)$$

Recalling Eq. (2-2), if dopant is added into ceria,  $[V_o^{\bullet\bullet}]$  is independent of oxygen partial pressure because that it's dominated by extrinsic defect. Thus,  $n_e$  and  $\sigma_e$  are oxygen partial pressure dependence and proportional to  $P_{O_2}^{-1/4}$ . Moreover, the mobility of electron is given by,

$$\mu_e = \frac{b}{T} \exp\left(\frac{-E_e}{kT}\right) \quad (2-17)$$

where  $b$  is a pre-exponential factor and  $E_e$  is activation energy of the migration of electron. Substituting Eq. (2-16) and (2-17) into Eq. (2-14), following equation could be obtained,

$$\sigma_e = \frac{ebK_0^{1/2}}{T[V_o^{\bullet\bullet}]^{1/2}}P_{O_2}^{-1/4} \exp\left(\frac{-\Delta H - 2E_e}{2kT}\right) \quad (2-18)$$

and rewriting Eq. (2-13) with Eq. (2-18) and (2-5). A relationship between  $P_{O_2}$  and  $1/T$  could be obtained,

$$\ln P_{O_2} = 4 \ln \left\{ \frac{t_i b e K_0^{1/2}}{A(1-t_i)[V_{O^{\bullet\bullet}}]^{1/2}} \right\} - 4 \left( \frac{\Delta H}{2} + E_e - E_a \right) \frac{1}{kT} \quad (2-19)$$

From Eq. (2-19), in a diagram of  $\ln P_{O_2}$  against  $1/T$ , each value of  $t_i$  gives a straight line with a slope of  $-\frac{4}{k} \left( \frac{\Delta H}{2} + E_e - E_a \right)$  that divides the diagram into two regions. The region above the line belong to the value of  $t_i$  higher than a given one [Tuller, *et al.*, 1975] [Kudo *et al.*, 1976]. For certain oxygen partial pressure  $P_{O_2}^*$ , which gives an equal value of ionic and electronic conductivity ( $t_i = 0.5$ ),  $P_{O_2}^*$  is called “electrolytic domain boundary.” [Patterson, 1971] A  $P_{O_2}$  higher than  $P_{O_2}^*$  gives an electrolytic domain of ceria, and electronic domain occurs when  $P_{O_2}$  is lower than  $P_{O_2}^*$ .

It had been mentioned in Section 2.3.2 that the doping of aliovalent ions increase the ionic conductivity of ceria. Besides, according to Eq. (2-2), since doping tri-valent ions would induce the concentration of oxygen vacancy, the reduction of ceria was suppressed [Mogensen *et al.*, 2000], and the concentration of intrinsic oxygen vacancies could be neglected due to the concentration of vacancies was dominated by the dopant [Suzuki *et al.*, 2002]. The reduction behavior of ceria could be investigated by measuring the electrical conductivity in different  $P_{O_2}$ .

In Rupp [Rupp *et al.*, 2007] and Suzuki’s researches, the electrical conductivity of GDC thin film as a function of oxygen partial pressure was measured. In Fig. 2.8, the diagram of  $\log \sigma$  vs.  $P_{O_2}$  exhibited plateau at high  $P_{O_2}$  region and a slope of -1/4 at low  $P_{O_2}$ .

At high  $P_{O_2}$ , ionic conductivity, which is independent upon  $P_{O_2}$  according to Eq. (2-5), dominates the electrical conductivity and plateau is shown. In the region of low  $P_{O_2}$ , the reduction of ceria occurs and electronic conductivity would dominate the total conductivity.

It had been mentioned that  $\sigma_e$  is oxygen partial pressure dependence, and proportional to  $P_{O_2}^{-1/4}$ . However, the slope of -1/6 was found in pure ceria system at temperature higher than 800°C, as the higher temperature curves shown in Fig. 2.8(a).

The appearance of intrinsic oxygen vacancy was responsible for this transition. In the intrinsic dominant region, the concentration of electron is two times greater than  $[V_O^{\bullet\bullet}]$  ( $n_e=2[V_O^{\bullet\bullet}]$ ) to balance the local charge in the lattice. Therefore, K could be rewritten as below.

$$K = [V_O^{\bullet\bullet}]n_e^2 P_{O_2}^{1/2} = \frac{1}{2}n_e^3 P_{O_2}^{1/2} \quad (2-20)$$

so

$$n_e = (2K)^{-1/3} P_{O_2}^{-1/6} \quad (2-21)$$

and the slope of  $\log\sigma$  vs.  $P_{O_2}$  diagram was -1/6<sup>[Chinang et al., 1997]</sup>.

The  $t_i$  values of several dopant in ceria were reported by Yahiro<sup>[Yahiro et al., 1988]</sup> and listed in Table 2.2. The  $t_i$  value could be enhanced up to the value higher than 0.97 from 0.35 of pure ceria at 800°C. Yahiro also reported that electrolytic domain boundary



would vary with the radii of dopant ions, the results are shown in Fig. 2.9<sup>[Yahiro *et al.*, 1989]</sup>.

It is obvious that the trend is very similar with the dopant radius dependence of ionic conductivity shown in Fig. 2.6. The minimum of electrolytic domain boundary occurs at a critical radius of dopant ion around 0.11 nm. Since the reduction of ceria will induce the oxygen deficiency, the total ceria mass will loss in reduction atmosphere due to the formation of gaseous oxygen. Yahiro's<sup>[Yahiro *et al.*, 1988]</sup> report showed that SDC system has the highest resistibility against the reduction atmosphere.



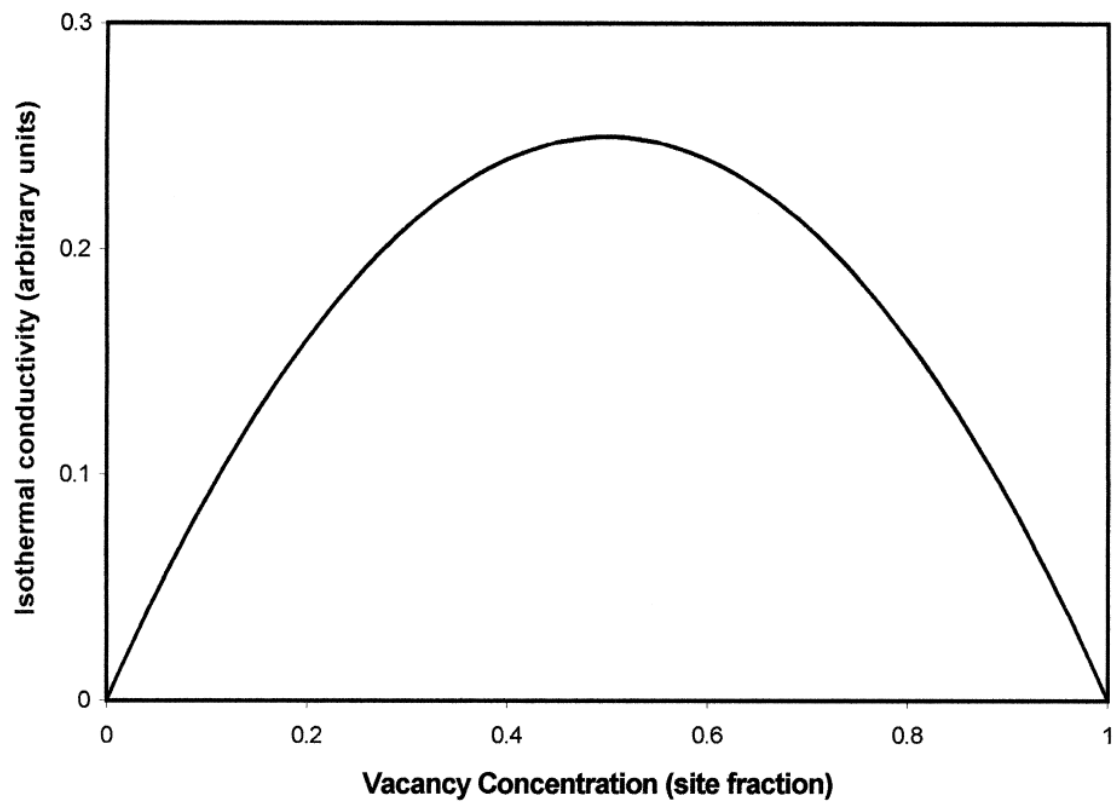


Fig. 2.5 Vacancy concentration dependence of the ionic conductivity from Eq. (8) [Kilner, 2000]

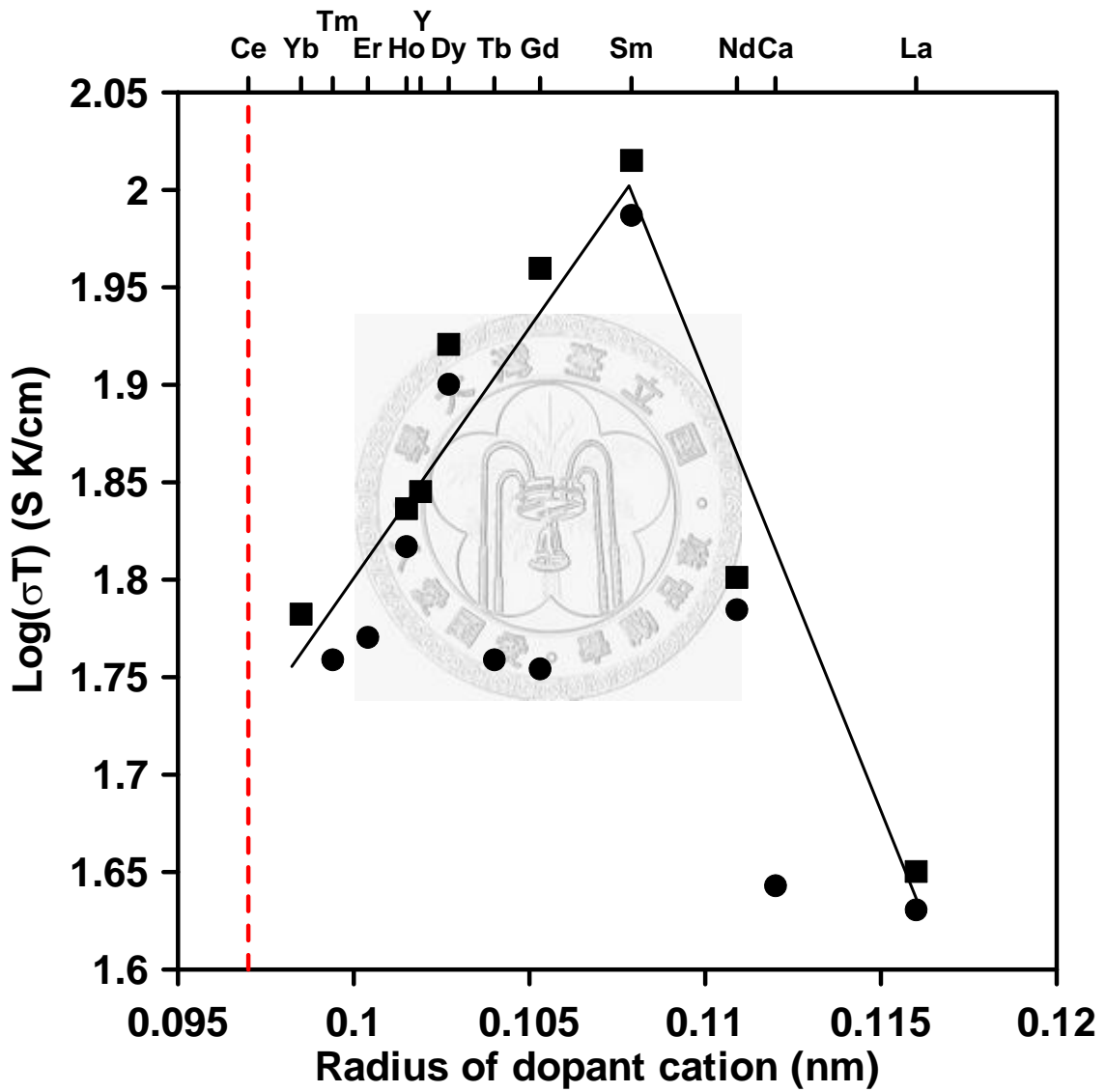


Fig. 2.6 Ionic conductivity of aliovalent doped ceria at 800°C against the radius of dopant cation. (■) Yahiro's work [Yahiro *et al.*, 1988], and (●) Mogensen's work [Mogensen *et al.*, 2000]

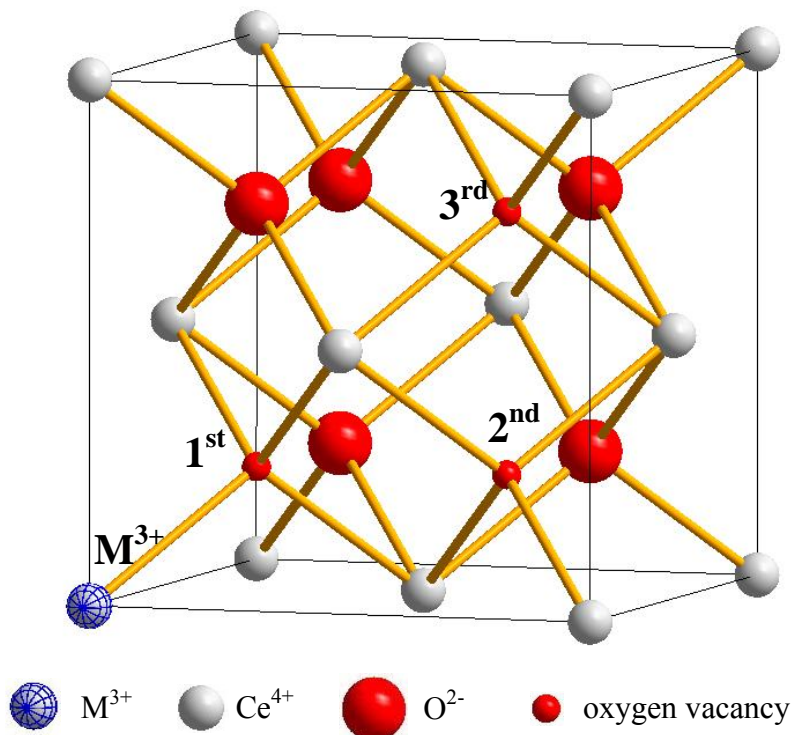
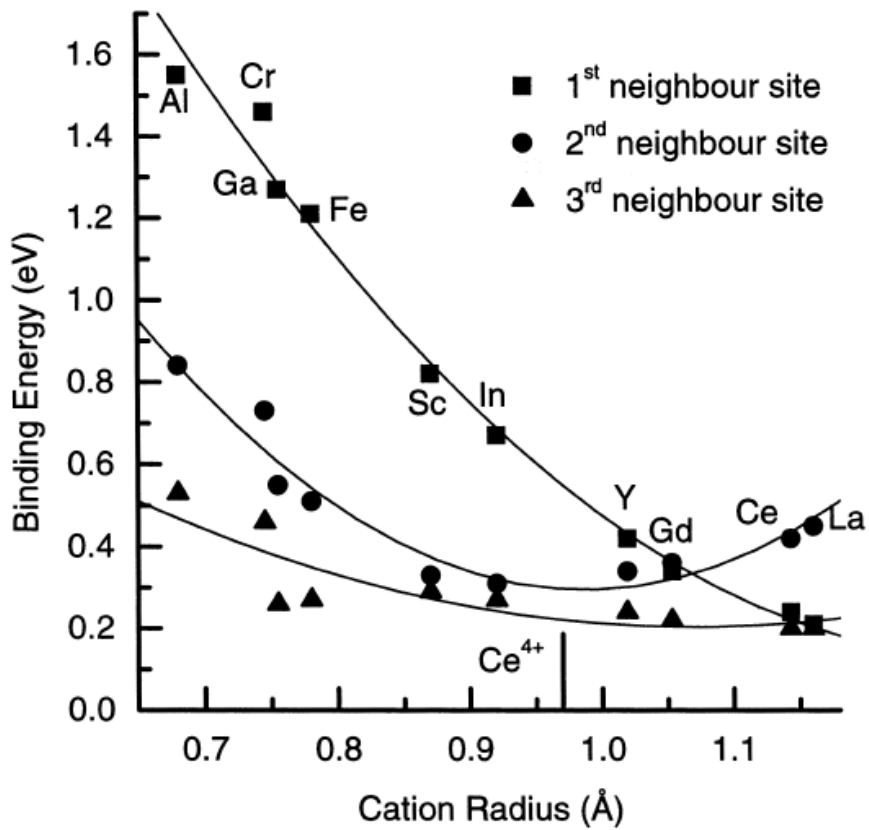


Fig. 2.7 (a) Calculated binding energy of trivalent substitutional ions to an oxygen vacancy<sup>[Minervini *et al.*, 1999]</sup>, (b) configuration of first, second and third neighbor oxygen vacancies with respect to the substitutional trivalent ion in a unit cell.

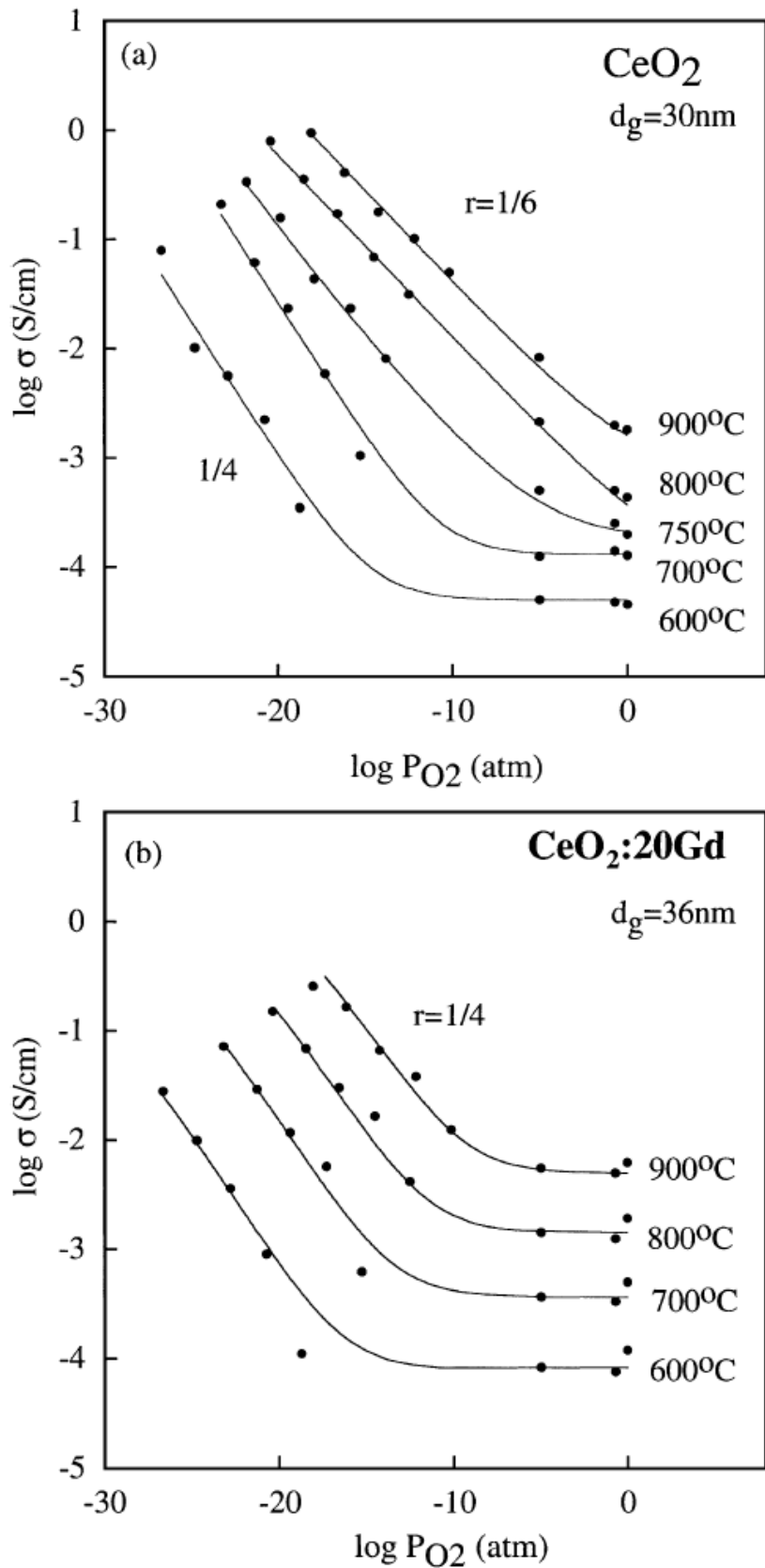


Fig. 2.8 Electrical conductivity of (a) pure ceria and (b) 20GDC system against oxygen partial pressure at different temperature [Suzuki *et al.*, 2002]

**Table 2.2** Ionic conductivities and ionic transference number ( $t_i$ ) of rare earth doped ceria at 800°C [Yahiro *et al.*, 1988]

Sample	Ionic conductivity (S/cm)	Ionic transference number ( $t_i$ )
CeO <sub>2</sub>	$3 \times 10^{-4}$	0.35
Sm <sub>0.20</sub> Ce <sub>0.80</sub> O <sub>1.90</sub>	0.0945	1.00
Dy <sub>0.20</sub> Ce <sub>0.80</sub> O <sub>1.90</sub>	0.0774	0.98
Ho <sub>0.20</sub> Ce <sub>0.80</sub> O <sub>1.90</sub>	0.0639	1.00
Nd <sub>0.20</sub> Ce <sub>0.80</sub> O <sub>1.90</sub>	0.0593	1.00
Er <sub>0.20</sub> Ce <sub>0.80</sub> O <sub>1.90</sub>	0.0574	0.97
Tb <sub>0.20</sub> Ce <sub>0.80</sub> O <sub>1.90</sub>	0.0559	1.00
Tm <sub>0.20</sub> Ce <sub>0.80</sub> O <sub>1.90</sub>	0.0559	1.00
Gd <sub>0.20</sub> Ce <sub>0.80</sub> O <sub>1.90</sub>	0.0553	0.99
La <sub>0.20</sub> Ce <sub>0.80</sub> O <sub>1.90</sub>	0.0416	1.00
Ca <sub>0.20</sub> Ce <sub>0.80</sub> O <sub>1.80</sub>	0.0428	0.99
Y <sub>0.16</sub> Zr <sub>0.84</sub> O <sub>1.92</sub>	0.0301	1.00

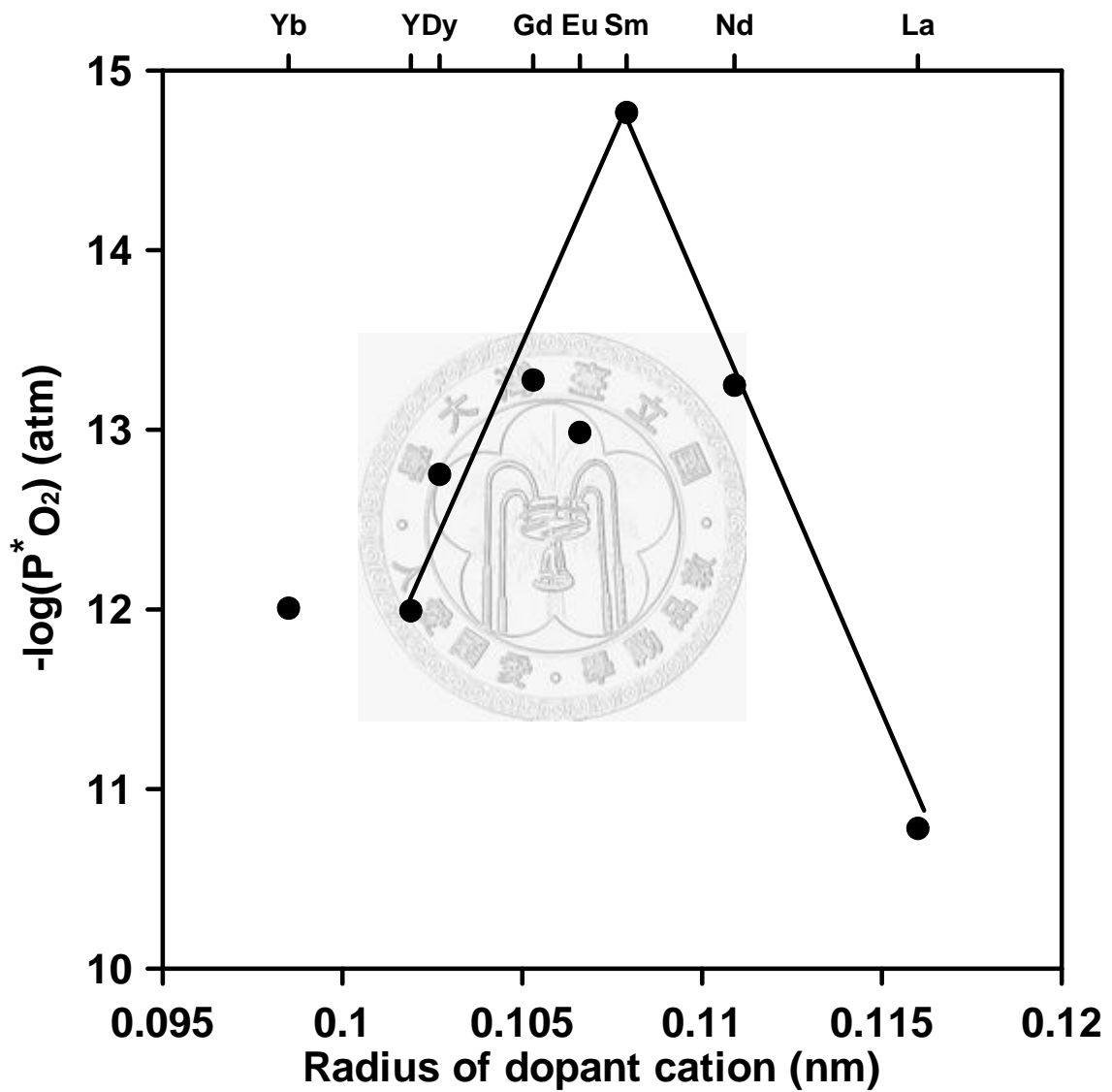


Fig. 2.9 Dopant radius dependence  $P_{O_2}^*$  ( $t_i = 0.5$ ) of doped ceria with rare-earth dopant [Yahiro *et al.*, 1989].

## 2.4 Cathode Materials for SOFC

The cathode, where the oxidant (oxygen or air) is fed, has generally undergone four reaction steps, including the adsorption and dissociation of oxygen molecules, surface diffusion of oxygen atoms to the position of triple phase boundary (TPB), and the electron transferring that forms oxygen ions<sup>[Singhal *et al.*, 2003]</sup>. To complete these steps, there are three basic requirements to the cathode materials in SOFC. First, the structure of the cathode must be porous for gas diffusion. Second, the material must be electronic and ionic conductive, so the collected electrons could be transferred to the dissociated oxygen atoms. Then the oxygen ions diffuse through the cathode material and electrolyte, reaching anode side. Finally, the material must be able to catalyze the reduction of oxygen. In summary, the abilities of oxygen and charge transports are important issues for the cathode material. Any negative effects to the mentioned issues will induce overpotential, such as the concentration and activation polarizations, which lead to poor performance of SOFC. In addition, due to high working temperature of SOFC with YSZ electrolyte (higher than 600°C), the cathode material must hold chemical stability as it contacts with YSZ. Besides, the coefficient of thermal expansion (CTE) of the cathode should be closely match to the other components to avoid the formation of interface crack during thermal cycle<sup>[Singhal, 2000]</sup>.

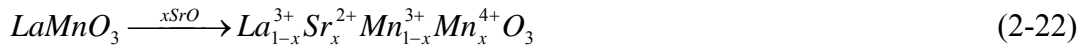


### 2.4.1 LaMnO<sub>3</sub> Materials

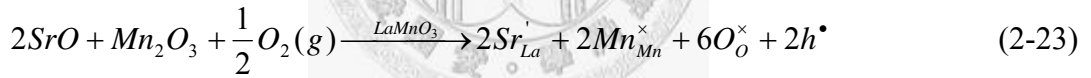
LaMnO<sub>3</sub>, a perovskite oxide, exhibits orthorhombic structure at room temperature. An orthorhombic-rhombohedral transition occurs at about 387°C [van Roosmalen *et al.*, 1995]. The existence of the deficiency, excess and stoichiometry of oxygen in the lattice of LaMnO<sub>3</sub> has been reported in literatures. The stoichiometry or non-stoichiometry of oxygen is a function of temperature and oxygen partial pressure [Kuo *et al.*, 1990]. In an extremely reducing atmosphere, the deficiency of oxygen will lead to the reversible dissociation of LaMnO<sub>3</sub> to La<sub>2</sub>O<sub>3</sub> and MnO phases. On the other hand, the excess of lanthanum (that is, deficiency of manganese) will result in the instability of LaMnO<sub>3</sub> crystal.

Sr-doped LaMnO<sub>3</sub> ((LSM) has the similar crystalline structure as LM, but shows better electric conductivity. However, there is one shortage reported in literature. The diffusion of Mn ions from cathode to YSZ induced the formation of insulating La<sub>2</sub>ZrO<sub>7</sub> and SrZrO<sub>3</sub> [Yang *et al.*, 2003][Østergård, *et al.*, 1995][Hagiwara *et al.*, 2007]. Therefore, the lanthanum deficient (manganese excess) La<sub>1-x</sub>MnO<sub>3</sub> was usually used in the application of SOFCs to suppress the influence of the reaction between cathode material and YSZ [Minh, 1993][Poulsen, 2000]. This A-site deficiency gives the p-type perovskite conductor behavior of the La<sub>1-x</sub>MnO<sub>3</sub>.

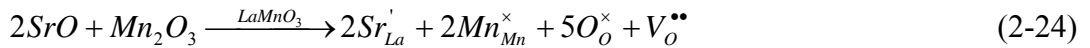
With the substitution of A-site cations ( $\text{La}^{3+}$ ) by lower valence cations, e.g.  $\text{Sr}^{2+}$ , the electrical conductivity of  $\text{LaMnO}_3$  is enhanced. In high oxygen partial pressure atmosphere, LSM performs suitable electrical conductivity for the needs of SOFC [Kuo *et al.*, 1990][Mori *et al.*, 1999][Hwang *et al.*, 2000]. The expression of  $\text{LaMnO}_3$  lattice substituted with SrO dopant can be written as follow [Minh, 1993][Singhal *et al.*, 2003]



It is noted that the tetravalent Mn ion is formed to maintain the local balance of electro-neutrality around the point defect of  $\text{Sr}_{\text{La}}^{\bullet}$ . When a  $\text{La}^{3+}$  ion is replaced by a  $\text{Sr}^{2+}$  ion, the accompanied formation of hole ( $h^{\bullet}$ ) or oxygen vacancy ( $V_{\text{O}}^{\bullet\bullet}$ ) is expressed as following equations [Yang *et al.*, 2003]



and



According to following redox-reaction,



The oxidation or reduction reaction between  $\text{Mn}^{3+}$  and  $\text{Mn}^{4+}$  could be expressed as



Therefore, the doping of SrO induces the concentration increasing of  $h^{\bullet}$  or  $V_{\text{O}}^{\bullet\bullet}$ .

Moreover, with the redox reaction of multi-valence Mn ions, the electrical conductivity of  $\text{LaMnO}_3$  could be enhanced to a level higher than 100 S/cm at 1000°C [Kuo *et al.*, 1990].

It had been mentioned that CTE is another important property for cathode materials. The CTE value of 8YSZ material is 10.5 ppm [Singhal *et al.*, 2003]. Mori [Mori *et al.*, 1999] reported that the CTE of LSM increased from 10.0 ppm to 11.6 ppm as the doping amount of  $\text{Sr}^{2+}$  increasing from 0.0 mol% to 30 mol%, which is very close to YSZ, and suitable for using in YSZ-based SOFC.

#### 2.4.2 Synthesis of LSM Powders

Several methods to fabricate the LSM powders are listed in Table 2.3. Owing to the advantages of low cost and simple processes, solid state reaction is a typical method to fabricate ceramic powders. This route is normally applied by mixing metal oxides or carbonates directly, and followed with thermal treatment at high temperature to form desirable crystalline phase. However, several issues, such as relative higher processing temperature and poor composition distribution, may deteriorate the quality of the ceramic products. In the case of LSM powders, the synthesis of this tri-elements system meets an even more serious problem of composition distribution, and results in multiple phases. In Mori's research [Mori *et al.*, 1999], pure LSM phase could be fabricated at

temperature higher 1400°C for more than 20 hr.

Gas phase synthesis, such as spray pyrolysis, chemical vapor deposition (CVD), and electrostatic spray-assisted vapor deposition (ESAVD) were reported by several researchers. In Hagiwara's reports [\[Hagiwara et al., 2007\]](#)[\[Hagiwara et al., 2007\]](#), LSM/ScSZ composite powder was fabricated by spray pyrolysis procedure. The spherical LSM/ScSZ composite powders were fabricated in four temperature zones which associated with evaporation, dehydration, decomposition and crystallization procedures.

Pinard [\[Pignard et al., 1999\]](#) reported the  $\text{La}_{0.8}\text{MnO}_{3-\delta}$  thin film deposited on MgO,  $\text{LaAlO}_3$ , and  $\text{SrTiO}_3$  single crystals at 650°C via CVD technology. The results of XRD and channeling electron patterns revealed that the smaller the lattice mismatch was, the higher the quality of the crystal could be obtained. Through electrostatic spray-assisted vapor deposition [\[Yan et al., 2008\]](#), a porous layer of pure LSM or LSM-YSZ composite with a thickness of 40  $\mu\text{m}$  was fabricated on dense YSZ substrate where the deposition temperature was 470°C. The as-deposited layer exhibited amorphous phase. After 900°C thermal treatment, the LSM and LSM/YSZ crystalline phases were observed without other phase existence.

Due to high cost of gas phase deposition process, wet chemical synthesis was adapted because the method also supply atomic-scale mixing of  $\text{La}^{3+}$ ,  $\text{Sr}^{2+}$  and  $\text{Mn}^{3+}$  to

fabricate pure and homogeneous LSM phase. In Hsu's research<sup>[Hsu, 2003]</sup>, taking metal nitrates as starting materials and PAA as gelling agent, pure LSM phase was synthesized at temperature as higher as 500°C with the molar ratios of PAA vs. LSM larger than 2. With less amount of PAA, the second phase, La<sub>2</sub>O<sub>3</sub>, was found.

Another chemical synthesis method, "Pechini Method," was also investigated by many researchers. This method was first proposed by Pechini<sup>[Pechini 1967]</sup> in 1967, who used citric acid (CA) as chelator and ethylene glycol (EG) as monomer. Single-phase ANb<sub>2</sub>O<sub>6</sub>, ATiO<sub>3</sub>, and BZrO<sub>3</sub> (A=Ba<sup>2+</sup>, Sr<sup>2+</sup>, Ca<sup>2+</sup>, Mg<sup>2+</sup>, and Pb<sup>2+</sup>; B= Ba<sup>2+</sup>, Sr<sup>2+</sup>, Ca<sup>2+</sup>, and Pb<sup>2+</sup>) powders were successfully synthesized. In this method, the stock solution containing all the starting materials, such as metallic ions, CA and EG were heated to remove the solvent. The polymerization of EG occurred during the heating procedure and forms "resin." The ceramic powders were obtained by calcination of the resin. Other than the above ceramics, lots of ceramic powders were synthesized by this method, including LSM. In Chen's<sup>[Chen *et al.*, 2001]</sup> and Gaudon's<sup>[Gaudon *et al.*, 2002]</sup> studies, LSM powders in average particle size of 50-110 nm were obtained by the thermal treated at  $\geq 600^{\circ}\text{C}$ .

Table 2.3 Comparison of LSM fabrication procedures

Methods	Solid State Reaction	Spray Pyrolysis	Chemical Vapor Deposition	Electrostatic Spary Assisted Vapour Deposition	Sol-Gel Method	Pechini Method
Precursor	Metal oxides or carbonates	Metal nitrates	La(thd) <sub>3</sub> and Mn(thd) <sub>3</sub> , thd=2,2,6,6-tetramethylheptanedione	Metal nitrates	Metal nitrates and PAA	Metal nitrates, citric acid and ethylene glycol
Thermal Treated Temperature	1400°C	Less than 900°C	650°C	900°C	500°C	600°C
Grain Size	N/A	100~200 nm	N/A	N/A	~50 nm	50~110 nm
Characters	N/A	0.5~1.5 μm in diameter spherical LSM/ScSZ composite particle	Small lattice mismatch between substrate and LM gave high quality crystalline growth	Deposited at 470°C As-deposited film with thickness of 40 μm exhibited amorphous phase	PAA/LSM ratio must larger than 2 to obtain pure LSM phase	Grain size decreased with the increase of Sr <sup>2+</sup> content
Reference	[Mori <i>et al.</i> , 1999]	[Hagiwara <i>et al.</i> , 2007] [Hagiwara <i>et al.</i> , 2007]	[Pignard <i>et al.</i> , 1999]	[Yan <i>et al.</i> , 2008]	[Hsu, 2003]	[Chen <i>et al.</i> , 2001] [Gaudon <i>et al.</i> , 2002]

## Chapter 3 Experimental

### 3.1 Materials

In this research, three types of fuel-cell-related components were prepared, including doped CeO<sub>2</sub> fibers, LSM porous cathode layer, dense 8Y-stabilized ZrO<sub>2</sub> (8YSZ) electrolyte.

(1) Gd-doped CeO<sub>2</sub> (GDC) and Sm-doped CeO<sub>2</sub> (SDC) fibers were synthesized by chemical co-precipitation method. The starting materials were cerium (III) nitrate hexahydrate (Ce(NO<sub>3</sub>)<sub>3</sub>·6H<sub>2</sub>O, 99.5%, ACROS, U.S.A.), gadolinium (III) nitrate hexahydrate (Gd(NO<sub>3</sub>)<sub>3</sub>·6H<sub>2</sub>O, 99.5%, ACROS, U.S.A.), samarium (III) nitrate hexahydrate (Sm(NO<sub>3</sub>)<sub>3</sub>·6H<sub>2</sub>O, 99.5%, ACROS, U.S.A.), sodium hydroxide (NaOH, 96%, Showa Chemical Co. Ltd., Japan), and anhydrous citric acid (C<sub>6</sub>H<sub>8</sub>O<sub>7</sub>, 99.5%, ACROS, U.S.A.).

(2) LSM powders were synthesized by two wet chemical processes. First was chemical co-precipitation with polyacrylic acid (PAA, Showa Chemical Co. Ltd., Japan) as gelling agent<sup>[Hsu, 2003]</sup>. The other was synthesized by Pechini method, in which anhydrous citric acid was used as chelator, and ethylene glycol (EG, 99.5%, Riedel-de Haën, Germany) was monomer. In both cases, the starting materials were lanthanum nitrate (La(NO<sub>3</sub>)<sub>3</sub>·6H<sub>2</sub>O, 99.9%, ProChem Inc., U.S.A.), strontium nitrate (Sr(NO<sub>3</sub>)<sub>2</sub>,

98.0%, Showa Chemical Co. Ltd., Japan), and manganese (II) nitrate hexahydrate ( $\text{Mn}(\text{NO}_3)_2 \cdot 6\text{H}_2\text{O}$ , 98.0%, Showa Chemical Co. Ltd., Japan). The commercial LSM powder ( $\text{La}_{0.75}\text{Sr}_{0.2}\text{MnO}_3$ , Lot# 04/06-8.2, B.E.T.=10.27  $\text{m}^2/\text{gm}$ ,  $d_{50}=1.12 \mu\text{m}$ , H. C. Starck, Germany) was selected as standard powder used to analyze the composition of synthesized LSM powders. In addition, the standard powder was also used for the preparation of the paste for screen printing. There were several additives in the LSM aqueous paste, including polyvinyl alcohol (PVA, Grade BP-14, Chang Chun Petrochemical Co., Ltd, Taiwan) as a binder, and Darven-C (Ammonium salt of polymethyl acrylic acid, Venderbilt, USA) as a dispersant.

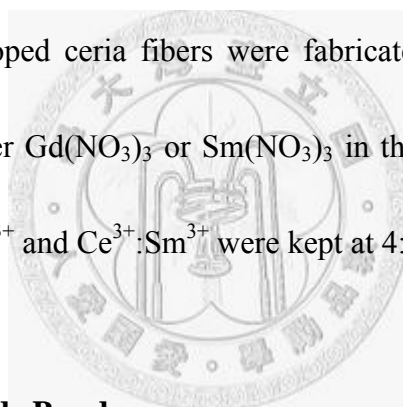
(3) YSZ tape fabricated by tape casting was made by YAGEO, (Taiwan) and the source powder of YSZ was 8 mol% YSZ (TZ-8Y, density= $5.90 \text{ gm}/\text{cm}^3$ , specific surface area= $16 \pm 3 \text{ m}^2/\text{gm}$ , Tosoh, Tokyo, Japan). The NiO/YSZ paste (40 vol% Ni) in organic solvent used for screen printing for the anode was supplied by YAGEO as well. The solid loading of the paste was 48 wt%. The mentioned LSM aqueous paste was also used for screen printing for the cathode.

### 3.2 Synthesis of Doped/Undoped Ceria Fibers

Fig. 3.1 shows the flowchart of the fiber synthesis. Two starting concentrations, 0.025  $m_c$  and 0.1  $m_c$  (molar concentration, moles of solute per kilogram solvent), of



Ce<sup>3+</sup> ions were used in this study. The detail formulas are listed in [Table 3.1](#) and [Table 3.2](#). A solution of Ce(NO<sub>3</sub>)<sub>3</sub> was dissolved in citric acid solution first. NaOH was finally added into the mixture with an appropriate ratio of [NaOH]:[citric acid]. The stock solution was then aged at 90°C for 24 hr until cerium hydrocarbonate fibers were obtained. With different ratios of [NaOH]:[citric acid], four types of the precipitates were obtained, including colloidal particles, fibers, stick-in-bundles and flakes. Cerium hydrocarbonate fibers were further thermally treated at high temperature to form ceria fibers. Gd-doped or Sm-doped ceria fibers were fabricated with the same procedure except the addition of either Gd(NO<sub>3</sub>)<sub>3</sub> or Sm(NO<sub>3</sub>)<sub>3</sub> in the starting solution, of which the molar ratios of Ce<sup>3+</sup>:Gd<sup>3+</sup> and Ce<sup>3+</sup>:Sm<sup>3+</sup> were kept at 4:1.



### 3.3 Fabrication of Cathode Powders

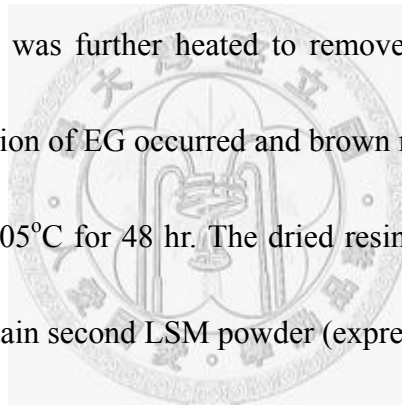
#### 3.3.1 Sol-Gel Synthesis

[Fig. 3.2](#) shows the flowchart of LSM synthesis by sol-gel method with PAA as gelling agent. La(NO<sub>3</sub>)<sub>3</sub>, Sr(NO<sub>3</sub>)<sub>2</sub>, and Mn(NO<sub>3</sub>)<sub>2</sub> were added into deionized (D.I.) water in a ratio of La<sup>3+</sup>:Sr<sup>2+</sup>:Mn<sup>2+</sup>=0.8:0.2:1.0, then stirred for 30 min. PAA was then added into the stock solution with a molar ratio of PAA/LSM=2. After 30 min stirring, the solution was drying at 105°C for 48 hr. The formed “cake” was ground and calcined

to obtain first LSM powder (expressed as A-LSM).

### 3.3.2 Pechini Method

Fig. 3.3 shows the flow chart of LSM synthesis by Pechini method.  $\text{La}(\text{NO}_3)_3$ ,  $\text{Sr}(\text{NO}_3)_2$ , and  $\text{Mn}(\text{NO}_3)_2$  were dissolved in D.I. water in a ratio of  $\text{La}^{3+}:\text{Sr}^{2+}:\text{Mn}^{2+}=0.8:0.2:1.0$ . The acidic mixture was heated to  $70^\circ\text{C}$ . Then citric acid was added with stirring of the mixture. After 1 hr stirring, EG was finally added into the mixture. The temperature of the mixture was further heated to remove the solvent. As the solvent evaporated, the polymerization of EG occurred and brown resin was formed in 3 hr. The resin was further dried at  $105^\circ\text{C}$  for 48 hr. The dried resin was ground and calcined at specified temperature to obtain second LSM powder (expressed as P-LSM).



## 3.4 Single Cell Fabrication

### 3.4.1 Fabrication of Dense YSZ Thin Plate

100  $\mu\text{m}$  thick green tape produced by YAGEO was cut into suitable size first. Then the thin plate was sintered at  $1500^\circ\text{C}$  for 1 hr in air. The relative density achieved is nearly 100% theoretical density (T.D.). To avoid the warpage of the plate, a Y-ZrO<sub>2</sub> block placed on the plate during sintering was necessary. This procedure was applied by

putting the plate between a ZrO<sub>2</sub>-block (10 cm × 10 cm × 5 mm in dimensions, Bell New Ceramics Co., Ltd, 富源瓷器, Taiwan) as a bottom, and a porous ZrO<sub>2</sub>-piece (26 g, 6.8 cm × 6.8 cm × 2 mm in dimensions, Tai Yiach Enterprise Co., Ltd, 台溢企業, Taiwan) as a cover. The block made by 3YSZ was chosen to prevent contamination during sintering procedure.

### **3.4.2 Anode and Cathode Thin Film Fabrication**

Through screen printing, the NiO/YSZ anode and LSM cathode thin film were fabricated on the YSZ plate. The commercial LSM powder was added in the mixture of Darven-C dispersant and water. The paste was then ball-milled with 3YSZ media for 24 hr. A 10 wt% PVA solution was added into the slurry and underwent additional ball-milling for 72 hr. The obtained LSM paste consisted of 60 wt% LSM powder, 2 wt% Darven-C (based on powder), and 3 wt% PVA. The anode and cathode pastes were screen-printed through a 150-mesh screen on YSZ plate with designed pattern. After drying at room temperature, the single cell was thermal treated at 1200°C for 1 hr in air.

## **3.5 Characterization**

### **3.5.1 ICP-AES Analysis**

The residual concentration of metallic ions (Ce, Gd, and Sm) in the supernatant of fiber synthesis was analyzed by inductive coupled plasma with atomic emission spectroscopy (ICP-AES, JOBIN YVON, Ultima 2000, France). The testing solutions were sampled from the aging solution and filtrated to remove all the suspended particles before measurement. A further dilution of the filtrated solution to reduce all the ionic concentrations down to the appropriate values (less than 100 ppm) was conducted before the test by ICP-AES. A standard solution (10  $\mu\text{g/mL}$ , Multi element Solution Standard 1, Matrix per Volume: 5%  $\text{HNO}_3$  per 125 mL, SPEX CertiPrep, U.S.A.) was used to calibrate the concentration of Ce, Sm and Gd ions in samples. Besides, the composition of GDC and SDC fibers were also quantified with this ICP-AES technology. A known quantity of hydrocarbonate fibers was first dissolved in nitric acid ( $\text{HNO}_3$ , 65%, Riedel-de Haën, Germany) under the hydrothermal condition of  $240^\circ\text{C}$ , 60 bar for 100 min by microwave digest system (Multiwave 3000, Anton Paar GmbH, Graz, Austria). Then the transparent solutions were further diluted before ICP-AES analysis.

### **3.5.2 Density Measurement**

The relative density of sintered 8Y-YSZ plate was measured by Archimedes

method. The sintered 8Y-YSZ plate was immersed in D.I. water. A few drops of n-pentyl alcohol (98.0%, Hanawa, Osaka, Japan) were added into the water as defoaming agent, and vacuumed for 4 hr to eliminate the bubble trapped on surface of sintered body. The total porosity  $f_p$  (in fraction) is obtained according to following equation<sup>[Kingery, 1976]</sup>.

$$f_p = \frac{d_t - d_b}{d_t} = 1 - \frac{d_b}{d_t} \quad (3-1)$$

where  $d_b$  is bulk density and  $d_t$  is true density. The relative density could be calculated by subtracting  $f_p$  from 1. The  $d_t$  value of 8Y-YSZ is 5.90 gm/cm<sup>3</sup> provided by Tosoh.  $d_b$  is calculated from the equation below.

$$d_b = \frac{\text{total mass}}{\text{total volume, including pores}} = \frac{w_a}{(w_{sat} - w_{sus}) / d_w} \quad (3-2)$$

where  $w_a$  is the mass of dried body in air,  $w_{sus}$  is the mass of sample suspended in water,  $w_{sat}$  is the mass of sample whose open pores are full of water in air, and  $d_w$  is the density of the water.

### 3.5.3 Thermal Analysis

To identify the appropriate calcination temperature of GDC fibers and LSM powders, differential thermal analysis (DTA)/thermogravimetric (TG) analysis (Seiko Instruments Inc., EXSTAR 6000 TG/DTA, Japan) were conducted. The sample powder

and reference material ( $\text{Al}_2\text{O}_3$ ) were individually put in two Pt crucibles and sent into a heating chamber. The mass changes and temperature difference between sample and the reference were recorded during the heating. The measurement was conducted in atmosphere. The flow rate of air was 150 mL/min. The temperature ramp rate was either  $10^\circ\text{C}/\text{min}$  or  $3^\circ\text{C}/\text{min}$  depending on different samples. The sample was cooled down to room temperature in the chamber.

#### **3.5.4 BET Measurement**

The specific surface area of thermal treated GDC fibers and LSM powders was measured by Brunauer-Emmett-Teller (B.E.T.) method with the instrument (Micromeritics, ASAP2000 and TriStar 3000, U.S.A.). The sample was put in a quartz tube. After de-gassing procedure ( $150^\circ\text{C}$  in vacuum for 10 hr), the sample was cooling to the temperature of liquid nitrogen. Specific surface area could be calculated by single-point method from the adsorption amount of  $\text{N}_2$  gas adsorbed on the surface of sample.

#### **3.5.5 Residual Carbon Analysis**

The residual carbon of thermal treated LSM powders were analyzed by Carbon/Sulfur analyzer (EMIA-220V, HORIBA, Kyoto, Japan). The sample was placed

in a ceramic crucible with the mixture powder of tungsten, tin, and iron particles as flux. The mixture was heated by a high frequency induction furnace with the input of pure O<sub>2</sub> to oxidize all the residual carbon and sulfur to gaseous carbon dioxide and sulfur dioxide. The gases were detected by infrared analyzer to measure the amount of vaporized carbon and sulfur in the sample.

### 3.5.6 Microstructural Analysis and Phase Identification

(1) **SEM Observation:** Fibrous, flake-shape, and stick-in-bundle precipitates were washed by D.I. water for 5 times to remove residual metallic ions and citric acid before observation. The naked sintered YSZ plate was ultrasonically washed in D.I. water, then in ethanol for 3 times to remove surface contamination before observation. Grain size of YSZ was measured by lineal intercept method. The morphologies of electrolyte supported SOFC, including top views and fracture surface were directly observed without other treatments. The morphologies and chemical composition of GDC precipitates were observed by scanning electron microscopy (SEM, field emission, model 1530, LEO Instrument, England) equipped with energy-dispersive spectroscopy (EDS, EDAX Corp., U.S.A.).

The composition of LSM powders were analyzed by quantitative analysis with

SEM-EDS. The standard for quantitative analysis was prepared by the commercial LSM powders (H. C. Starck, Germany). The commercial powder was uniaxially die-pressed with 100 MPa pressure into a disc with 6 mm in diameter and then sintered at 900°C for 1 hr in air. The synthesized LSM powders were calcined at 400°C for 1 hr first. The following preparation procedures of specimens were the same with the standard sample.

The conditions of quantitative analysis were set as below, 15 kV of e-beam voltage, the electron probe size was about 1~1.5 nm, the tilt angle of sample was 15°, the intensity (counts per second, CPS) was controlled at about 1000-1200, and the working distance (WD) was kept at 8.5 mm. The X-ray intensity for the analysis was L peak for Sr and La, K peak for Mn.

**(2) TEM Observation:** Oxide fibers and LSM powders were dispersed in pure ethanol (99.5%, Shimakyu's Pure Chemicals, Japan). A copper grid covered by carbon film was dipped in the suspension for sampling. The copper grid was dried in air, and then vacuumed to eliminate all the remained solvent before observation. The microstructures of the powders on carbon film were observed by transmission electron microscopy (TEM, 100 CXII, JEOL Co., Japan). The operation voltage was 100 keV. The crystalline phases of the powders were identified from diffraction pattern.

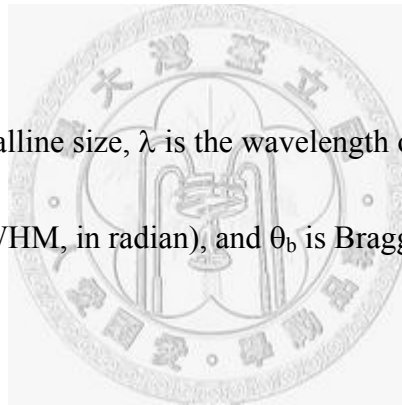


### 3.5.7 XRD Analysis

The crystalline phase of hydrocarbonate fibers, thermal treated ones, and LSM powders were analyzed by X-ray diffraction (XRD, Philips PW1830, Philips Instrument Corp., Netherlands) using Cu  $K_{\alpha}$  radiation, of which the wavelength of X-ray was 1.5406 Å. The scanning rate was 4°/min, the applied voltage and current were 40 kV and 30 mA, respectively. The crystalline size of powder samples was calculated with Scherrer formula<sup>[Cullity *et al.*, 2001]</sup>:

$$t = \frac{0.9\lambda}{B \cos \theta_b} \quad (3-3)$$

where  $t$  is the average crystalline size,  $\lambda$  is the wavelength of X-ray (1.5406 Å),  $B$  is full width at half maximum (FWHM, in radian), and  $\theta_b$  is Bragg angle (in radian).



### 3.5.8 Electrical Properties Measurement

#### (1) DC Electrical Measurement

The area-specific resistance (ASR,  $\Omega \cdot \text{cm}^2$ ) of cathode polarization was measured by 3-terminal measurement<sup>[Barsoukov *et al.*, 2005][Yang, 2003]</sup>. ASR is a dimensionally dependant material property. The scheme of electrodes and fixture of the measurement is shown in Fig. 3.4. The electrode material of working electrode (WE) was the coated LSM layer been thermally treated at 1200°C for 1 hr in air. The material of counter electrode (CE)

and reference electrode (RE) was silver paste which was pre-treated (baking) at 500°C before testing. The role of RE was to isolate the overpotential of WE from the entire half cell. Therefore, the voltage drop of WE itself and the interface of WE and electrolyte could be measured.

The 8YSZ electrolyte was fabricated by uniaxially die-pressed at a pressure of 30 MPa into a disc with 20 mm in diameter. The green disc was sintered at 1500°C for 1 hr in air. The LSM was coated on the electrolyte by spray coating. To control the remained carbon content of LSM powders, the A-LSM and P-LSM powders were thermal treated with different conditions, as shown in [Fig. 3.5](#). The 400°C calcined LSM powders were prepared as a suspension with solid loading of 20 wt%, and followed with ball-milling for 20 hr with 3YSZ media. After spray coating, the LSM film was thermal treated at 1200°C for 1 hr in air to form a LSM/YSZ half cell.

A current source (Keithley 224, Keithley, U.S.A.), a digital multimeter (7555, YOKOGAWA, Japan), and an electronic load (E-load, Agilent N3301A, Agilent, U.S.A.) were connected to the specimen with silver wires (0.5 mm in diameter) to carry out the measurement. The current input was manual control. The voltage variation was monitored and recorded by personal computer via general purpose instrumentation bus (GPIB) interface. The monitoring and recording software was written with laboratory

virtual instrument engineering workbench (LabVIEW) program. The original code of the software is shown in [Fig. 3.6](#).

## **(2) Electrochemical Impedance Spectroscopy Measurement**

Electrochemical Impedance Spectroscopy (EIS) is a technique to investigate the properties of fuel cell. A small amplitude of alternating current (AC) signal is applied to the cell under test. The response signal was detected and analyzed to obtain the impedance of the cell. The EIS of 1500°C sintered YSZ plate was measured by frequency response analyzer (FRA, Solartron Analytical Co., UK). The measured frequency range was from 0.01 Hz to 1 MHz with the amplitude of AC voltage of 10 mV. The measurement was performed in the temperature range between 300°C and 700°C.

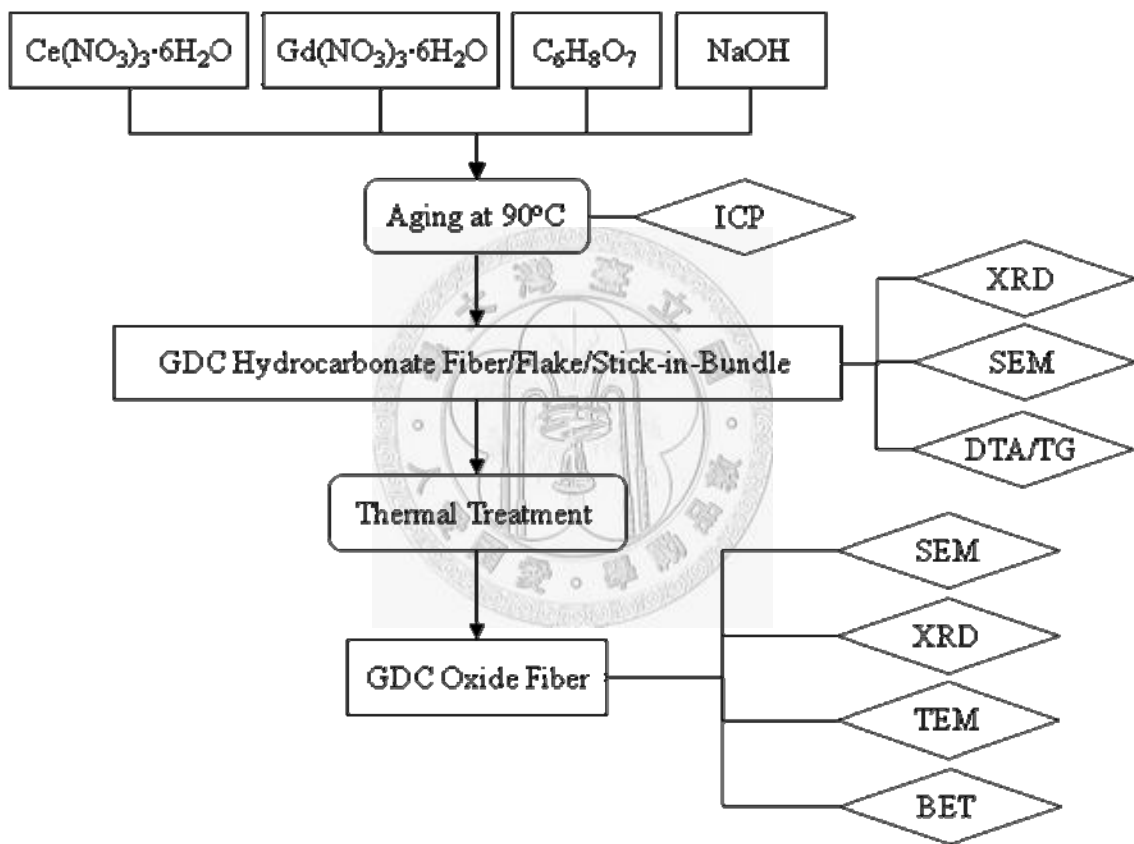


Fig. 3.1 Experimental flowchart of GDC fiber synthesis.

**Table 3.1** Formulations of the synthesis of cerium hydrocarbonate fiber,  $[Ce^{3+}] = 0.025 \text{ m}_c$

No.	concentration(M)			NaOH/C <sub>6</sub> H <sub>8</sub> O <sub>7</sub>	morphology
	Ce(NO <sub>3</sub> ) <sub>3</sub>	C <sub>6</sub> H <sub>8</sub> O <sub>7</sub>	NaOH		
1	0.025	0.1	0.01	0.1	stick-in-bundle
2	0.025	0.1	0.02	0.2	stick-in-bundle
3	0.025	0.1	0.06	0.6	flake
4	0.025	0.1	0.075	0.75	flake
5	0.025	0.1	0.1	1	flake
6	0.025	0.1	0.12	1.2	flake
7	0.025	0.1	0.14	1.4	flake
8	0.025	0.1	0.16	1.6	flake
9	0.025	0.2	0.02	0.1	stick-in-bundle
10	0.025	0.2	0.04	0.2	stick-in-bundle
11	0.025	0.2	0.06	0.3	stick-in-bundle
12	0.025	0.2	0.075	0.375	stick-in-bundle
13	0.025	0.2	0.12	0.6	flake
14	0.025	0.2	0.14	0.7	flake
15	0.025	0.2	0.16	0.8	flake
16	0.025	0.2	0.18	0.9	flake
17	0.025	0.2	0.2	1	flake
18	0.025	0.25	0.15	0.6	flake
19	0.025	0.3	0.075	0.25	stick-in-bundle
20	0.025	0.4	0.075	0.188	stick-in-bundle

Note: all samples were aging at 90°C for 24 hr.

Table 3.1 Continued

No.	concentration(M)			NaOH/C <sub>6</sub> H <sub>8</sub> O <sub>7</sub>	morphology
	Ce(NO <sub>3</sub> ) <sub>3</sub>	C <sub>6</sub> H <sub>8</sub> O <sub>7</sub>	NaOH		
21	0.025	0.5	0.02	0.04	stick-in-bundle
22	0.025	0.5	0.04	0.08	stick-in-bundle
23	0.025	0.5	0.06	0.12	stick-in-bundle
24	0.025	0.5	0.075	0.15	stick-in-bundle
25	0.025	0.5	0.1	0.2	stick-in-bundle
26	0.025	0.5	0.12	0.24	stick-in-bundle
27	0.025	0.5	0.14	0.28	stick-in-bundle
28	0.025	0.6	0.02	0.033	stick-in-bundle
29	0.025	0.6	0.075	0.125	stick-in-bundle
30	0.025	0.7	0.02	0.029	stick-in-bundle
31	0.025	0.7	0.075	0.107	stick-in-bundle
32	0.025	0.8	0.02	0.025	stick-in-bundle
33	0.025	0.8	0.04	0.05	stick-in-bundle
34	0.025	0.8	0.075	0.094	stick-in-bundle

Note: all samples were aging at 90°C for 24 hr.

**Table 3.2** Formulations for the synthesis of cerium hydrocarbonate synthesis,  $[Ce^{3+}] = 0.1$  m<sub>c</sub>

No.	Concentration (m)			NaOH/C <sub>6</sub> H <sub>8</sub> O <sub>7</sub>	Morphology
	Ce(NO <sub>3</sub> ) <sub>3</sub>	C <sub>6</sub> H <sub>8</sub> O <sub>7</sub>	NaOH		
<b>1</b>	0.1	0.5	0.3	0.6	fiber
<b>2</b>	0.1	0.4	0.3	0.75	fiber
<b>3</b>	0.1	0.6	0.3	0.5	fiber
<b>4</b>	0.1	0.8	0.3	0.375	fiber
<b>5</b>	0.1	1	0.3	0.3	fiber
<b>6</b>	0.1	0.1	0.1	1	fiber
<b>7</b>	0.1	0.2	0.1	0.5	stick-in-bundle
<b>8</b>	0.1	0.4	0.1	0.25	stick-in-bundle
<b>9</b>	0.1	0.5	0.1	0.2	stick-in-bundle
<b>10</b>	0.1	1	0.1	0.1	stick-in-bundle
<b>11</b>	0.1	1	0.5	0.5	fiber
<b>12</b>	0.1	0.5	0.5	1	flake
<b>13</b>	0.1	1.1	0.5	0.45	fiber
<b>14</b>	0.1	0.3	0.5	1.67	flake
<b>15</b>	0.1	0.5	0.4	0.8	flake

Note: all samples were aging at 90°C for 24 hr.

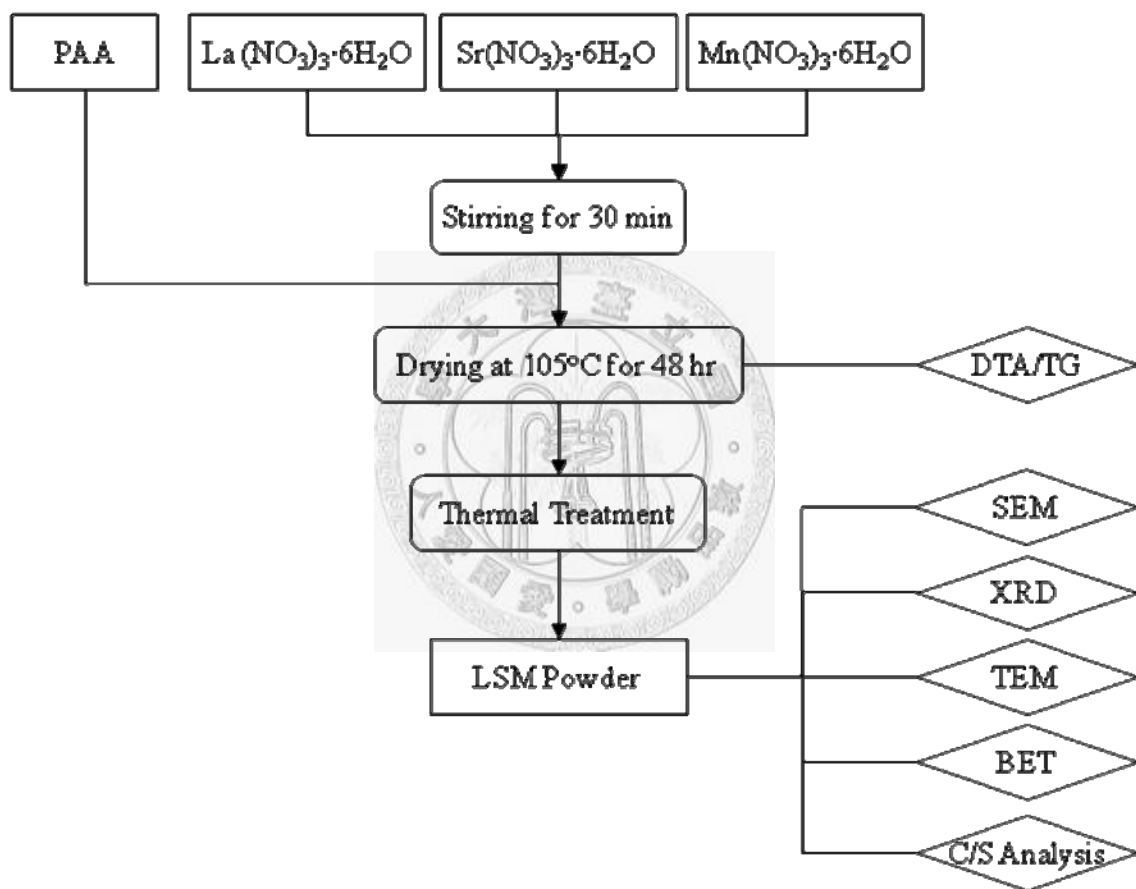


Fig. 3.2 Experimental flowchart of LSM powder synthesized by sol-gel process with PAA as gelling agent.



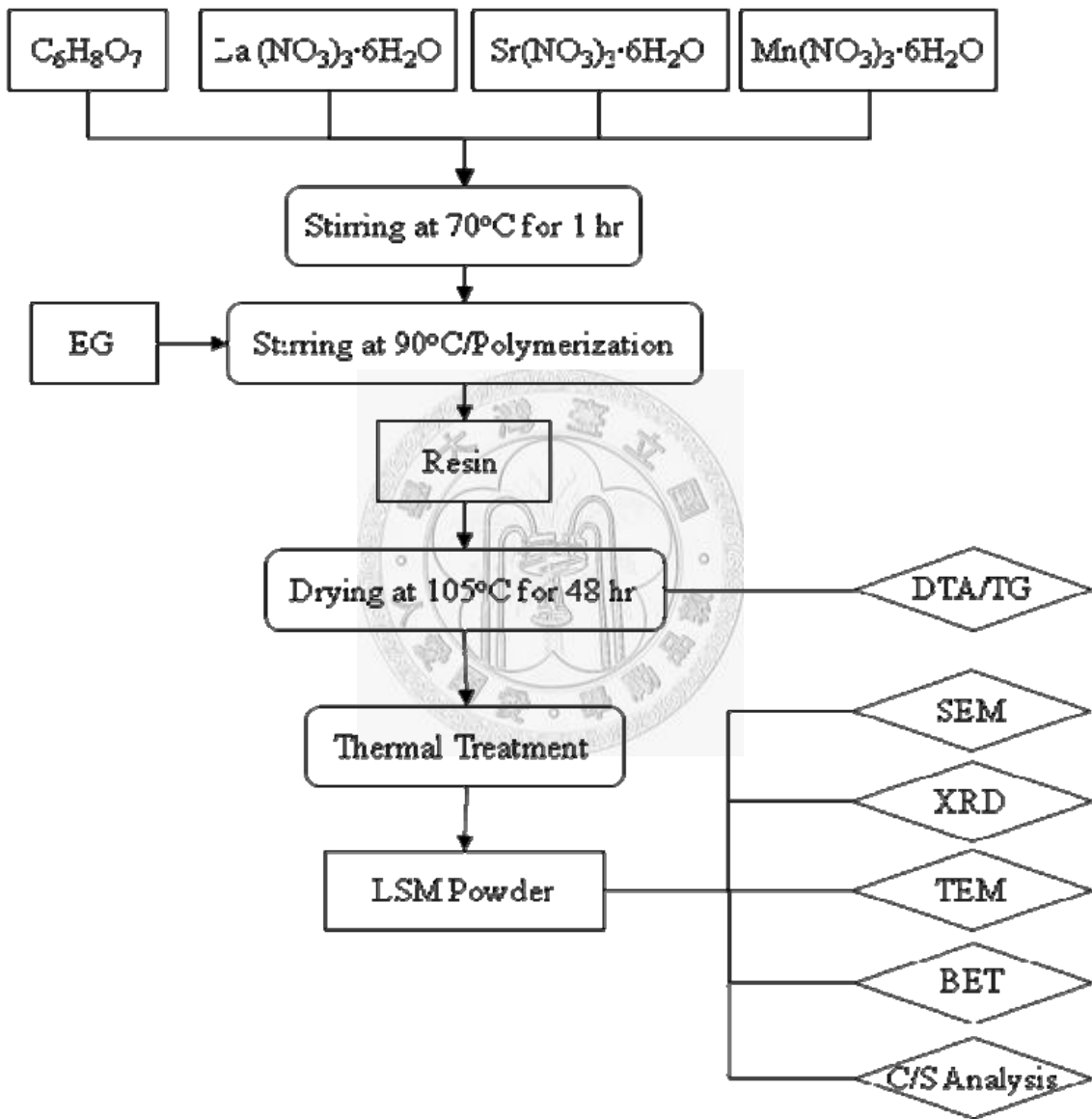


Fig. 3.3 Experimental flowchart of LSM powder synthesized by Pechini method.

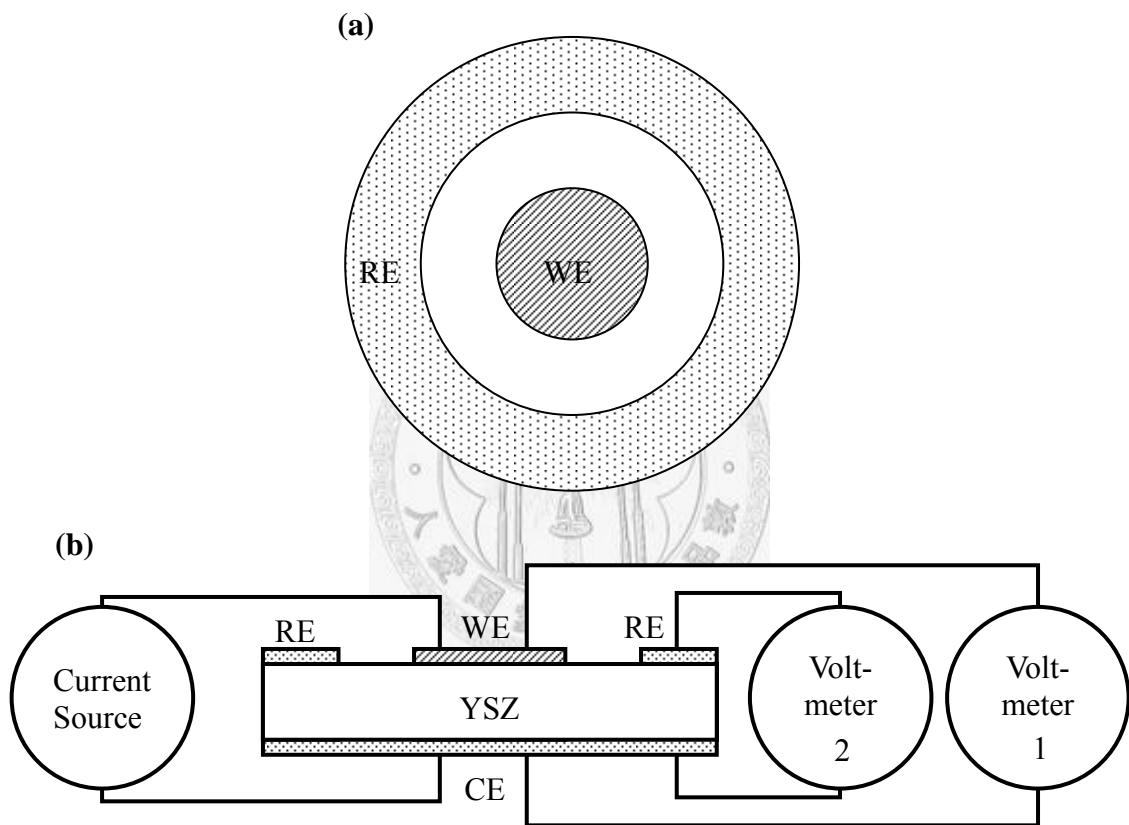
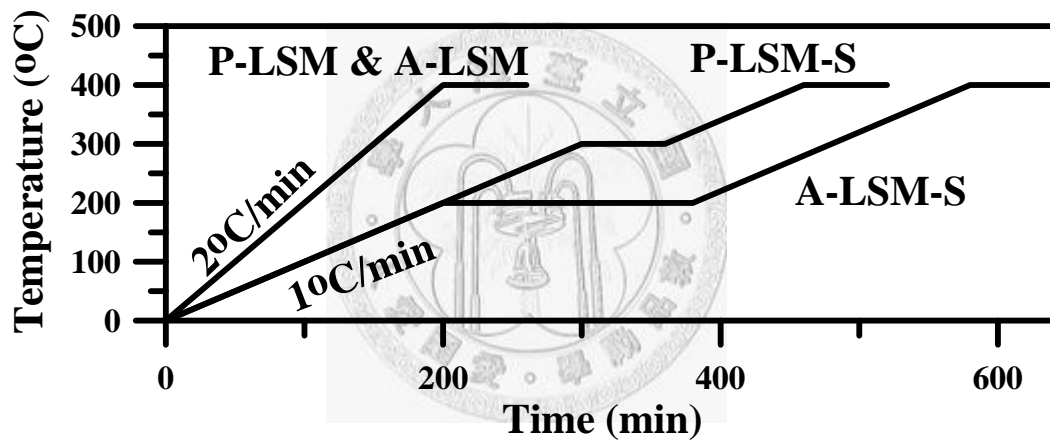


Fig. 3.4 (a) Top view of the electrodes, and (b) side view of the configuration scheme of 3-terminal electrical measurement.



**Fig. 3.5** Thermal treatment procedures of LSM powders. All the treatment was conducted in atmosphere. The procedure of P-LSM and A-LSM was 2°C/min to 400°C, then holding for 1 hr. The ramp rate of P-LSM-S and A-LSM-S was 1°C/min, and the isothermal treatment was 1 hr at 300°C for P-LSM-S and 3 hr at 200°C for A-LSM-S.

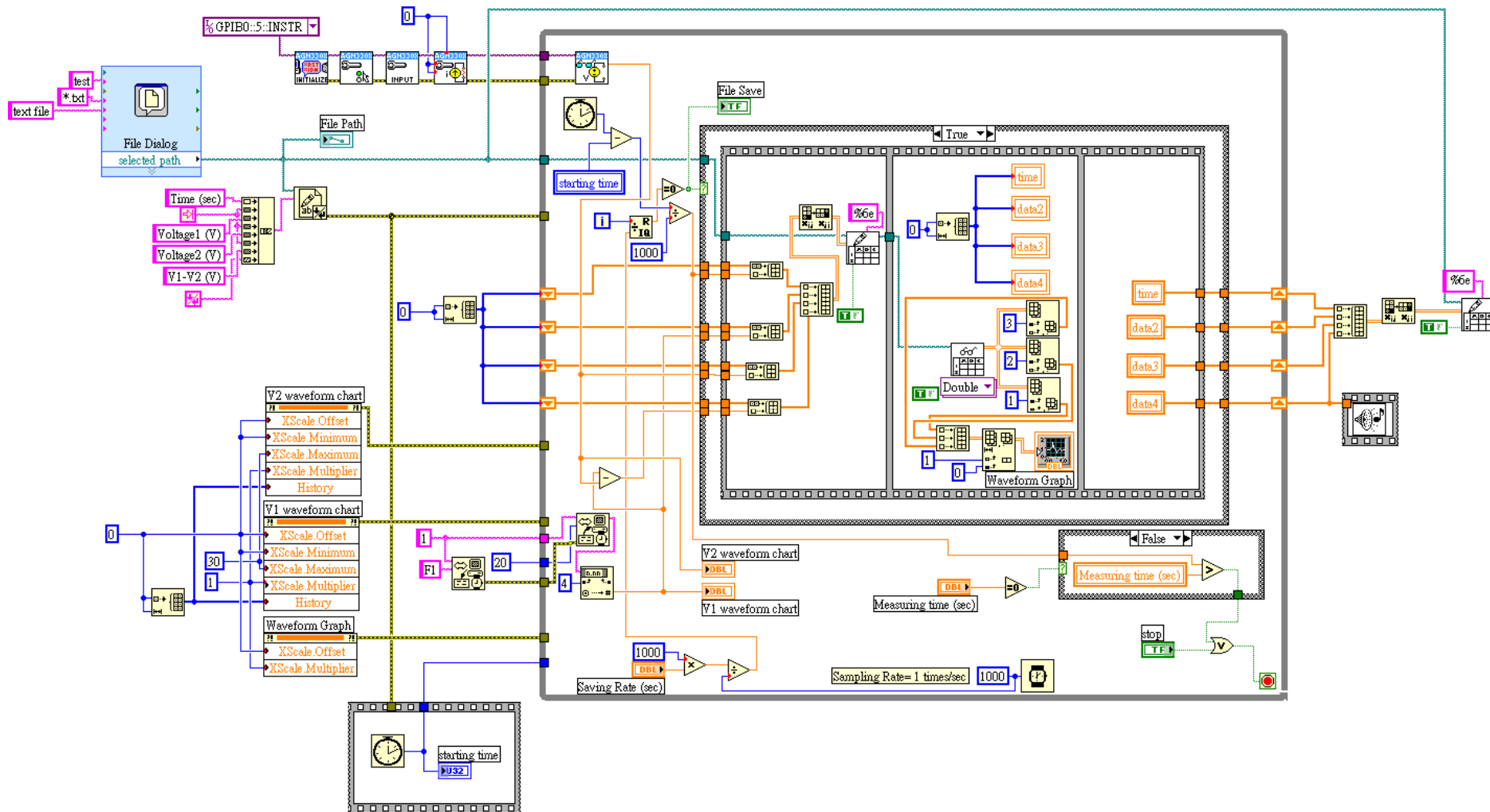


Fig. 3.6 Block diagram (original code) of 3-terminal electrical measurement monitoring software.

## Chapter 4 Results and Discussions

### 4.1 Synthesis of CeO<sub>2</sub> (GDC and SDC) Fibers

#### 4.1.1 Effects of Sodium Hydroxide/Citric Acid

There were three kinds of Ce-precipitations could be obtained after 24 hr aging at 90°C, including fibrous, flake-shape, and stick-in-bundle precipitates. Fig. 4.1 schematically shows the evolution of starting solutions during the aging period, and the precipitates growth in three cases.

In the synthesis of fibrous precipitates, there were several morphologic changes of the starting solution during the aging period. The colorless transparent solution first turned to turbid suspension in less than 1 hr. As the solution aging, the suspension formed some precipitates to the bottom of container, and the supernatant solution became transparent. The sediment, which covered the entire bottom of glass container, underwent next transition from porous precipitates to loose agglomerates, which were visual by naked eyes. If agitating by ultrasonic bath, the matter coming off the agglomerates was fibers, as observed by SEM. In other words, the fiber was “growing” from the loose agglomerates possibly by dissolution-precipitation process on the bottom of the container.

In the case of the synthesis of flake-shape precipitates, the change of starting

solution was similar with the previous one. No precipitates and loose agglomerates were found in the turbid suspension. Instead, flake-shape precipitates could be observed after washing and drying of the suspended particles obtained from the suspension. The morphologies of flake-shape precipitates are shown in Fig. 4.2(a).

Finally, the evolution of the solution for growing stick-in-bundle precipitation was different from the others. Lots of the bundles were formed, and became larger as the aging proceeded. The transparent solution stayed the same as it was in the whole aging period. The microstructure of the bundles is shown in Fig. 4.2(b), of which these sticks grow radiantly from centers.

Fig. 4.3 shows the composition domains for synthesizing cerium hydrocarbonate precipitates. Two starting concentrations of cerium ( $0.025 m_c$  and  $0.10 m_c$ ) ions were tried, and the aging time was kept for 24 hr. It is apparent that the shape of the cerium hydrocarbonate precipitates was closely affected by the ratio of  $[\text{NaOH}]:[\text{C}_6\text{H}_8\text{O}_7]$ . Taking the ratio equals to 0.5 as an example, the domain in Fig. 4.3(a) was separated into two main regions only, which contain either the stick-in-bundle or the flake-shape precipitates, as shown in Fig. 4.2. As the aging time lasting longer, e.g. 35 hr, the solutions of the  $[\text{NaOH}]/[\text{C}_6\text{H}_8\text{O}_7]$  ratio between 0.5 and 0.8 grew fibrous precipitates, instead of flakes <sup>[Sung *et al.*, 2007]</sup>.

In order to understand the effect of cerium concentration and to increase the quantity of fibrous precipitates, the concentration of cerium solution was increased to 0.10 m<sub>c</sub>. The precipitation result is shown in Fig. 4.3(b). The detail formulas of the samples have been listed in Table 3.2. With a higher concentration of starting Ce precursor, the time required to form the fibrous precipitate was shortened to less than 12 hr. Besides, the processing window of fiber synthesis was enlarged. The stick-in-bundle and flake-shape precipitates were only observed in the extremely low or large [NaOH]/[C<sub>6</sub>H<sub>8</sub>O<sub>7</sub>] ratios. In Fig. 4.4(a), the fibrous precipitates were synthesized in 12 hr with the ratio equal to 0.6. When the ratio was 0.8, flake-shape precipitate was observed in 24 hr as shown in Fig. 4.4(c). In Fig. 4.4(d), fibrous precipitate could be synthesized with a longer period of aging 62 hr for the case with the ratio of 0.8. On the other hand, since the fibers appeared, the precipitate had reached their stable state. There were no other kinds of Ce-precipitate could be found within 60 hr aging period.

#### 4.1.2 Kinetic Analysis of Fiber Synthesis

Fig. 4.5 shows the doped cerium hydrocarbonate fibrous precipitates with Gd<sup>3+</sup> and Sm<sup>3+</sup>, respectively. There was a limited effect of the additives to the fibrous morphology. The result of quantitative analysis of two fibers by ICP-AES is listed in Table 4.2. The

contents of Gd and Sm in doped cerium hydrocarbonates fibers are 17.3 mol% and 16.0 mol%, respectively, less than the original quantities of 20 mol%. Loss of Gd and Sm content is occurred for both doping system. The slower deposition rate of Gd and Sm ions than Ce ions during the aging period was responsible for this content deficiency.

The residual concentrations of Ce ([Ce]) and Gd ([Gd]) ions in the supernatant are shown in Fig. 4.6. The linear decrease of the [Ce] and [Gd] species indicated the zero-order reaction of the precipitation. The deposited fractions of Ce and Gd ionic concentrations from the solution were about 91.1% and 83.8%, respectively.

The residual [Ce] in supernatant of three different solutions (samples 1, 14, and 10 in Table 3.2) growing their Ce-precipitates were also analyzed by ICP-AES. The results are shown in Fig. 4.7, of which shows different time dependence of [Ce] content. The sample 1 keep constant precipitation rate. 10 hr later, the concentration of [Ce] turns constant at 450 ppm. For this zero-order reaction, the reaction rate is independent of the concentrations of reactants. As a result, reaction time is the only controlling fact to the residual concentration. The relationship between residual concentration and time could be expressed as follow.

$$R = -\frac{d[C]}{dt} = k \quad (4-1)$$

where  $R$  is reaction rate,  $[C]$  is the concentration of Ce,  $t$  is reaction time, and  $k$  is



reaction rate coefficient. In this investigation, the units of  $[C]$ ,  $t$ , and  $k$  were ppm, hr, and ppm/hr, respectively. Integrating Eq. (4-1), the following equation is obtained.

$$[C]_t = [C]_0 - k(t - t_0) \quad (4-2)$$

where  $[C]_t$  is reactant concentration at time  $t$ ,  $[C]_0$  is original reactant concentration, and  $t_0$  is starting time which is normally zero. The linear relationship between  $[C]_t$  and  $t$  is obtained. The minus slope of the  $[C]_t$  plotted against time gives the reaction rate coefficient,  $k$ . From the results of ICP-AES, the value of  $k$  was 1371 ppm/hr in the case of fiber synthesis. On the other hand, the value of  $k$  was 172 ppm/hr for the stick-in-bundle precipitates, which was much lower than that of fibrous precipitates.

The flake shape precipitate, however, showed an abnormal trend of concentration variation against aging time. The residual  $[Ce]$  seemed to be independent of the aging time. Fig. 4.1(b) shows that the as-prepared samples for ICP-AES analysis were entirely turbid. When the suspension was removed from the 90°C water bath, the turbid disappeared and the solution returned to transparent. The remained precipitate from the turbid showed flake-shape morphology. Therefore, the solubility of the particles in the suspension was the cause of turbidity change. As a result, the re-dissolving of the particles in the suspension during the room-temperature filtration procedure of the sample is a reasonable explanation for the abnormal trend of  $[Ce]$  concentration shown

in Fig. 4.7.

The morphology of sample 1 varied with aging period is shown in Fig. 4.8. Two kinds of morphologies were observed during the synthesis, including spherical particles and fibers. The plot of aspect ratio of the grown precipitates against aging time is shown in Fig. 4.9. After 10 hr aging, the aspect ratio of fibers dramatically increased from 1 to 110, and reached stable state. This turn point of 10 hr aging was also the linear decreasing region of [Ce] showing in Fig. 4.7. After 10 hr aging, [Ce] consumed to nearly empty and reached stable value.

Recalling Fig. 4.1(a), the starting solution turned to turbid first, and then deposited to sediment. In concentrated case of 0.10 m<sub>c</sub> of cerium ions, the first two steps completed in couple hr. The following two steps would complete in less than 8 hr. The whole precipitate procedure completed in less than 10 hr.

The morphology of sediment showing in Figs. 4.8(a), 4.8(b), and 4.8(c) was spherical particles, which could only be observed when the aging time was less than 10 hr. After that, only fibrous precipitate was observed. Loose agglomeration started to form after the formation of sediment. The fibrous morphology of the precipitates indicated the co-existence of the porous particles and fibers before 10 hr aging. Therefore, in the step 3 of Fig. 4.1(a), the colloidal particles re-dissolved and the fibers

formed at the same time until the colloidal particles disappeared entirely.

Water solubility of various hydrates on the particles in suspension led to the deviation of ICP-AES result. The re-dissolving of the colloidal particle also resulted in different morphology observation of the precipitate. As shown in Fig. 4.10, it is noted that the morphology of the spherical colloidal particles to be very porous due to the re-dissolving when the particles were treated in D.I. water. The porous morphologies are preserved by dilution of the solution with pure ethanol. The SEM micrographs shown in Figs. 4.8(a) to 4.8(c) are different from those shown in Fig. 4.10.

### 4.1.3 Morphology Evolution by Thermal Treatment

Fig. 4.11 shows the XRD patterns of pure,  $Gd^{3+}$ -doped and  $Sm^{3+}$ -doped cerium hydrocarbonate fibers. These patterns indicated the similar crystalline phases ( $Ce(CO_3)_3$ ,  $Ce(OH)_3$  and residual citric acid phases) of the hydrocarbonate fibers were identified. However, there were still several other peaks that could not be identified. These peaks might be contributed by the other hydrated Ce-species.

In the following sections, only GDC fibers were chosen for test. Fig. 4.12 shows that the hydrocarbonate fibers transforms to oxide if calcined higher than  $300^\circ C$ . In Fig. 4.12, there is an endothermic peak at  $150-200^\circ C$ , and an obvious exothermic peak above

250°C. Two peaks agree with the two stages of mass loss during the thermal treatment in DTG results. The first endothermic peak corresponds to the loss of physical water. The second peak is the transformation of hydrocarbonate to oxide, resulting in an extremely strong exothermic reaction (burning) between 250°C and 350°C. It indicates that the combustion of the hydrocarbonate fibers occurs in the temperature range. Therefore, the thermal treatment of the hydrocarbonate fibers should be carefully controlled, either by very slow ramping rate, or holding at temperature less than 250°C before reaching the maximal exothermic temperature so to avoid rapid combustion.

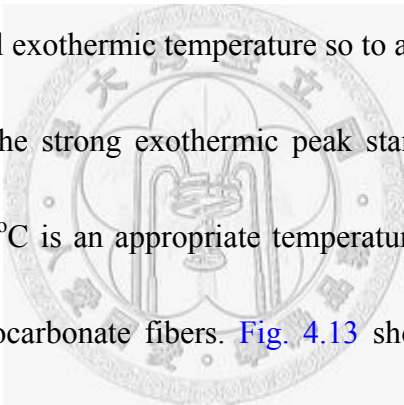


[Fig. 4.12](#) shows that the strong exothermic peak starts at 220°C. Therefore, the holding temperature of 220°C is an appropriate temperature that allows to completing the decomposition of hydrocarbonate fibers. [Fig. 4.13](#) shows the results of DTA/TG analysis with an isothermal treatment at 220°C or 200°C for 1 hr. [Fig.4.13\(a\)](#), however, shows a temperature surge during the isothermal period of 220°C. An associated mass drop could also be observed from [Fig. 4.13\(a\)](#). This result reveals that the reaction produces heat from the decomposition of carbonate species able to heat-up the test material. The reaction of these fibers was accelerated as temperature increased, similar to a chain reaction. As a result, the combustion occurred, and the carbon-contained compounds were decomposed. In [Fig. 4.13\(b\)](#), the exothermic peak was not observed

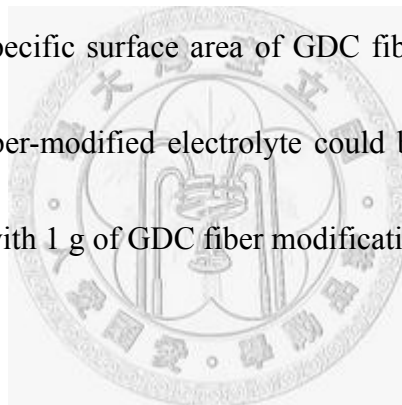
during the isothermal procedure at 200°C. A continuous mass loss during the isothermal treatment indicated that continuous decomposition of hydrocarbonate fibers proceeded. Therefore, the holding temperature at 200°C was confirmed to be appropriate for the purpose from Fig. 4.13(b). It was noted that the decomposition of hydrocarbonate fibers was not completed in 1 hr from Fig. 4.13(b). An exothermic reaction was still observed at 240°C. The phenomenon reveals that a longer period of fiber decomposition by a thermal treatment at 200°C is necessary to avoid combustion.

Fig. 4.14 shows XRD patterns of GDC fibers thermal-treated at several temperatures. It shows that, the decomposition of hydrocarbonate fibers completed after 200°C calcinations and the fibers with amorphous phase were observed. The crystallization of CeO<sub>2</sub> phase could be observed starting at 300°C. It can be seen from Fig. 4.14 that there are no other phases remained after calcination. According to Scherrer formula, Eq. (3-3), the crystalline size of GDC fibers was growing from 3 nm to 16 nm when thermal treated temperature increased from 300°C to 600°C.

Fig. 4.15 shows the bright field (BF) and centered dark field (CDF) TEM microstructures of GDC fibers thermal treated at 600°C. Fig. 4.15(a) shows a diffraction pattern (ring pattern) indicating that the GDC fibers are polycrystalline with a cubic ceria structure (JCPD file [34-0394]), and no other phases remained. The average grain

size of GDC is 15 nm which is measured from the CDF image. After 1200°C thermal treatment, the grain of GDC grew to 150 nm from the SEM and TEM microstructures in Figs. 4.16(a) and 4.16(b). The grain growth of GDC fibers against thermal treatment temperature was shown in Fig. 4.17.

In the very first time that the fiber was synthesized, the fiber exhibited serious agglomeration, as shown in Fig. 4.16(c). The agglomerated fibers which were thermally treated at 1200°C (Fig. 4.16(d)) led to a lost of the surface area of GDC fiber. Through B.E.T. measurement, the specific surface area of GDC fiber was 0.71 m<sup>2</sup>/g. It implies that, the surface area of fiber-modified electrolyte could be at least 7000 times larger than the naked electrolyte with 1 g of GDC fiber modification.



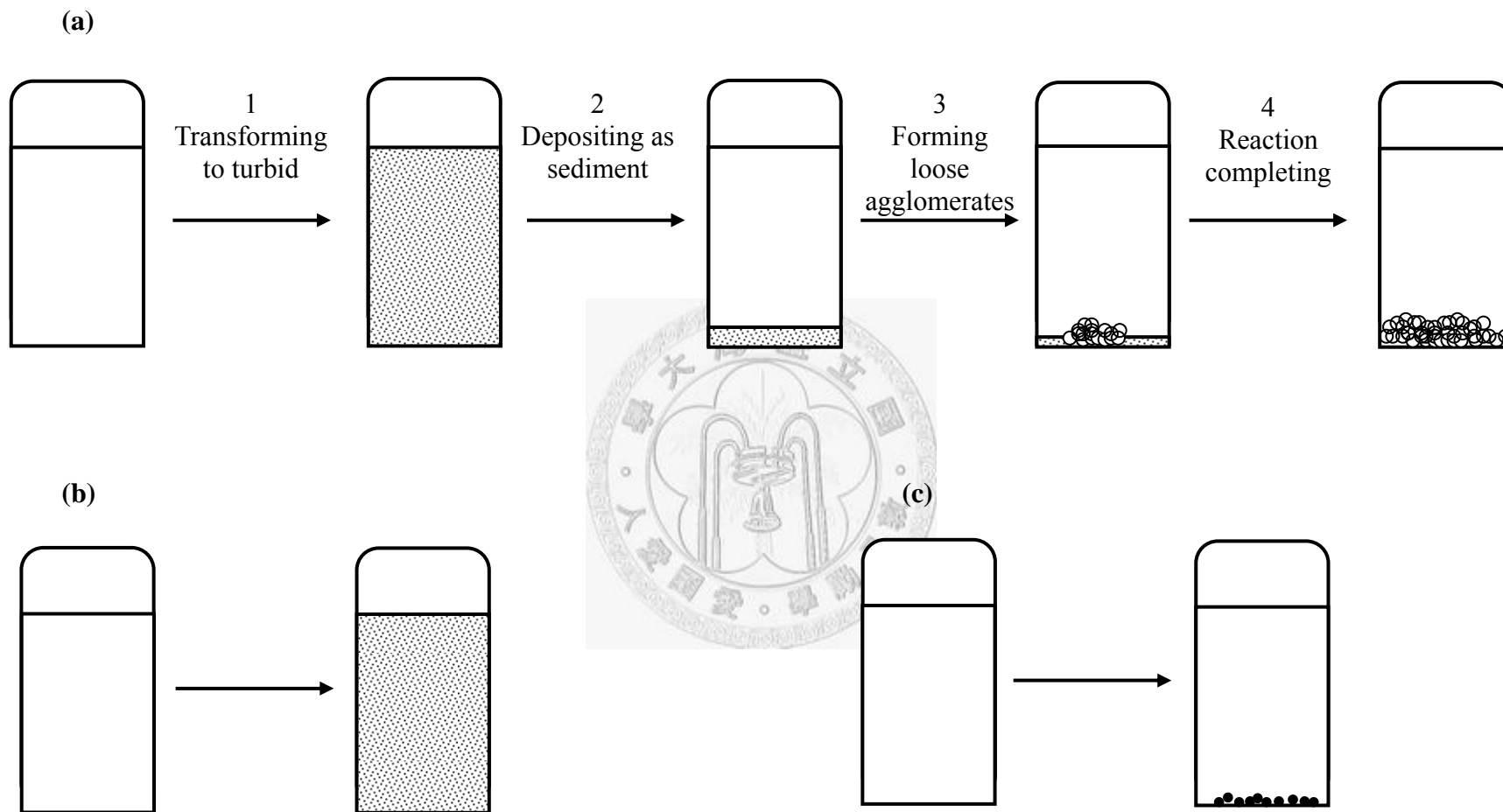
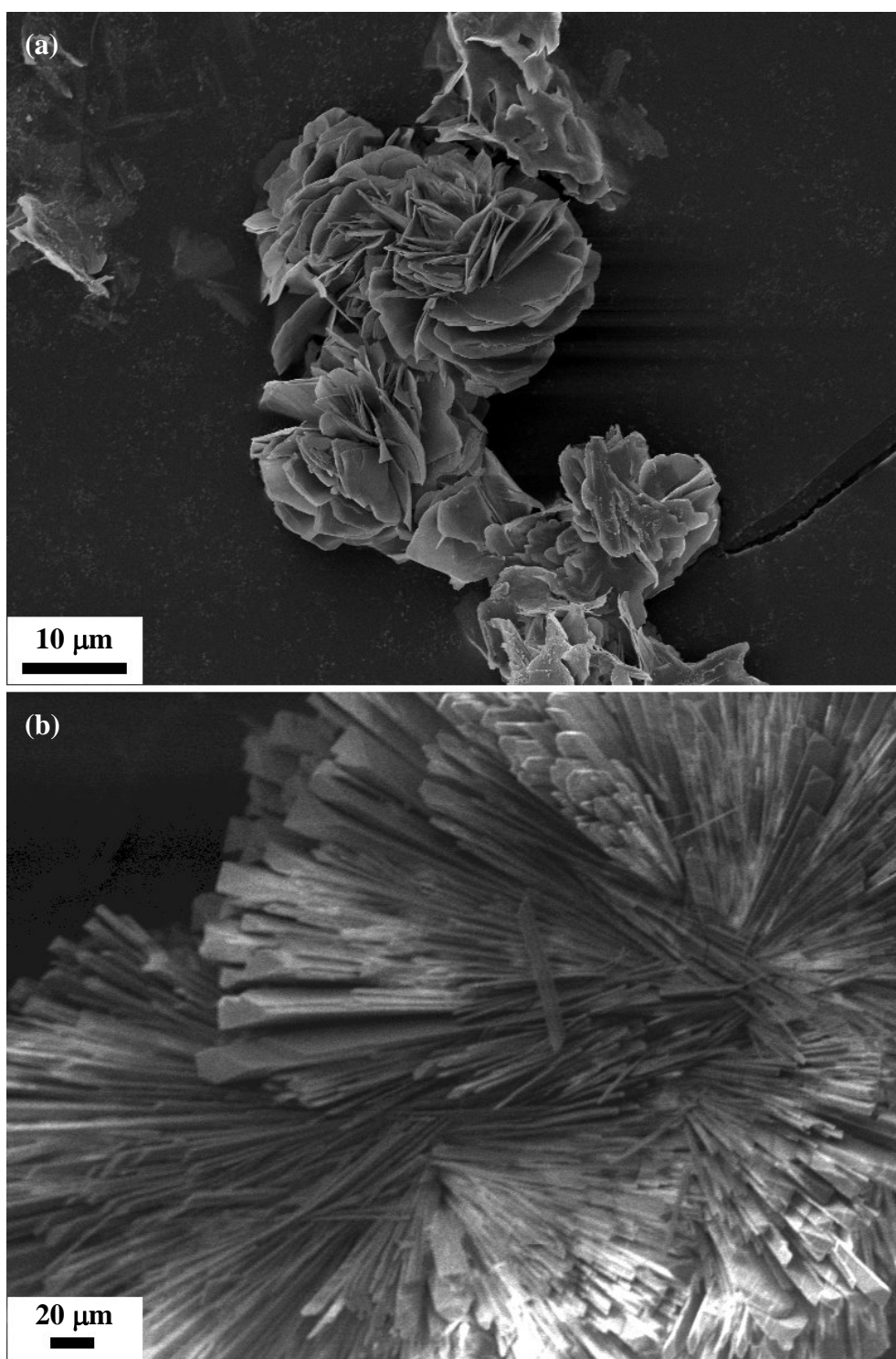


Fig. 4.1 Schematic diagram showing the change of reacting solution growing (a) fibrous, (b) flake-shape, and (c) stick-in-bundle precipitates.





**Fig. 4.2** As-prepared cerium hydrocarbonate precipitates with the  $[\text{NaOH}]/[\text{C}_6\text{H}_8\text{O}_7]$  ratio equal to (a) 0.8, in a flake shape, (b) 0.2, in a shape of stick-in-bundle. The solutions were aged at  $90^\circ\text{C}$  for 24 hr.



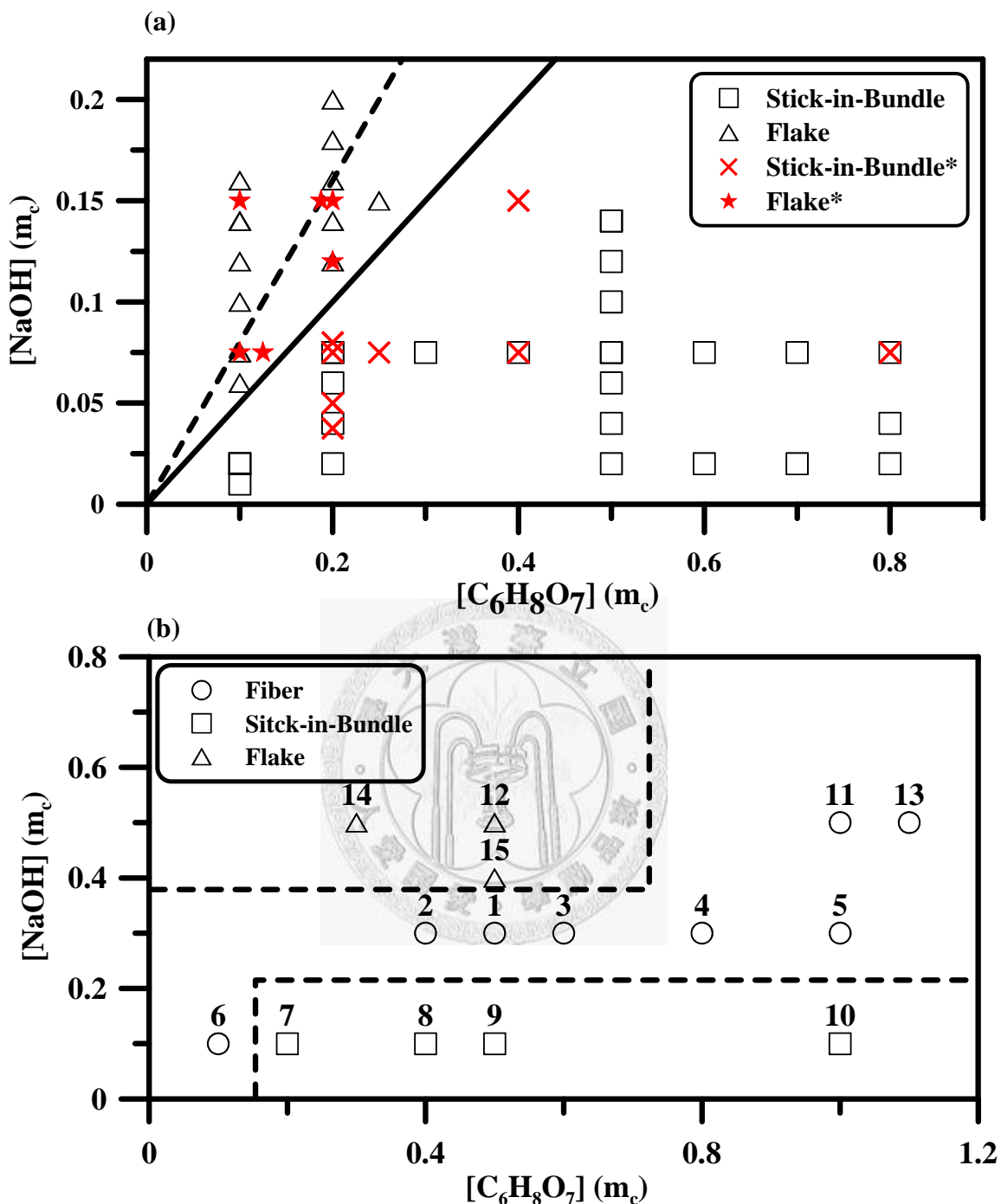
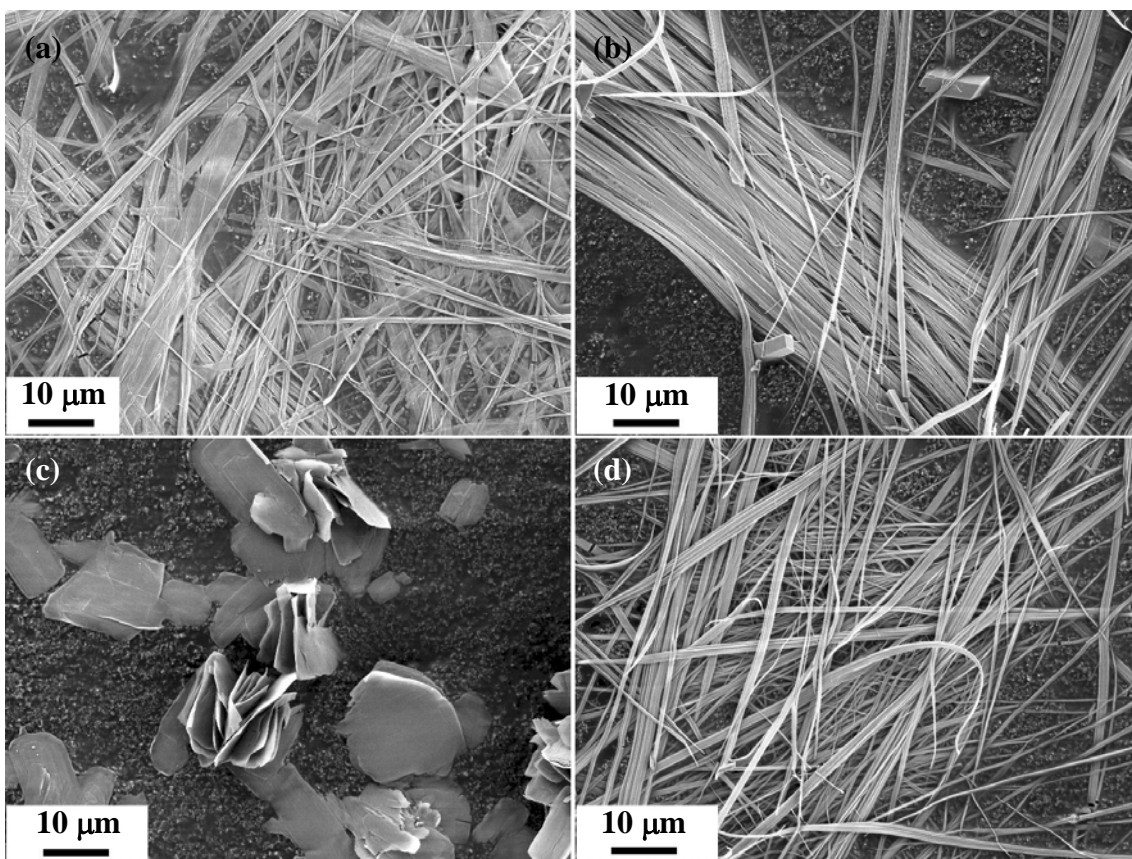


Fig. 4.3 Concentration of  $[\text{NaOH}]$  and  $[\text{C}_6\text{H}_8\text{O}_7]$  illustrating the resulted morphologies of cerium hydrocarbonate precipitates aged at  $90^\circ\text{C}$  for 24 hr. The starting concentration of cerium ion was (a) 0.025 m and (b) 0.1 m. In (a), the solid and dash lines represent the ratio of 0.5 and 0.8, respectively. The symbols with “\*” were previous results reported by Sung [Sung *et al.*, 2007].



**Fig. 4.4** As-prepared cerium hydrocarbonate fibrous precipitates with a  $[\text{NaOH}]/[\text{C}_6\text{H}_8\text{O}_7]$  ratio of 0.6 (sample 1) aging for (a) 12 hr and (b) 60 hr, respectively, and ratio of 0.8 (sample 15) aging for (c) 24 hr and (d) 62 hr, respectively.



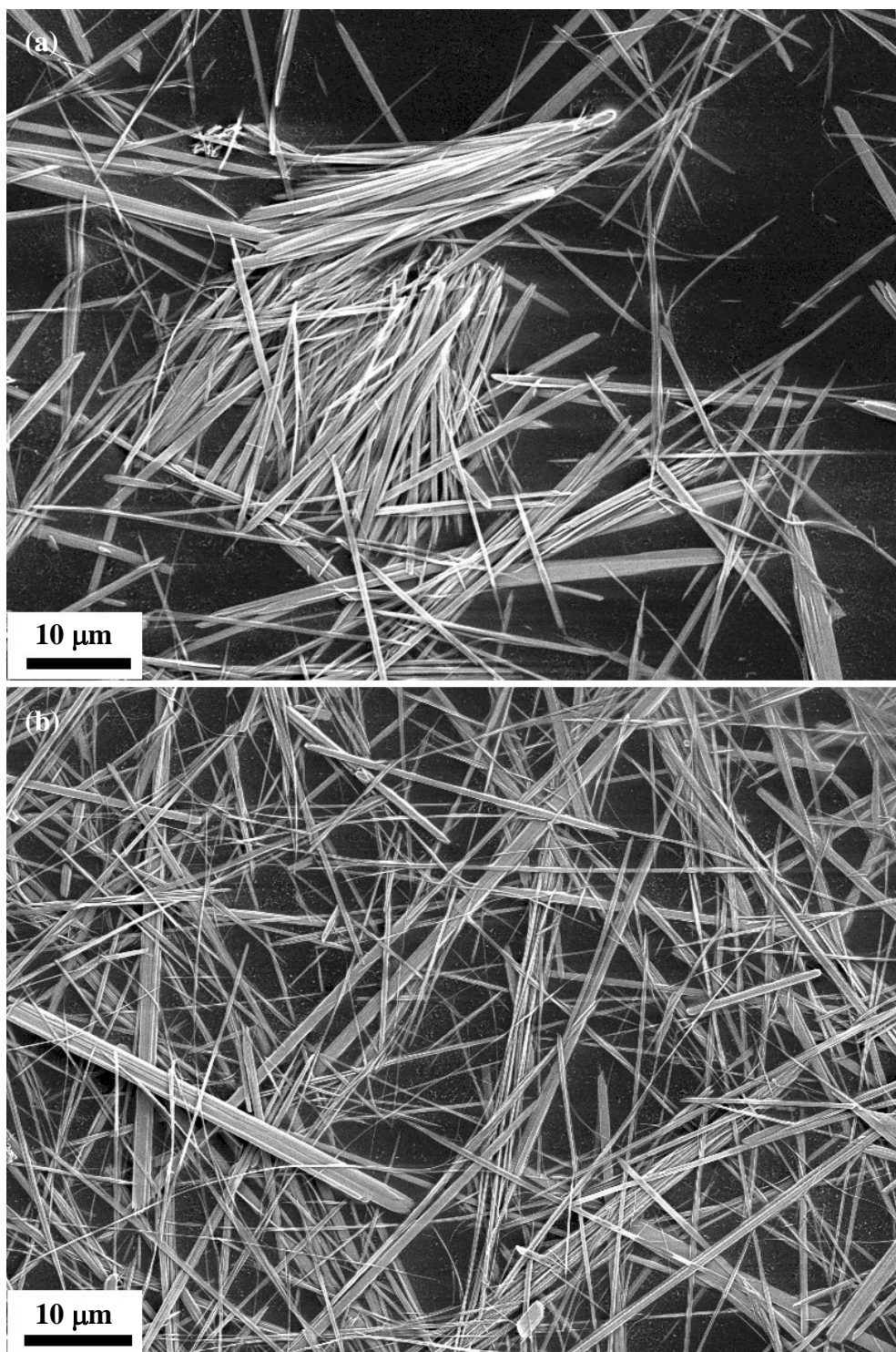


Fig. 4.5 SEM micrographs showing the fibrous microstructures of 20 mol% (a)  $\text{Gd}^{3+}$  doped and (b)  $\text{Sm}^{3+}$  doped cerium hydrocarbonate fibers.

**Table 4.1** ICP quantitative results of Gd and Sm doped cerium hydrocarbonate fibers and correspondent formulation of GDC and SDC

	Ce (ppm)	Gd (ppm)	Sm (ppm)
GDC	6.07	1.43	N/A
SDC	6.18	N/A	1.26
GDC	$\text{Ce}_{0.83}\text{Gd}_{0.17}\text{O}_{1.915}$		
SDC	$\text{Ce}_{0.84}\text{Sm}_{0.16}\text{O}_{1.925}$		

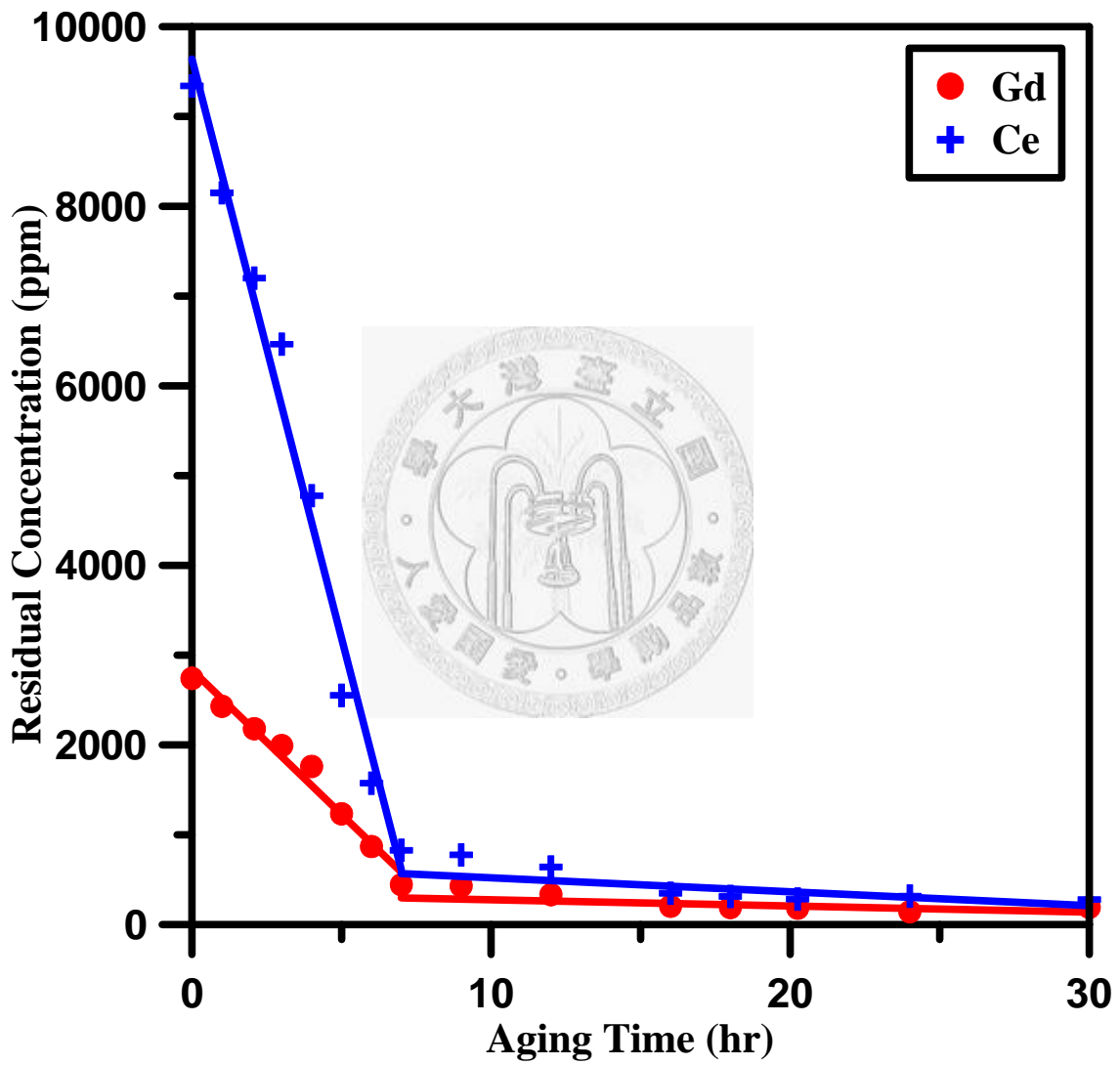


Fig. 4.6 Residual concentrations of Ce<sup>3+</sup> and Gd<sup>3+</sup> ions during aging period by ICP.

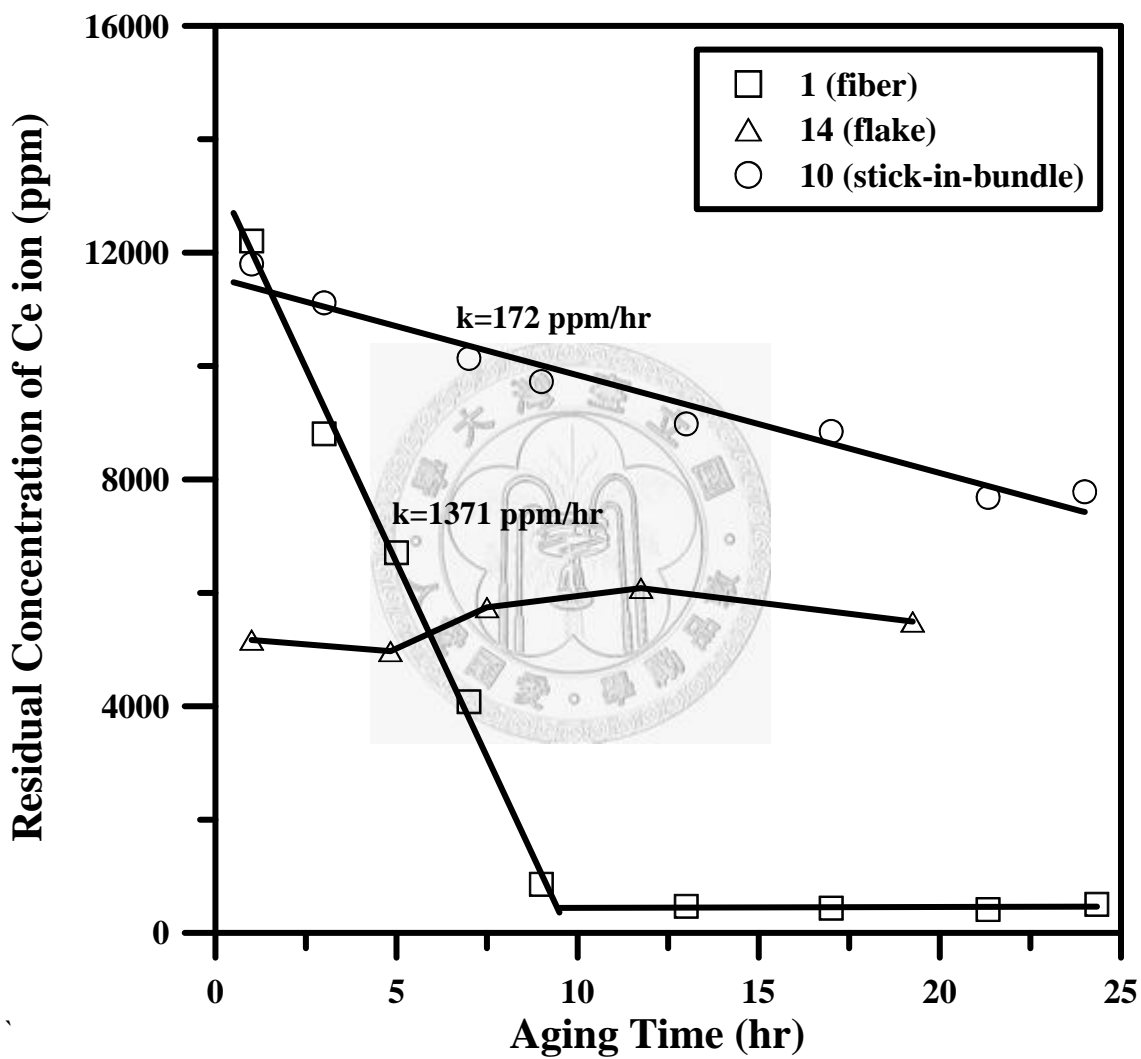
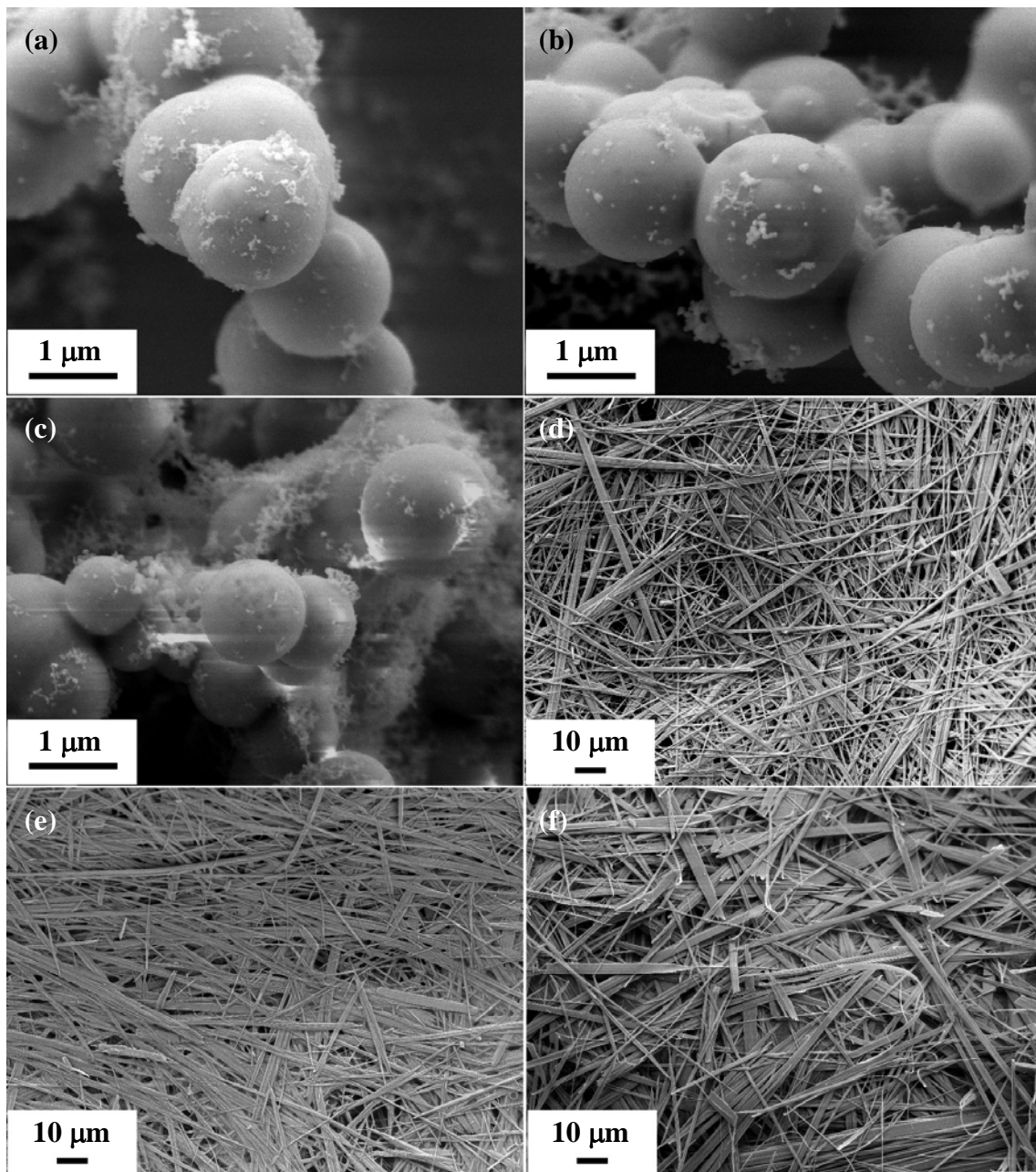


Fig. 4.7 Residual concentrations of Ce<sup>3+</sup> ions of fibrous, flake, and stick-in-bundle precipitates synthesis during aging period by ICP. The labeled numbers represent the sample numbers in Fig. 4.3.





**Fig. 4.8** SEM micrographs of Gd doped cerium hydrocarbonate precipitate with (a) 2 hr, (b) 5 hr, (c) 7 hr 20 min, (d) 10 hr, (e) 12 hr, and (f) 24 hr aging period.

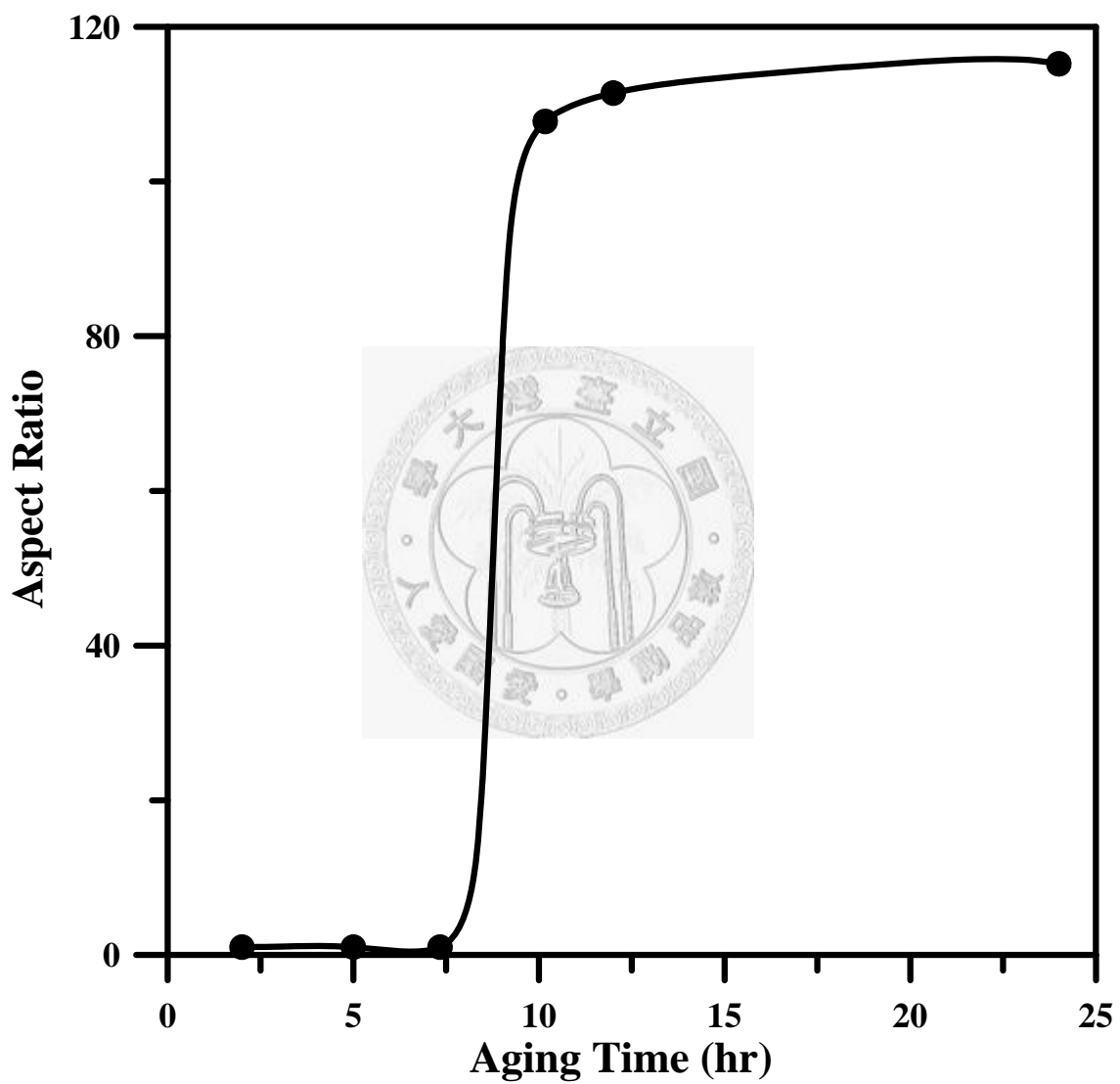
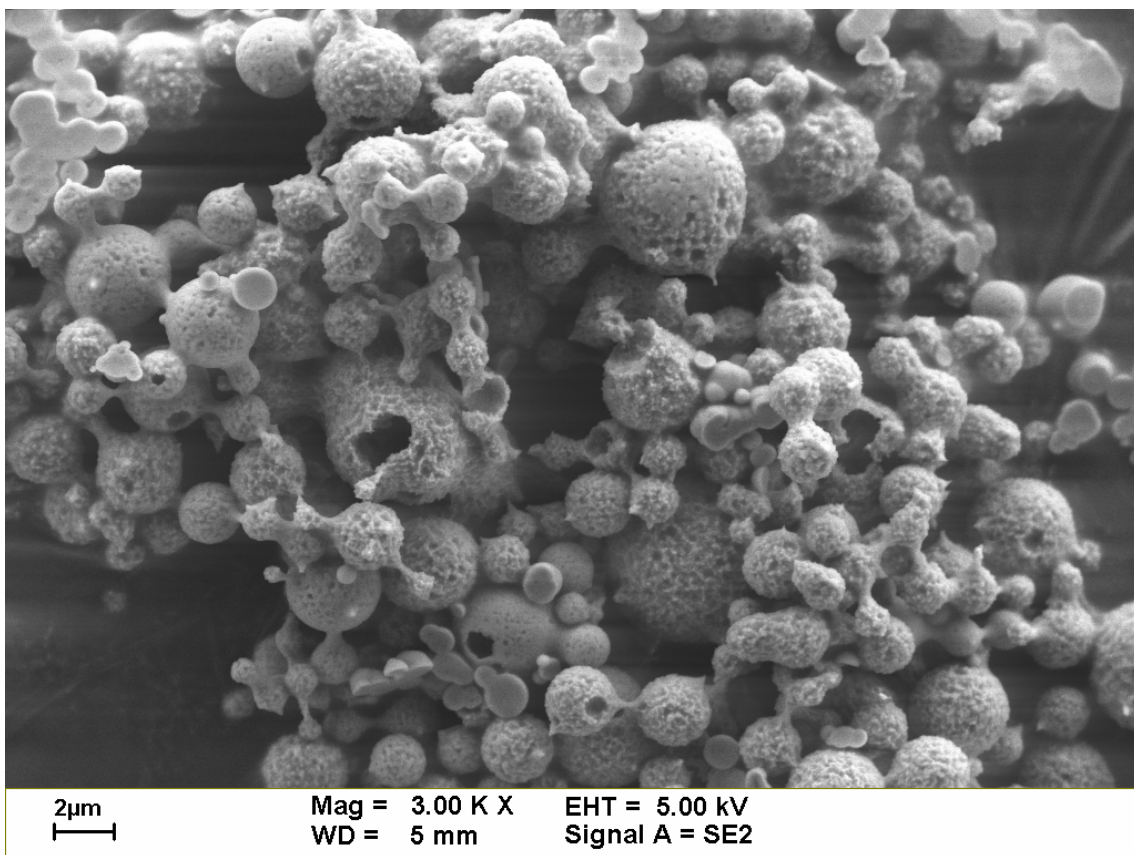


Fig. 4.9 Aspect ratio variation of Gd doped cerium hydrocarbonate precipitation (sample 1 in Table 3.2) against aging time.





**Fig. 4.10** SEM microstructure of Gd doped cerium hydrocarbonate precipitate with 1 hr aging period, in which the specimen was sampled in D.I. water.

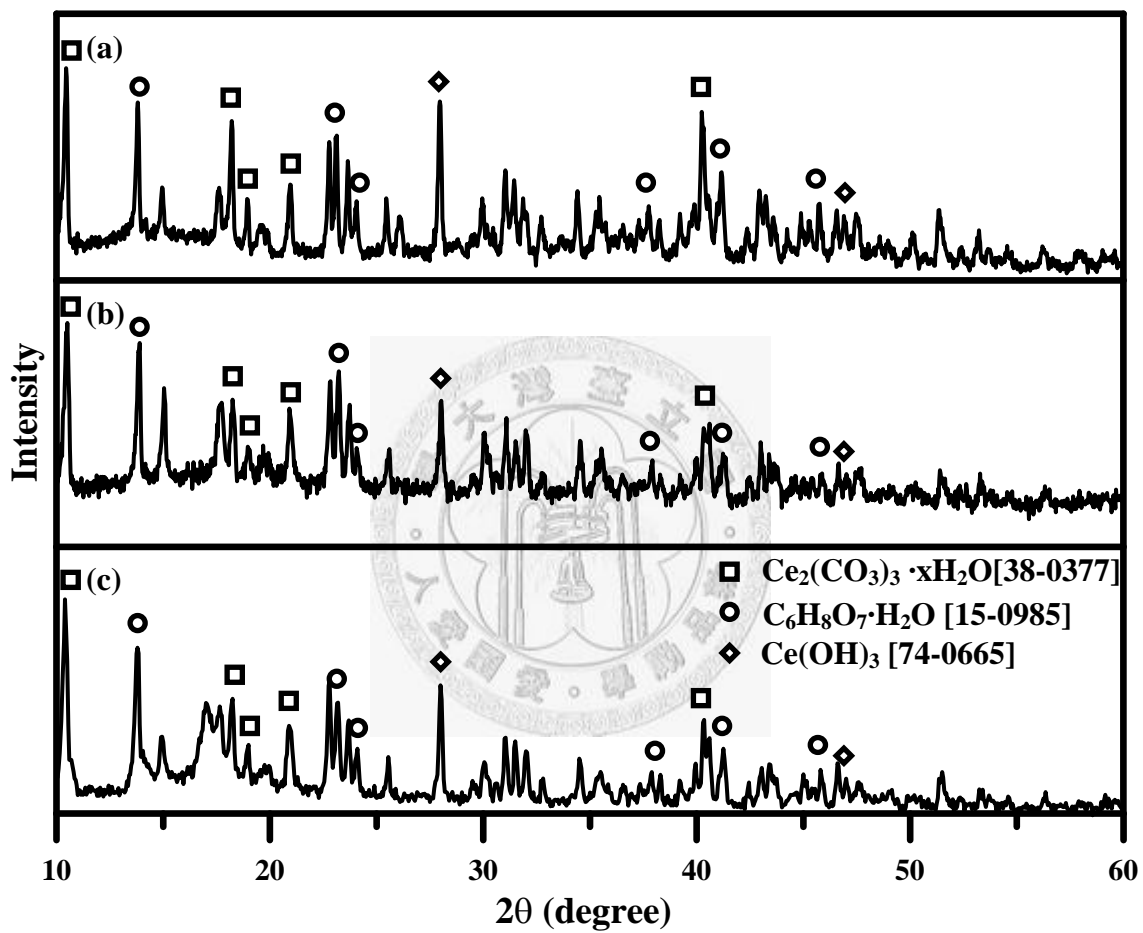


Fig. 4.11 XRD patterns of as-prepared (a) pure cerium, (b) gadolinium doped, and (c) samarium doped hydrocarbonate fibers.

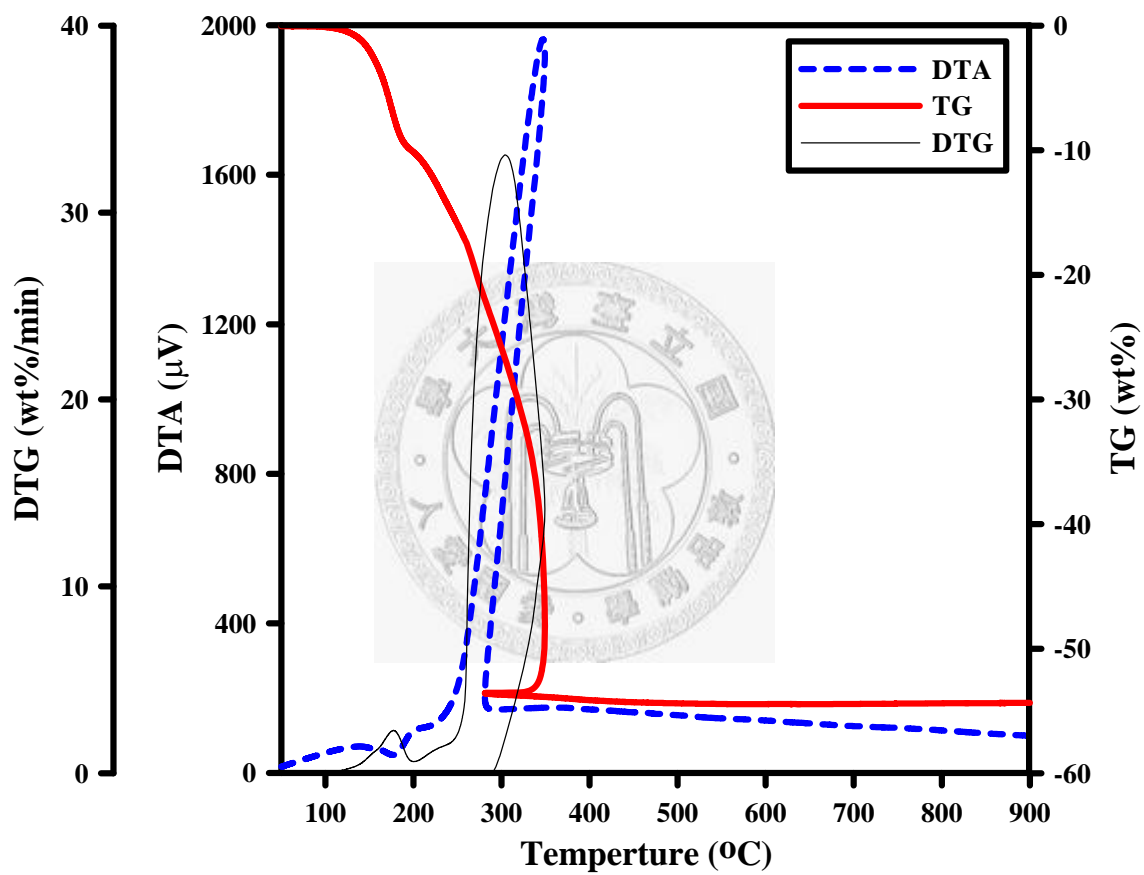


Fig. 4.12 DTA/TG analysis results of GDC fibers with a ramp rate of 10°C/min.

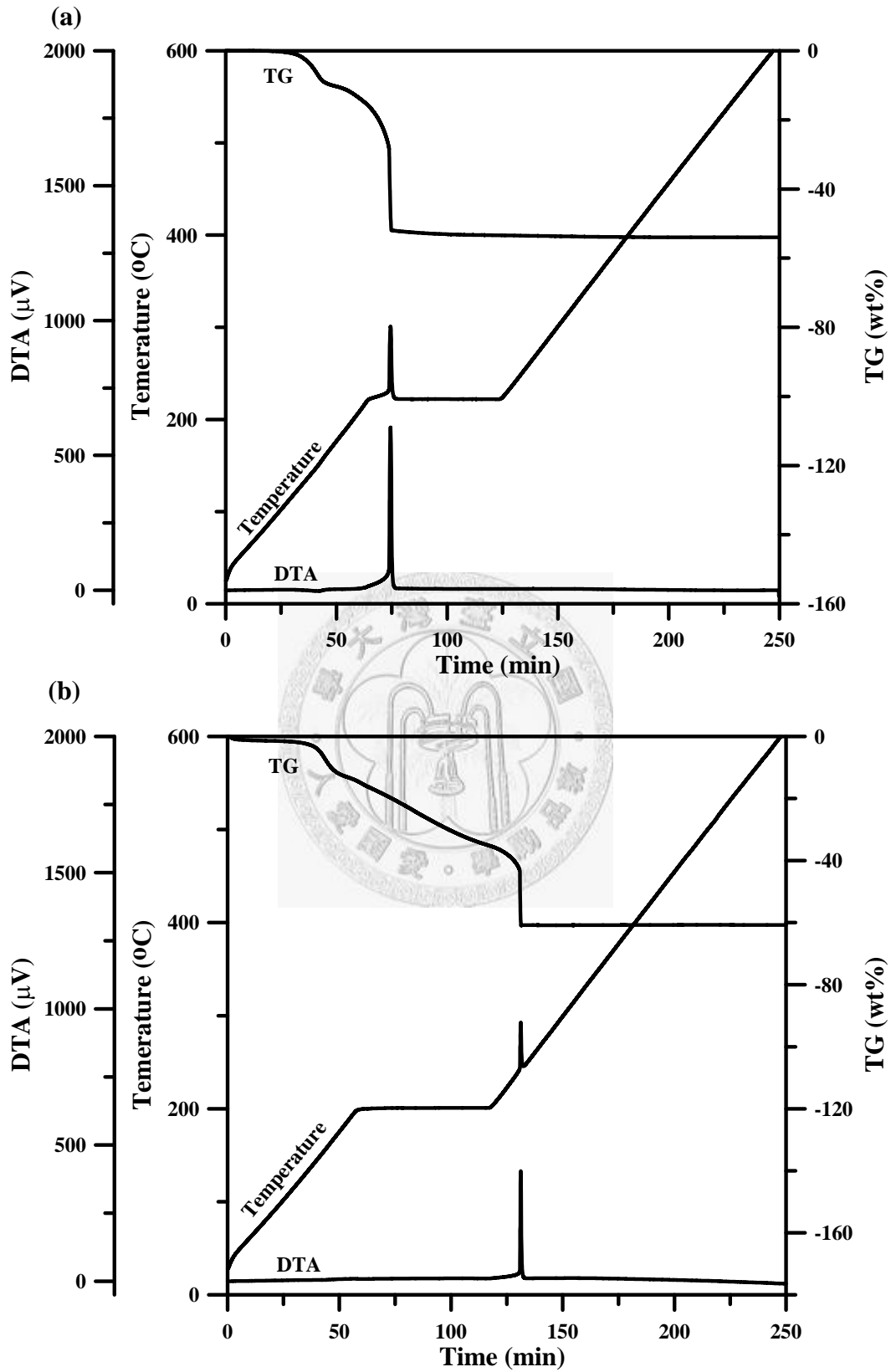


Fig. 4.13 DTA/TG analysis results of GDC fibers with a ramp rate of  $3^{\circ}\text{C}/\text{min}$  to (a)  $220^{\circ}\text{C}$  and (b)  $200^{\circ}\text{C}$ , then holding for 1 hr.

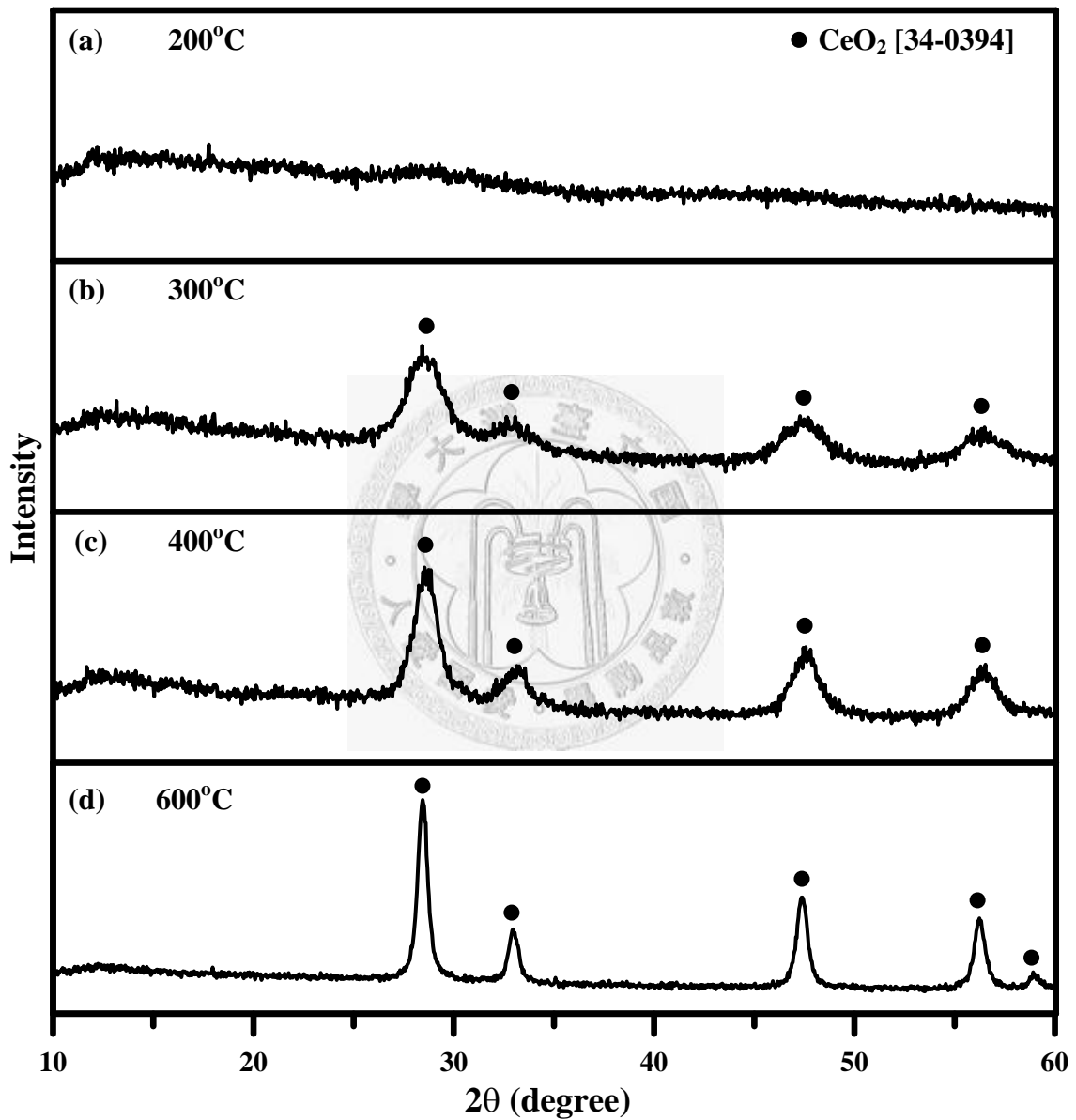


Fig. 4.14 XRD patterns of GDC fibers thermal treated at (a) 200°C, (b) 300°C, (c) 400°C, and (d) 600°C for 1 hr.

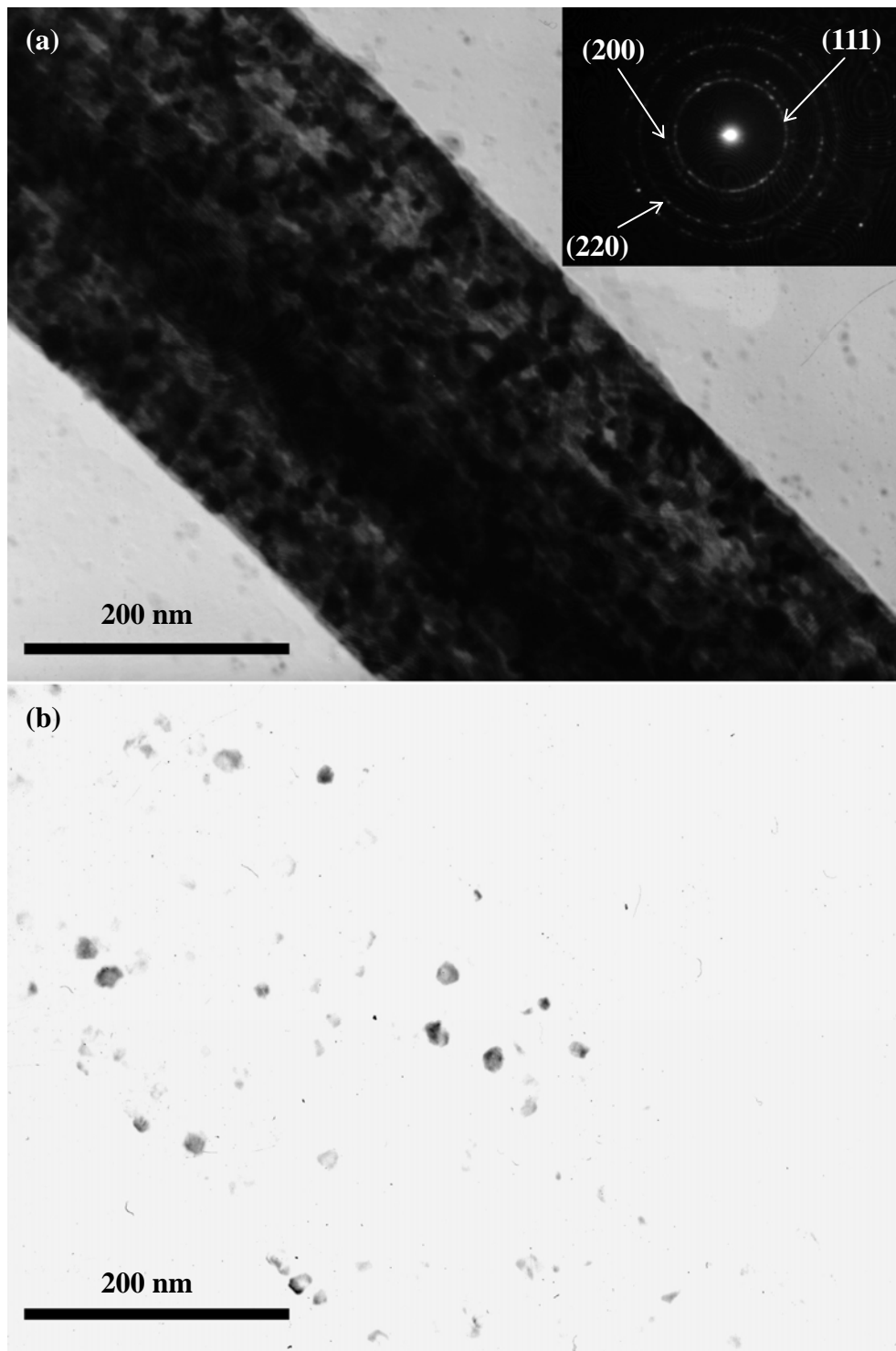
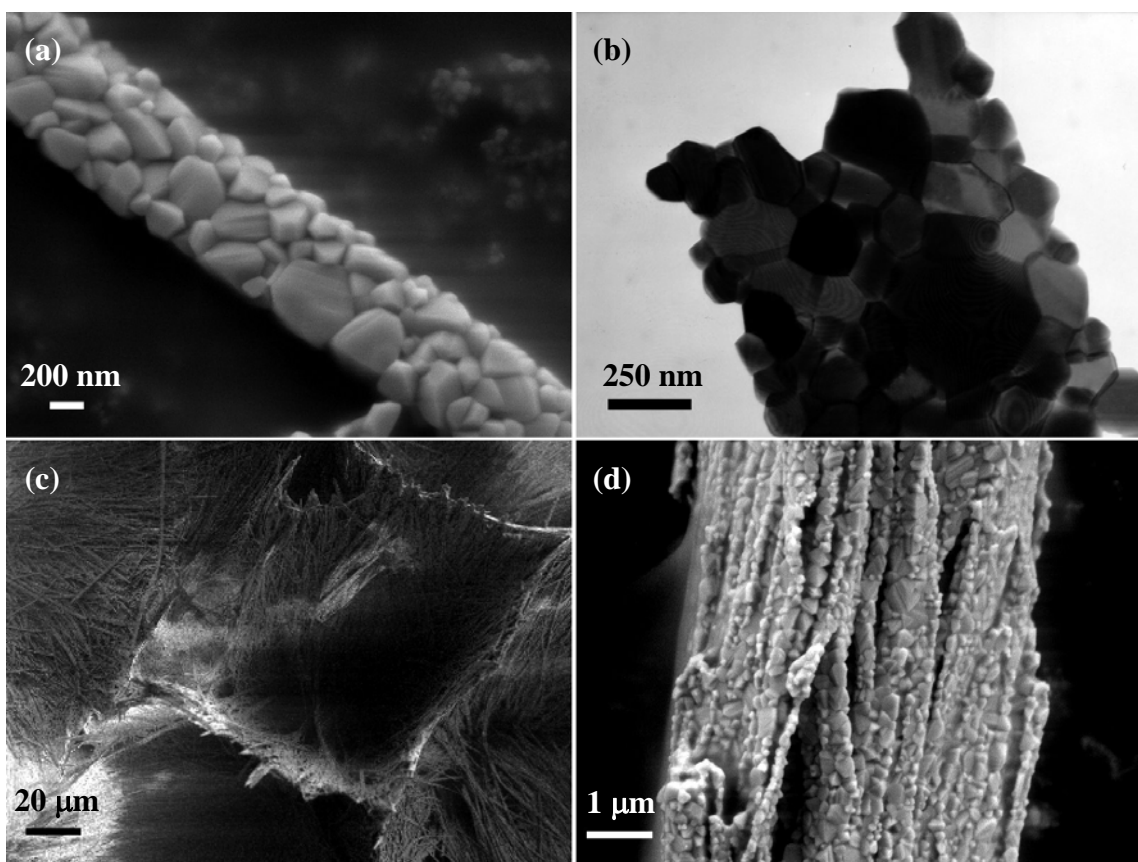


Fig. 4.15 (a) BF image and (b) negative CDF image of GDC fibers thermal treated at 600°C for 1 hr.



**Fig. 4.16** SEM images of 1200°C thermally treated GDC (a) single fiber and (b) TEM bright field image revealing polycrystalline character, (c) SEM image of as-prepared GDC hydrocarbonate fibers with some agglomeration, and (d) fibrous morphologies in bundle.

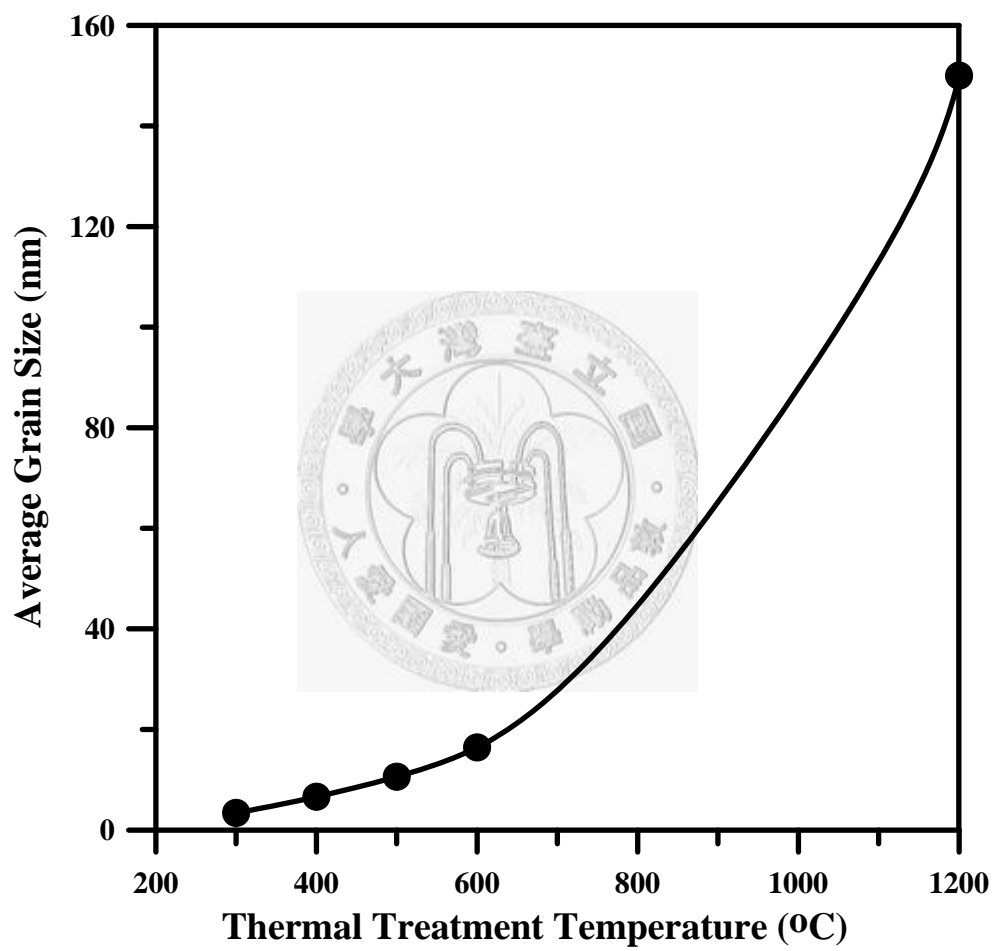


Fig. 4.17 Average grain size of GDC fiber plotted against thermal treatment temperature.



## 4.2 Properties of LSM Powders

This section reports several properties of LSM powders synthesized either with Pechini method or a sol-gel process with PAA. Their properties, including their crystallization, chemical composition uniformity, and electrical properties of LSM/YSZ interface will be compared with a commercial product made by H. C. Starck, Germany.

### 4.2.1 Phase Formation of LSM

[Fig. 4.18](#) shows the DTA/TG results of LSM powders synthesized by Pechini method (P-LSM). The DTA/TG curve profile of P-LSM was similar with the results from Gaudon's report [\[Gaudon \*et al.\*, 2002\]](#). There were three main exothermic peaks, found at 135°C, 260°C, and 380°C, respectively. Besides, the associated mass losses were observed in TG result. According to the interpretation on the mass spectra reported by Gaudon, all the exothermic reactions were related to the decompositions of carbon and nitrogen contained compounds. In addition, the maximal exothermic peak at 380°C associated with the obvious consumption oxygen indicated the occurrence of combustion. The final mass loss after 500°C was due to the production of CO<sub>2</sub> gas.

The XRD patterns of P-LSM powders thermal-treated at different temperatures are shown in [Fig. 4.19](#). It is noted that the as-prepared P-LSM powders were not amorphous

phase, in fact, might be the crystals of polymerized EG. After 400°C calcination, which was higher than the maximal exothermic peak in Fig. 4.18, the decomposition of C-N compounds resulted in amorphous state. From Fig. 4.19, a carbon contained phase of  $\text{La}_2\text{CO}_5$  was formed after 500°C calcination. This undesirable phase could only be detected in the P-LSM powder that was thermal-treated at 500°C and 600°C. The crystallization of LSM started at 600°C calcination, by which the  $\text{La}_2\text{CO}_5$  phase co-existed with the LSM phase. After 700°C thermal treatment, pure LSM phase could be obtained without any  $\text{La}_2\text{CO}_5$  phase. The TG result indicated that the mass loss was completed at thermal treated temperature  $\geq 700^\circ\text{C}$ . This TG result agreed to the XRD result.

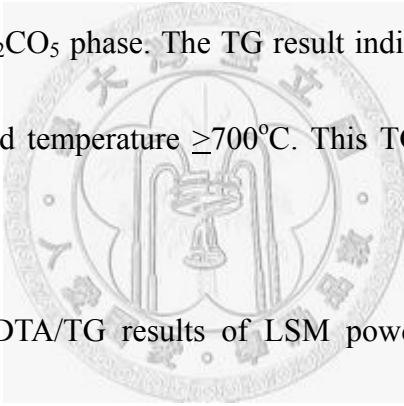
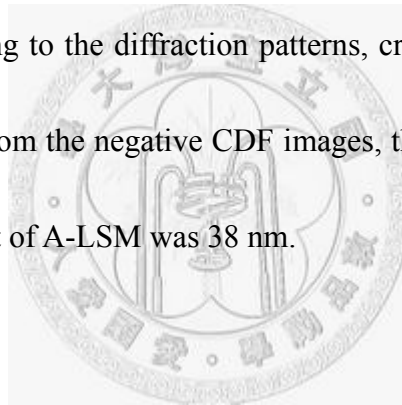


Fig. 4.20 shows the DTA/TG results of LSM powders synthesized by sol-gel method with PAA (A-LSM). From Hsu's report<sup>[Hsu, 2003]</sup>, pure LSM phase could be synthesized with the ratio of PAA and LSM higher than 2. Therefore, the ratio of 2 was used in this study. In Fig. 4.20, the endothermic peak at temperature lower than 100°C was the vaporization of adsorbed water. During the thermal treatment of A-LSM, a lot of gas with brown color emitted after the temperatures greater than 230°C. From the DTA result, there was a broad exothermic peak between 230°C and 320°C. The formation of  $\text{NO}_2$  was associated with the exothermic reaction.

Fig. 4.21 shows the XRD patterns of A-LSM powders thermal treated at different temperatures. Comparing with the XRD results of P-LSM powders, the crystallization of LSM phase occurred at 600°C calcination. In addition, there was no other phases could be detected at all calcination temperatures. The TG result, however, indicated that the mass loss completed after the thermal treatment at temperatures higher than 750°C, which was 50°C higher than that of P-LSM.

Fig. 4.22 shows TEM micrographs of P-LSM and A-LSM powders thermal treated at 800°C for 1 hr. According to the diffraction patterns, crystalline LSM phase of both powders was confirmed. From the negative CDF images, the average crystalline size of P-LSM was 27 nm, and that of A-LSM was 38 nm.



#### 4.2.2 Quantitative Analysis of Composition

Table 4.2 shows the quantitative EDS results of P-LSM and A-LSM powders by SEM-EDS. The samples and standard LSM powders were uni-axially die-pressed at 100 MPa pressure and thermal treated at 900°C for 1 hr. The chemical composition of LSM powders and its distribution were analyzed by Student statistics<sup>[Harris, 2001]</sup>. Student's t-distribution is a statistical method to express the confidence interval (CI) of the experimental results. The CI of true population mean value ( $\mu$ ) is expressed as

$$\mu = \bar{x} \pm \frac{ts}{\sqrt{n}} \quad (4-3)$$

where  $\bar{x}$  is the mean value of measured data,  $s$  is measured standard deviation,  $n$  is the number of measurements, and  $t$  is Student's  $t$ , which is taken from  $t$ -table according to degree of freedom ( $n-1$ ) and used CI. As the increase of the  $n$  (for instance,  $>30$ ),  $\bar{x}$  and  $s$  are approaching to the true average value and true standard deviation ( $\sigma$ ). In this study, the CI of 95% was used. The chemical distribution of commercial LSM (expressed as H-LSM) was also analyzed by  $t$ -distribution. In the CI of 95%, the results indicated a very narrow distribution of each composition (25.0%±0.2% for  $\text{La}_2\text{O}_3$ , 12.2%±0.2% for  $\text{SrO}$ , and 62.8%±0.3% for  $\text{MnO}_x$ ). The quantitative analysis results of P-LSM and A-LSM are shown in [Table 4.2](#), indicated the deviation (in %) of three oxides was narrower (a better composition) distribution of the P-LSM powder.

True chemical composition of the P-LSM was  $(\text{La}_{0.79}\text{Sr}_{0.21})\text{MnO}_3$ . The A-LSM was  $(\text{La}_{0.76}\text{Sr}_{0.24})\text{MnO}_3$ . The true composition was close to the original one,  $(\text{La}_{0.8}\text{Sr}_{0.2})\text{MnO}_3$ . P-LSM, however, still showed the smaller composition deviation from the original one. Therefore, comparing the composition made by Pechini method with that of sol-gel method, Pechini method could serve a better chemical accuracy and precision in practice.

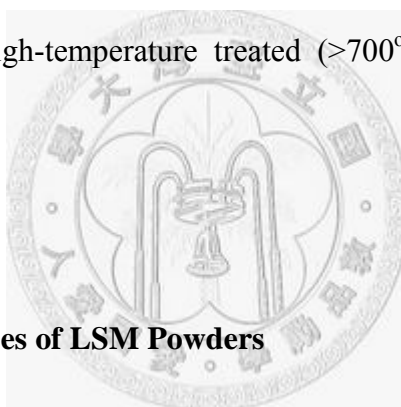
### 4.2.3 Reduction of Surface Area

In general, the sol-gel process could give a narrower composition distribution, smaller particle size, and larger surface area of ceramic powders comparing with the powder by solid state reaction. Table 4.3 and Fig. 4.23 show the specific surface area of P-LSM and A-LSM powders thermal treated at different temperatures. The surface area of both LSM powders decreased with the increase of thermal treatment temperature. Before the 700°C treatment, the surface area of P-LSM powder was larger than that of A-LSM. After 700°C treatment, however, A-LSM showed smaller specific surface area. In the TEM microstructures shown in Fig. 4.22, it is noted that the crystalline size distribution of P-LSM was broader than that of A-LSM. The hard agglomeration of grains induced the abnormal grain growth. Therefore, since the grain growth occurred, the grains inside the hard agglomeration would grow easier than the others, and led to the loss of surface area.

In Hsu's report<sup>[Hsu, 2003]</sup>, the addition of PAA could result in smaller grain size and larger specific surface area due to the steric hindrance from PAA. The surface area of LSM increased from 5.6 to 25.2 m<sup>2</sup>/g if the ratio of PAA/LSM increased from 0 to 10. In Pechini method, the chelator was citric acid, which was a smaller molecule comparing with PAA. The chelating model is shown in the report by Abreu Jr.<sup>[Abreu Jr. et al.,</sup>

<sup>2005]</sup>. Weaker steric hindrance might result in agglomeration of LSM in the stage after the resin formation, and further lead to larger agglomeration.

Besides, the as-prepared P-LSM has a higher specific surface area, which implies the particles is in smaller size and higher driving force to grow as thermally treated at higher temperature. Without the growth limitation (for instance, residual carbon), the particle size increases dramatically as the surface diffusion is apparent. As the opposite case, A-LSM has more carbon residual, resulting in grain growth inhibition. The specific surface area of high-temperature treated ( $>700^{\circ}\text{C}$ ) of A-LSM was slightly greater than the other case.



#### 4.2.4 Electrical Properties of LSM Powders

In the application of SOFC, the ohmic polarization from electrolyte had been reduced by decreasing the thickness of electrolyte<sup>[Chen *et al.*, 2006]</sup> or using the alternative material, such as doped ceria<sup>[Zhang *et al.*, 2007]</sup>. As a result, the polarization contributed from electrodes becomes an important issue that determines the performance of SOFC<sup>[Chen *et al.*, 2007]</sup>. Therefore, the electrical property of the interface between LSM and YSZ was analyzed in this section.

The synthesized and commercial LSM (H. C. Starck) powders were coated on

sintered YSZ electrolyte by spray-coating and thermal treated at 1200°C for 1 hr before measurement. The detail thermal treatment procedures of every LSM powders are shown in Fig. 3.5.

Fig. 4.24 shows the fracture surfaces of the interfaces between LSM and YSZ thermal treated at 1200°C. After thermal treatment, the thickness of LSM thin films was 6 μm for all the synthesized LSM layers. The microstructure of the fracture surface of P-LSM porous layer is also shown in Fig. 4.25. The thickness of the porous layer from H-LSM is shown in Fig. 4.24(c), which is only 3 μm. In addition, the porosity of two synthesized LSM thin films was obviously greater than H-LSM thin layer from the SEM microstructures. To calculate the length density ( $L_A$ ) of TPB between LSM and YSZ, Saltykov equation<sup>[Harrigan *et al.*, 1984]</sup> is introduced,

$$L_A = \frac{\pi}{2} P_L = \frac{\pi}{2} N_L \quad (4-4)$$

where  $L_A$  is length per unit area,  $P_L$  is contact points per unit length, and  $N_L$  is the number of objects or interceptions per unit length. The TPB zone is counted based on the corner effects of conducting flux of LSM materials in contact with YSZ<sup>[Yu *et al.*, 2004]</sup>.

The results of the measured TPB are shown in Table 4.4. It can be seen that the synthesized LSM films showed similar  $L_A$  of TPB, around 1.5 μm/μm<sup>2</sup>. H-LSM film showed 30% higher  $L_A$  of TPB (2 μm/μm<sup>2</sup>) than synthesized LSM powders, implying

the possibility of a lower activation polarization for H-LSM powder.

The residual carbon content was also analyzed to identify the effect on electrical conductivity. The carbon contents of all the LSM powders are listed in [Table 4.5](#). The residual carbon content of A-LSM powders was much greater than P-LSM powders after 900°C thermal treatment. With carefully thermal treatment control, the residual carbon content in P-LSM powders could be reduced to half (from 470 ppm to 212 ppm). A-LSM powders, however, the thermal treatment of slow heating didn't result in an obvious reduction of residual carbon content.

The interface resistance between LSM and YSZ was measured by 3-terminal electrical measurement. The electrodes and attachment configurations had been mentioned in [Section 3.5.8](#). In practice, the voltage signal needed a few min to reach stable since the constant current was inputted. One example is shown in [Fig. 4.26\(a\)](#). Therefore, to get the stable voltage signal, the voltage value was obtained from the average of the voltage signal from 200 s to 400 s. As the increase of the input current, the measured voltage increased, as shown in [Fig. 4.26\(b\)](#). The interface resistance was calculated from the slope in the linear region of I-V curve.

The area of working electrode was kept at 0.38 cm<sup>2</sup> in this study. [Table 4.6](#) lists the interfacial ASR of the specimens of P-LSM, P-LSM-S, A-LSM, A-LSM-S, and H-LSM



layers. The Arrhenius plot is shown in Fig. 4.27. The resistance from LSM film itself was neglected in this study. According to Hsu's research<sup>[Hsu, 2003]</sup>, the electrical conductivity of LSM thin film with PAA/LSM = 2 was 2.1 S/cm at 1000°C. In other word, the ASR of the LSM thin film with 6 μm in thickness was only 0.3 mΩ, which could be ignored if comparing with the interfacial resistance of a few Ω in this study. For all the LSM layers, the ASR decreased as the increasing of testing temperature from ~10 kΩ at 300°C down to ~5 Ω at 800°C. From the ASR results, there was no apparent difference in all the LSM layers. The reasons for the similar electrical properties can be several folds. Similar chemical composition, close residual carbon content in the LSM films and porous microstructures are considered.

In order to offer the appropriate interface strength between LSM grains and YSZ electrolyte plate, the thermally treated temperature must be higher than 1200°C, as shown in Fig. 4.28. The P-LSM-S film thermally treated at 1100°C was easily removed from YSZ plate by external physical force.

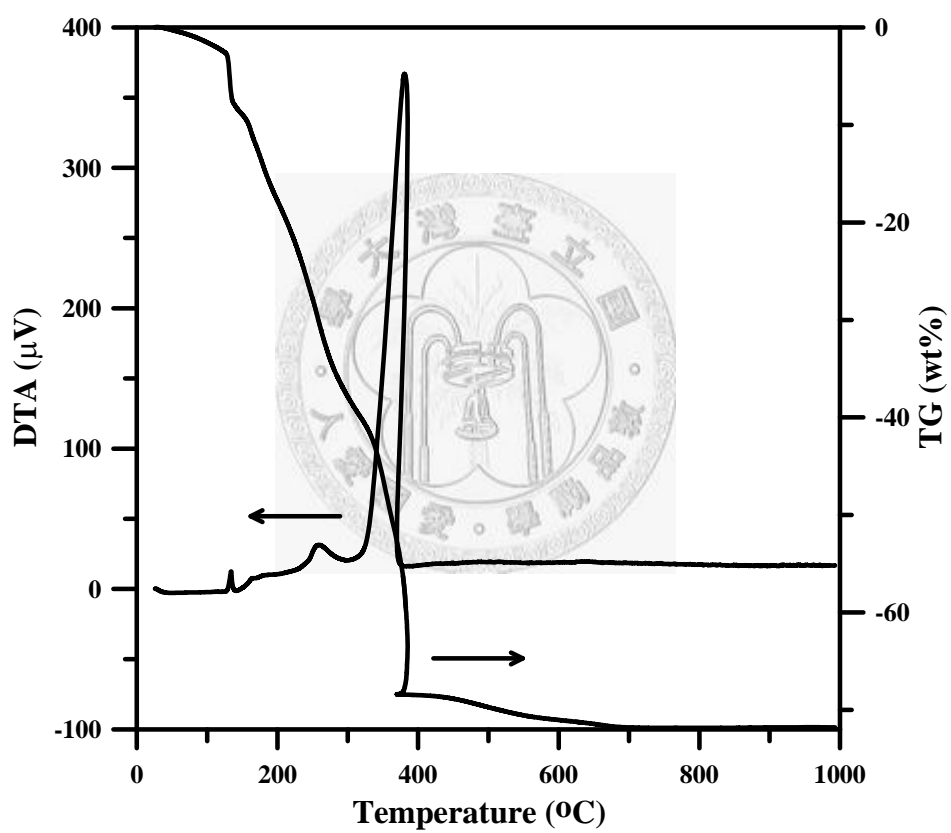


Fig. 4.18 DTA/TG results of P-LSM powders. The temperature ramp rate was 10°C/min.

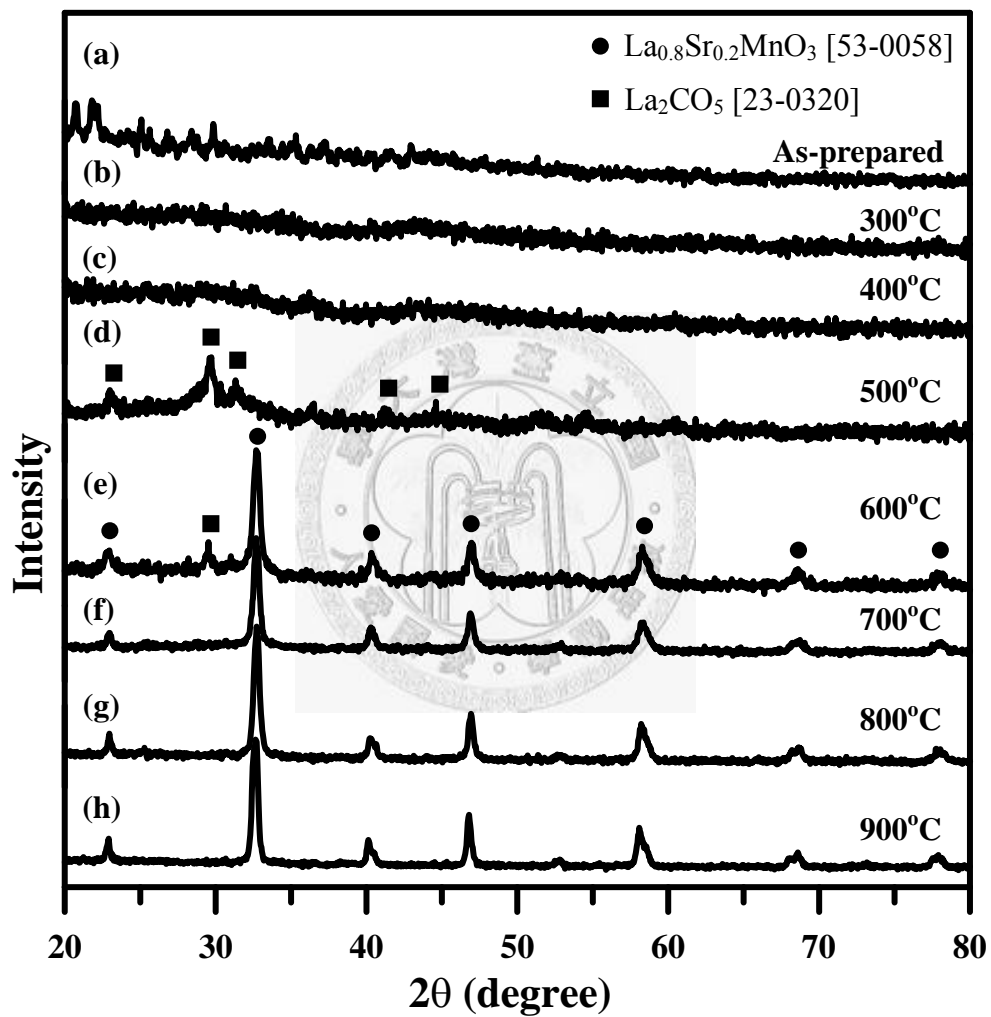


Fig.4.19 XRD patterns of P-LSM powders (a) as-prepared, and by different thermal treatment at the temperature of (b) 300°C, (c) 400°C, (d) 500°C, (e) 600°C, (f) 700°C, (g) 800°C, and (h) 900°C.

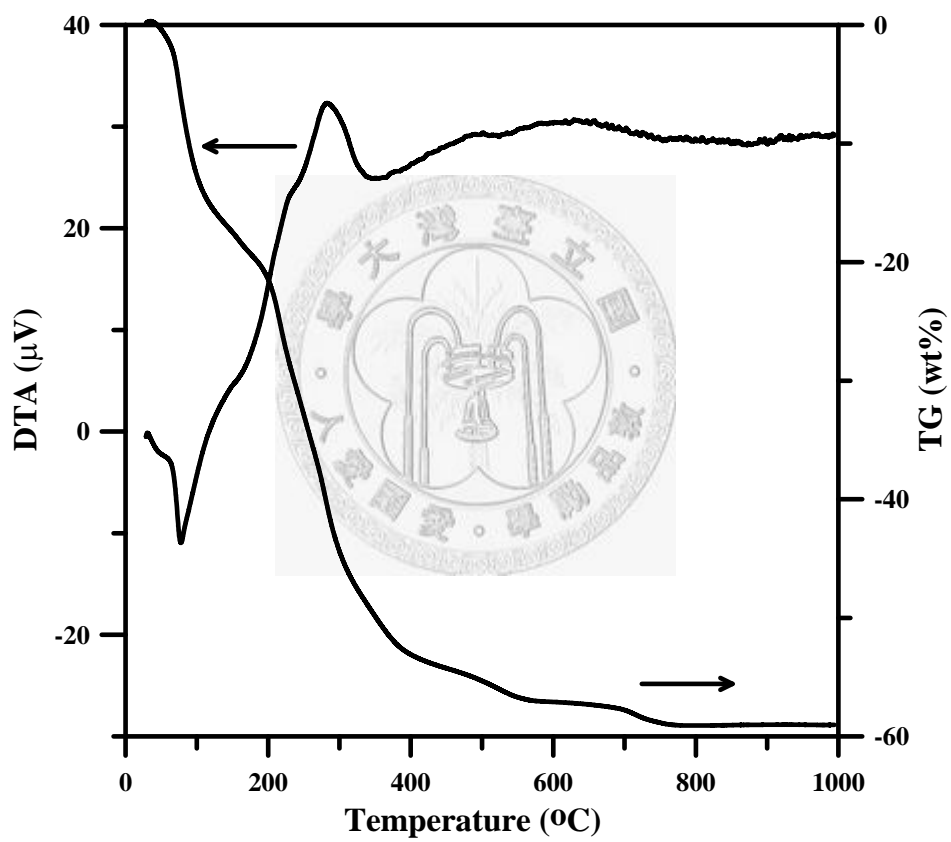


Fig. 4.20 DTA/TG results of A-LSM powder. The temperature ramp rate was 10°C/min.

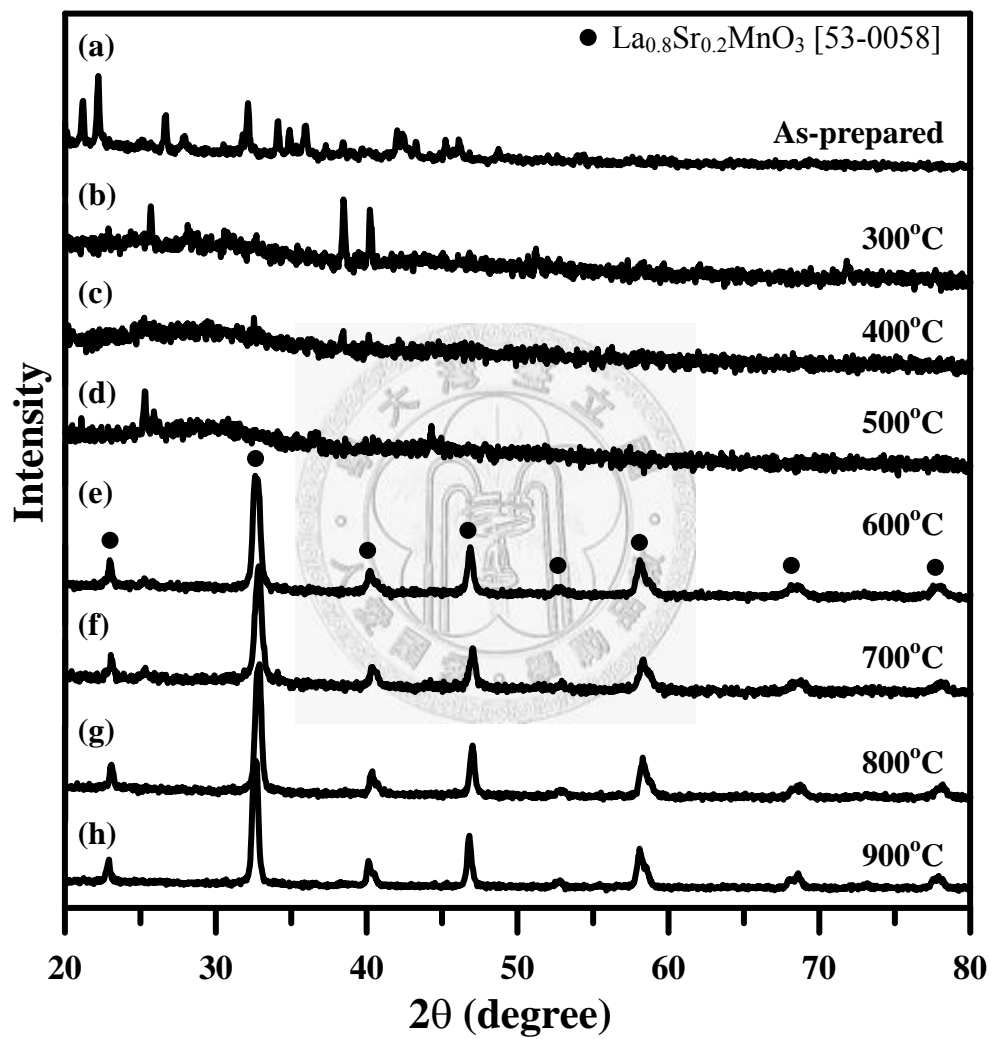
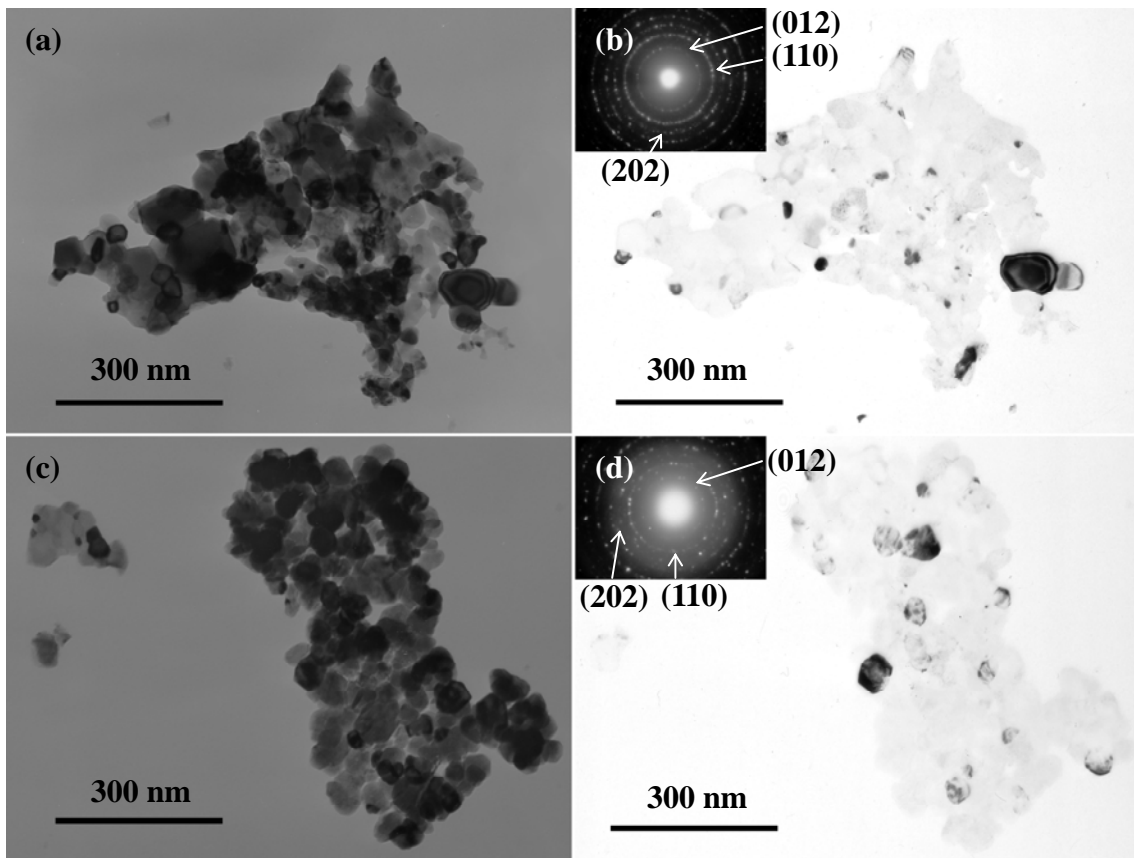


Fig.4.21 XRD patterns of A-LSM powders (a) as-prepared, and by different thermal treatment at temperature of, (b) 300°C, (c) 400°C, (d) 500°C, (e) 600°C, (f) 700°C, (g) 800°C, and (h) 900°C.



**Fig. 4.22** TEM micrographs showing (a) BF and (b) negative CDF of 800°C thermal treated P-LSM powders, and (c) BF and (d) negative CDF of A-LSM 800°C thermal treated powders.

**Table 4.2** Quantitative analysis of P-LSM and A-LSM

P-LSM				A-LSM			
	mol%				mol%		
Compound	La <sub>2</sub> O <sub>3</sub>	SrO	MnO <sub>x</sub>	Compound	La <sub>2</sub> O <sub>3</sub>	SrO	MnO <sub>x</sub>
values (%)	24.7	12.1	63.2	values (%)	28.3	10.4	61.4
	24.8	13.4	61.9		22.9	15.6	61.5
	25.3	11.7	63.0		24.9	11.0	64.1
	24.6	13.6	61.8		21.5	17.9	60.6
	25.6	11.2	63.2		24.5	14.8	60.7
	26.0	11.6	62.4		22.6	18.0	59.4
	25.7	12.4	61.9		23.9	14.7	61.4
	24.3	13.93	61.8		22.9	17.3	59.8
	23.3	15.4	61.3		23.8	15.4	61.0
	22.4	15.4	62.3		24.2	12.7	63.1
	25.6	12.3	62.1		23.4	15.8	60.8
	24.5	14.4	61.1		24.7	14.7	60.6
mean	24.7	13.13	62.2	mean	23.97	14.83	61.2
STD	1.05	1.46	0.69	STD	1.66	2.45	1.29

95% Confidence Interval (CI)	La <sub>2</sub> O <sub>3</sub>	SrO	MnO <sub>x</sub>
P-LSM	24.7%±0.5%	13.1%±0.8%	62.2%±0.3%
A-LSM	22.0%±0.9%	14.8%±1.3%	61.2%±0.7%

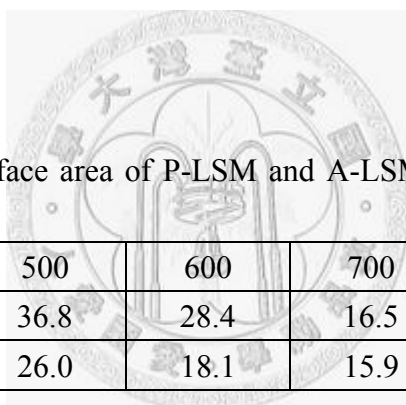


**Table 4.3** BET specific surface area of P-LSM and A-LSM thermal treated at various temperatures

	T (°C)	500	600	700	800	900
BET (m <sup>2</sup> /g)	P-LSM	36.8	28.4	16.5	4.34	1.37
	A-LSM	26.0	18.1	15.9	12.8	4.05



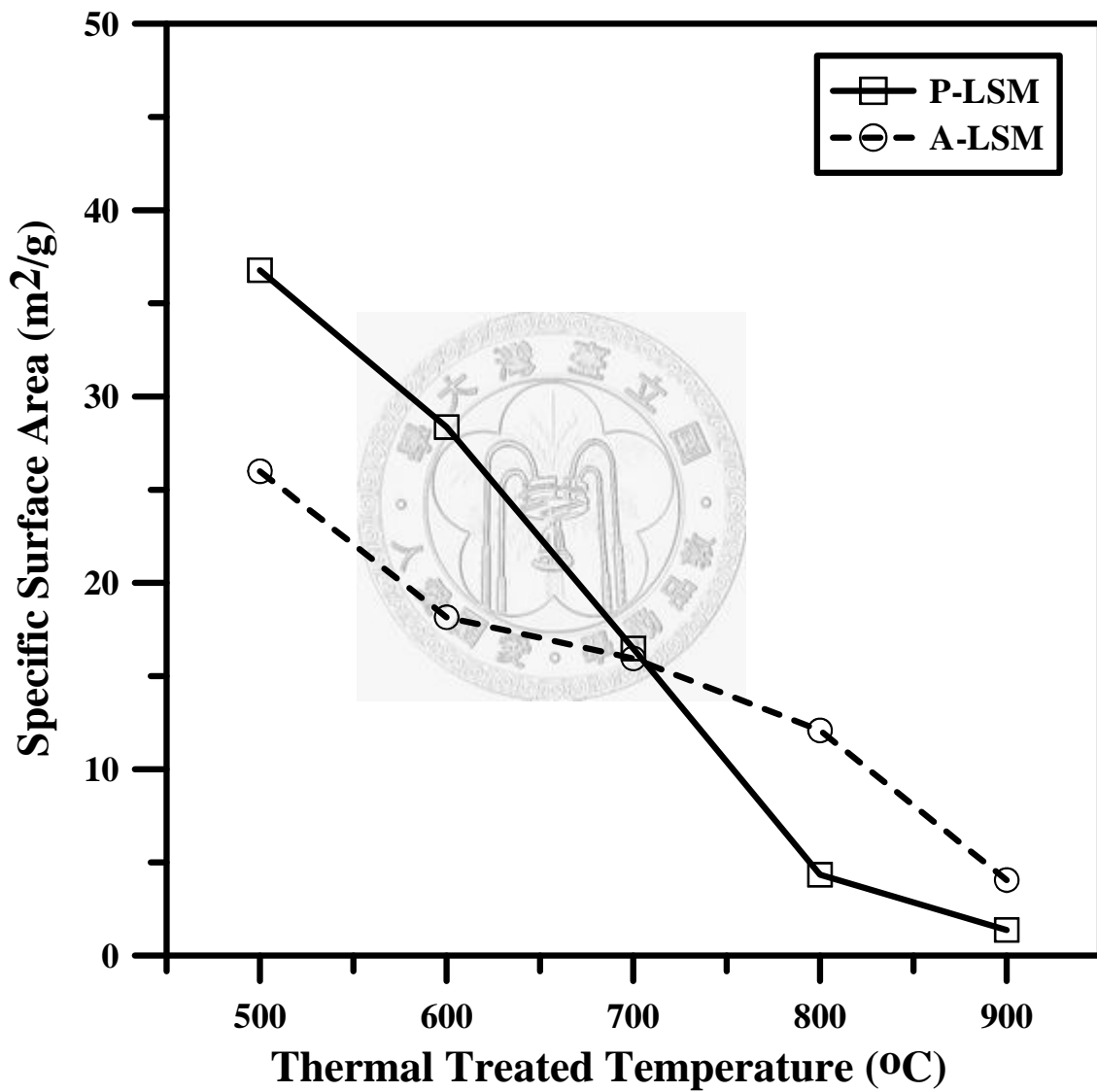
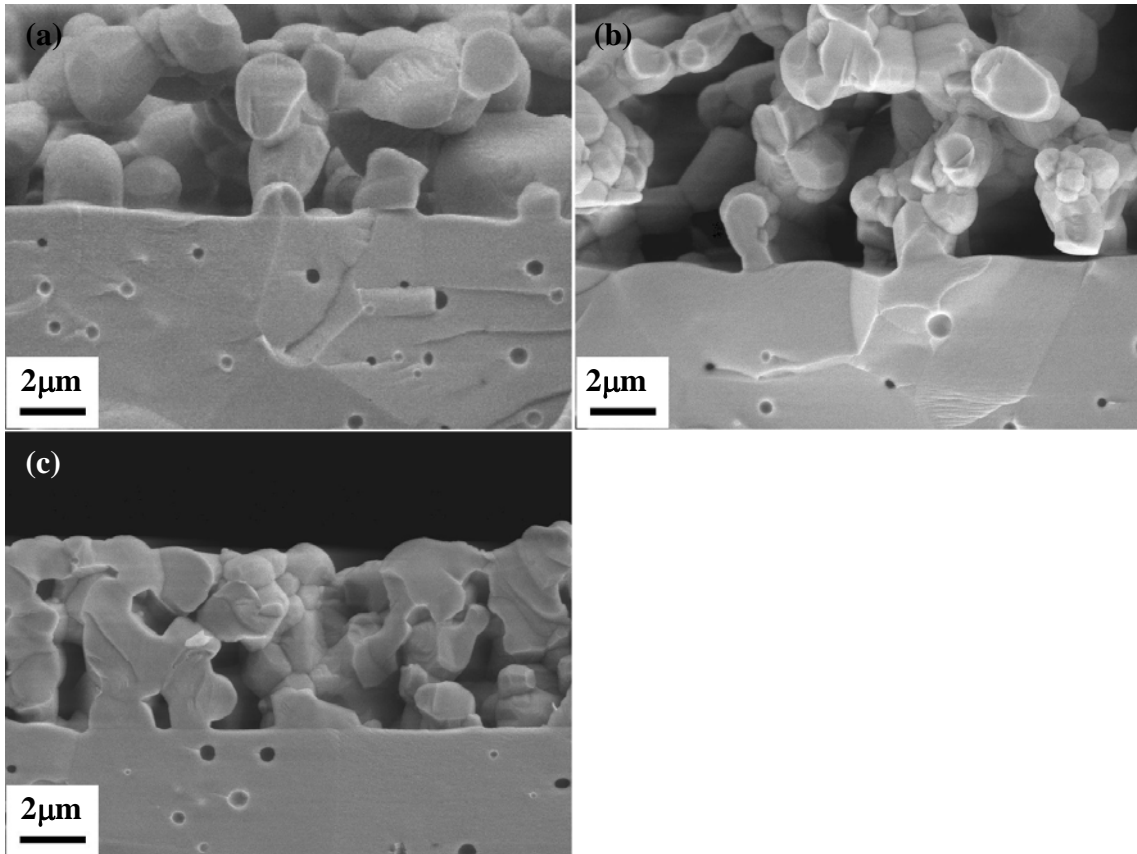
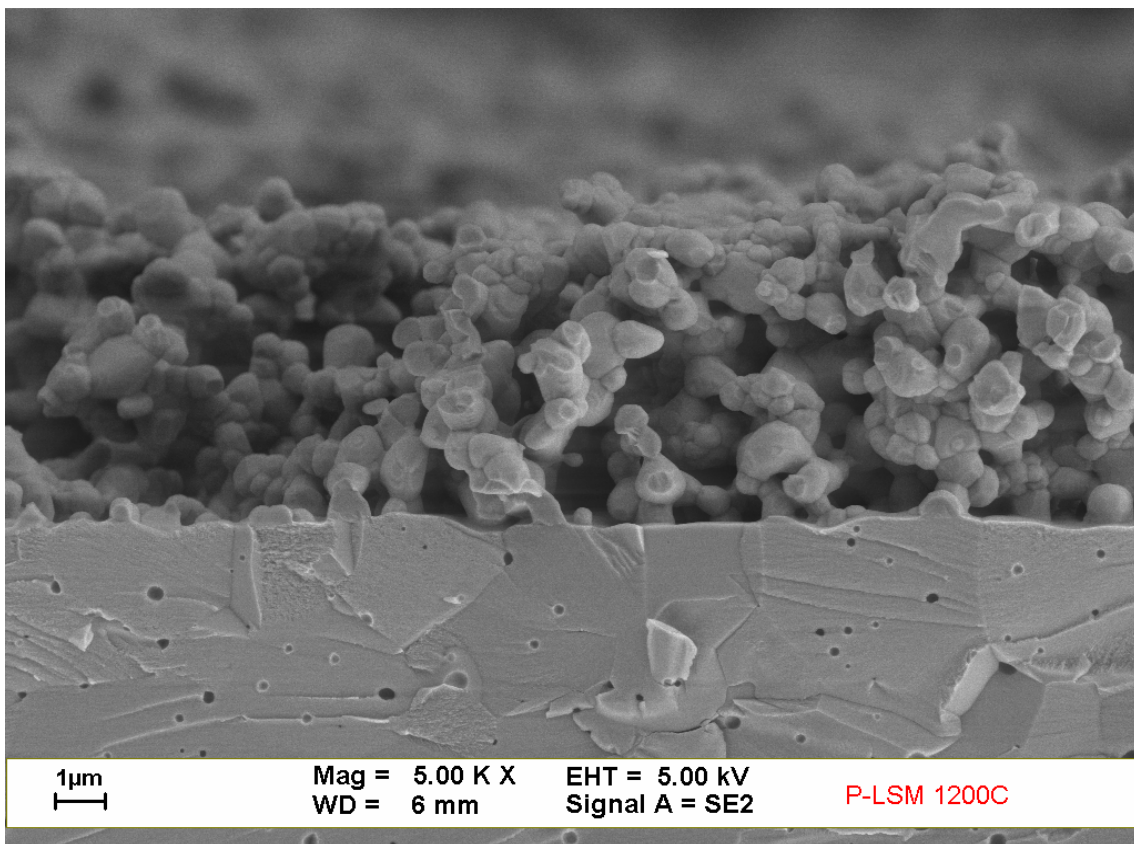


Fig. 4.23 Plot of specific surface area against thermal treated temperature of P-LSM and A-LSM.



**Fig. 4.24** SEM microstructures showing fracture surfaces of sintered (a) P-LSM-S, (b) A-LSM-S, and (c) H-LSM layers on YSZ substrates thermal treated at 1200°C for 1 hr.



**Fig. 4.25** SEM micrograph showing fracture surface of porous P-LSM layer on YSZ electrolyte thermally treated at 1200°C for 1 hr.

**Table 4.4** Characteristic length of TBP of YSZ and all the LSM thin layers calculated according to Saltykov equation

	H-LSM	P-LSM	P-LSM-S	A-LSM	A-LSM-S
$P_L$ ( $1/\mu\text{m}$ )	1.29	1.07	0.914	0.914	0.876
$L_A$ ( $\mu\text{m}/\mu\text{m}^2$ )	2.03	1.66	1.44	1.44	1.38

**Table 4.5** Carbon content of LSM powders by the treatment in specified conditions

900°C thermal treatment					
	P-LSM	P-LSM-S	A-LSM	A-LSM-S	H.C. Starck
average C (ppm)	470	212	923	825	N/A
1200°C thermal treatment					
	P-LSM	P-LSM-S	A-LSM	A-LSM-S	H.C. Starck
average C (ppm)	103	182	108	193	134

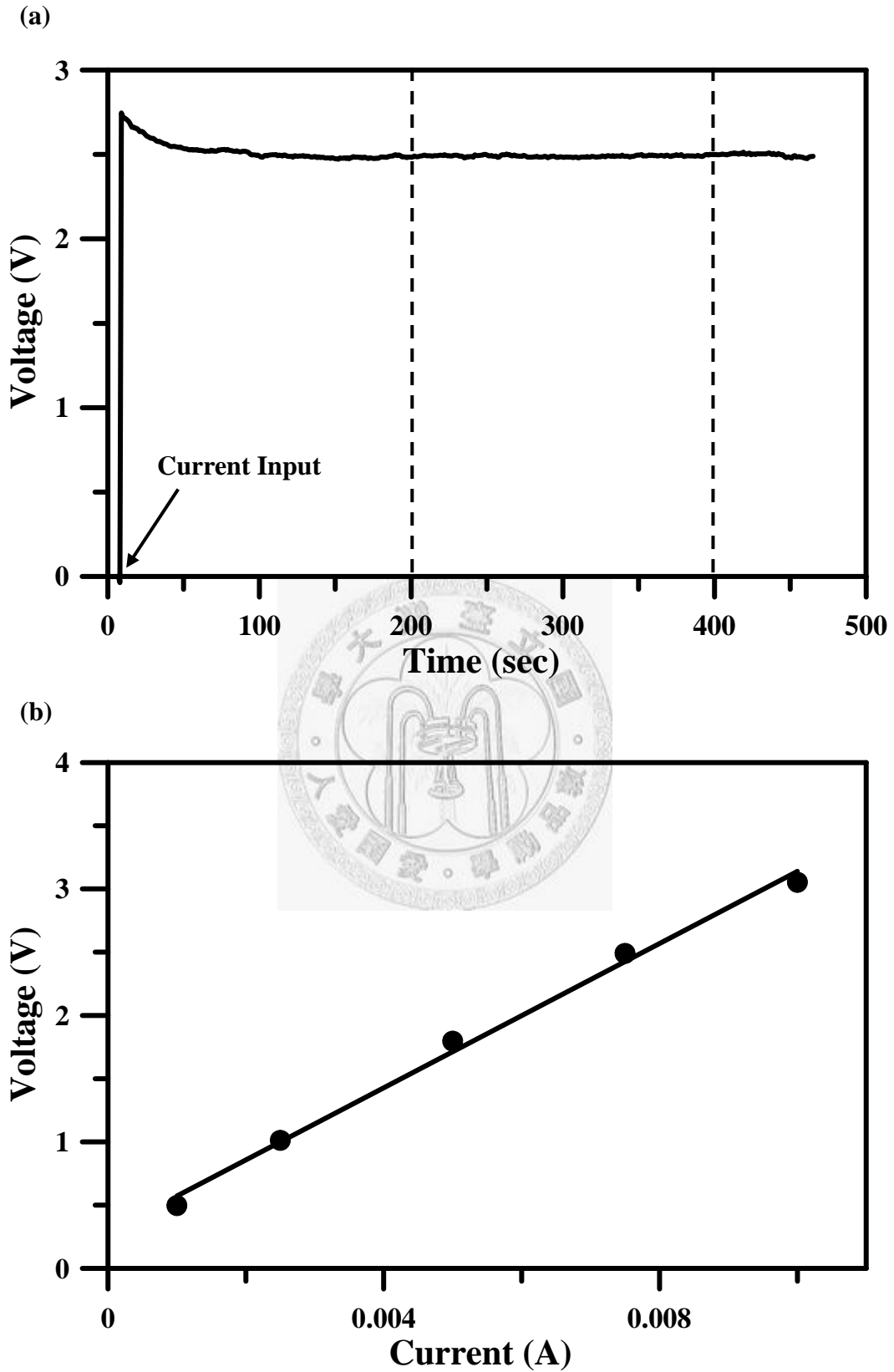


Fig. 4.26(a) Voltage curve profile with 7.5 mA current input and (b) linear I-V curve of 1200°C thermally treated A-LSM-S/YSZ half cell at 500°C.

**Table 4.6** ASR results of all the LSM layers on YSZ electrolyte thermal treated at 1200°C

ASR ( $\Omega \text{ cm}^2$ )	300°C	400°C	500°C	600°C	700°C	800°C
H-LSM	13.5k	688	82.7	28.8	7.25	N/A
P-LSM	7.12k	500	76.8	18.8	9.47	5.25
P-LSM-S	13.4k	514	84.0	16.1	11.0	6.36
A-LSM	9.28k	690	132	24.6	10.0	5.43
A-LSM-S	7.50k	516	110	15.0	9.07	5.82

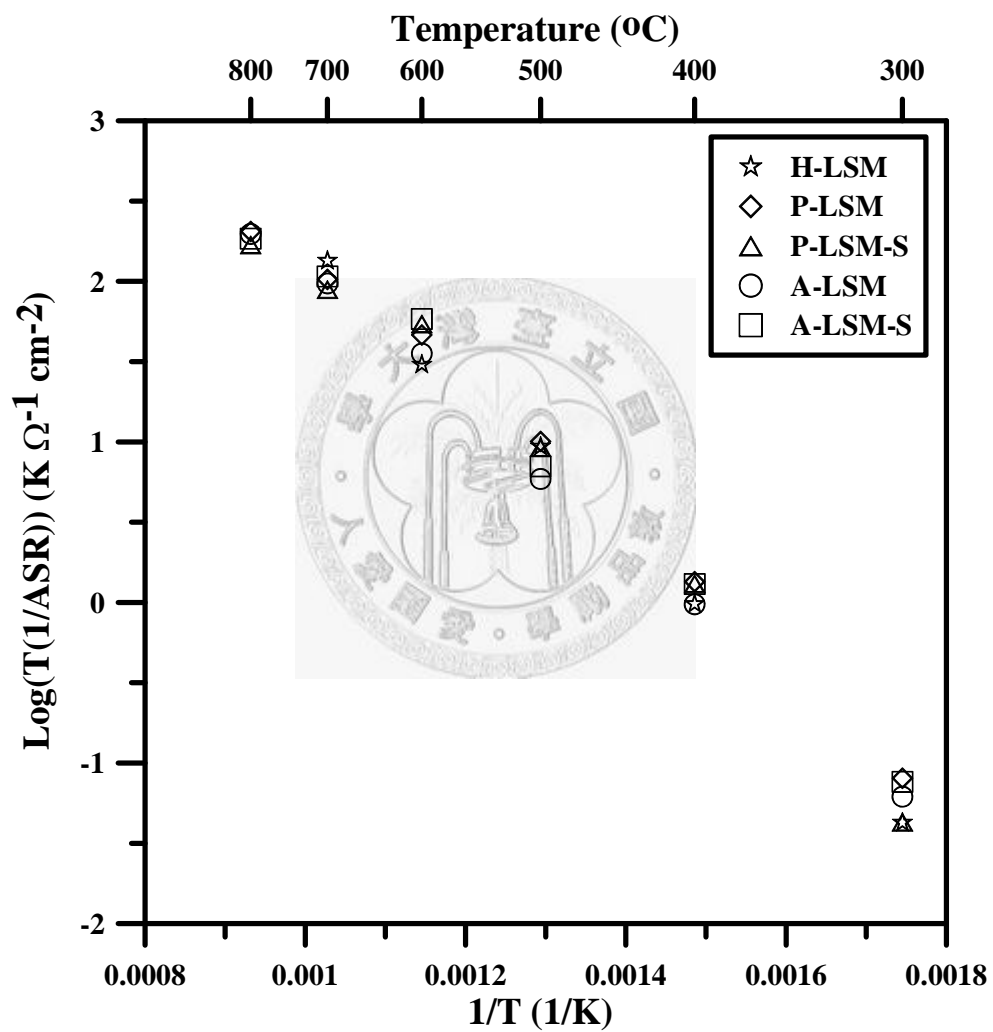
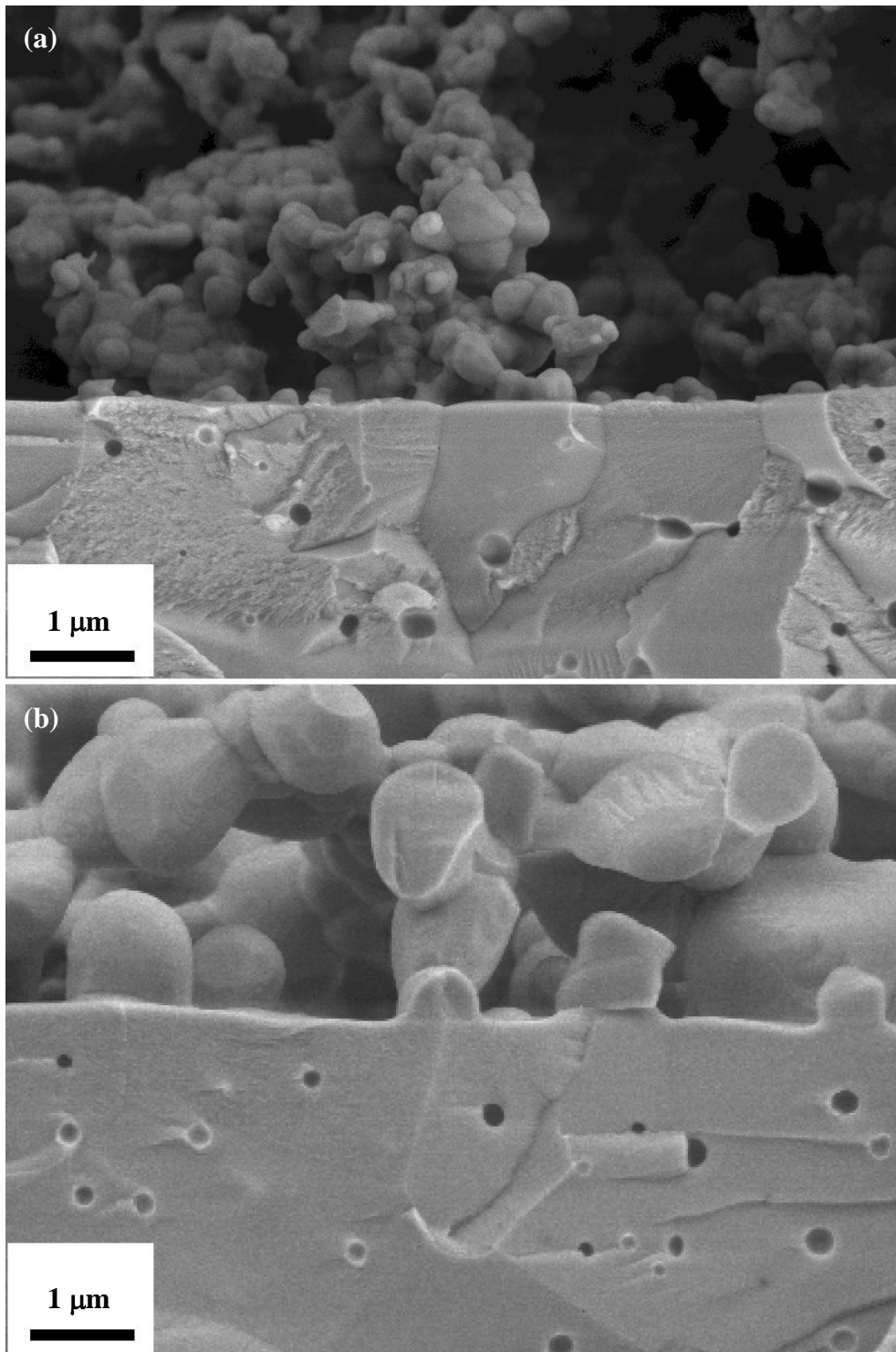


Fig. 4.27 Arrhenius plot of  $\log(T/\text{ASR})$  of various LSM layers prepared by spray coating, then thermal treating at  $1200^{\circ}\text{C}$  for 1 hr.





**Fig. 4.28** SEM micrographs showing fracture surfaces of sintered P-LSM-S layers and YSZ thermally treated at (a) 1100°C and (b) 1200°C for 1 hr.

### 4.3 Fabrication and Properties of Electrolyte Supported SOFC Single Cell

In this section, the properties of 8Y-YSZ electrolyte were discussed, including its sintering behavior and electrical property. In addition, the microstructure of electrolyte supported solid oxide fuel cell was also reported.

#### 4.3.1 Sintering Behavior and Electric Properties of 8YSZ Plate

In order to avoid the warpage of YSZ plate during sintering, sintering with gravitational load of 26 g was adopted in this study. After the sintering, the thickness of the sample shrank from 100  $\mu\text{m}$  to 75  $\mu\text{m}$ . The relative density and grain size of 8YSZ at several sintering temperatures are shown in Fig. 4.29. The relative density increases with the increase of the sintering temperature. The density of the electrolyte is higher than 99% theoretical density (T.D.), which is valid for the operation of SOFC, and could be achieved with the sintering temperature higher than 1500°C. Fig. 4.30 shows the top view images of the surface of several 8YSZ plates. The average grain size grew up to 3  $\mu\text{m}$  and 9  $\mu\text{m}$  with sintering temperature at 1500°C and 1600°C for 1 hr, respectively.

Fig. 4.31 shows the results of electrochemical impedance spectroscopy (EIS) of 1500°C sintered YSZ plate tested in static air at temperatures between 300°C and 700°C. From the literature<sup>[Minh, 1993]</sup>, the electrical conductivity of zirconia based electrolyte

system is independent of oxygen partial pressure when the oxygen partial pressure is higher than  $10^{-20}$  atm. Therefore, the electronic conductivity of the YSZ is negligible in air atmosphere condition. In Fig. 4.31(a), three semi-circles were observed on the spectrum measured at 300°C. The semi-circles of high frequency and intermediate were associated with the contribution of grain interior ( $R_g$ ) and grain boundary ( $R_b$ ), respectively. The semi-circle of lowest frequency was attributed by the resistivity of silver electrode-electrolyte interface ( $R_e$ ) [Barsoukov *et al.*, 2005]. As the testing temperature increased, the semi-circles from grain interior and grain boundary disappeared. At the temperatures higher than 600°C, only the semi-circle of electrode-electrolyte interface was observed, in which the intercept of high frequency spectrum represents the ionic impedance ( $R_i$ ). On the other hand, the ionic impedance was obtained from the addition of  $R_g$  and  $R_b$  at the temperature lower than 600°C. It can be seen that the ionic impedance of YSZ decreased with the increase of temperature from  $3700 \Omega \cdot \text{cm}^2$  (300°C) to  $3 \Omega \cdot \text{cm}^2$  (700°C), which are in the same order of ASR reported in Table 4.6.

The Arrhenius plot of ionic conductivity of 1500°C sintered YSZ plate is shown in Fig. 4.32, also comparing with the results in Yang's report [Yang *et al.*, 2003]. A slope change at 550°C, which indicated the change of conductive mechanism, was observed. The association of the defects, i.e.  $\{Y_{Zr}'V_O^{\bullet\bullet}\}^{\bullet}$ , was explained for the mechanism change. The

activation energy of migration of associated defect could be derived from the slope of the Arrhenius plot. The activation energy of YSZ plate in the temperature range of 300°C and 600°C was 109 kJ/mol, which was close to the activation energy 103 kJ/mol reported by Yang *et al.*<sup>[Yang *et al.*, 2003]</sup>.

### 4.3.2 Fabrication of Anode and Cathode Layers

LSM paste for cathode and NiO-YSZ paste for anode were screen-printed on the 1500°C sintered 8Y-YSZ plate through a 150-mesh screen with a designed square pattern (1.3 cm × 1.3 cm in dimensions). After de-binding, several sintering temperatures were conducted. Fig. 4.33 shows the fracture surfaces of the H-LSM cathode layer on YSZ plate. The higher the sintering temperature is, the higher the relative density and larger grain size of the cathode structure appear. In addition, the sintering behavior between LSM and YSZ started at the sintering temperature of 1100°C and got more obvious at higher temperature. The occurrence of interfacial sintering results in an easily diffusion of oxygen ions between LSM and YSZ, which would reduce the resistance from cathode/electrolyte interface. At the thermal treatment of 1300°C, the relatively lower relative density would lead to the concentration polarization. Therefore, 1200°C was chosen to be the suitable sintering temperature for

the single cell.

The fracture surface of LSM/YSZ/NiO-YSZ single cell sintered at 1200°C is shown in Fig. 4.34(a), which shows the fracture surface of 1500°C sintered 8YSZ electrolyte, on which submicron-sized pores (Fig. 4.34(d)) enclosed in the plate are observed. The thickness of sintered LSM cathode, NiO/YSZ anode film and YSZ are 5 μm, 8 μm and 75 μm, respectively. Figs. 4.34(b) and (c) show the top views of the LSM film and the NiO/YSZ film of the single cell. Highly porous structure of cathode and anode provides gas flowing channels for air and fuel. The cell shows the potential used as on component of SOFC.



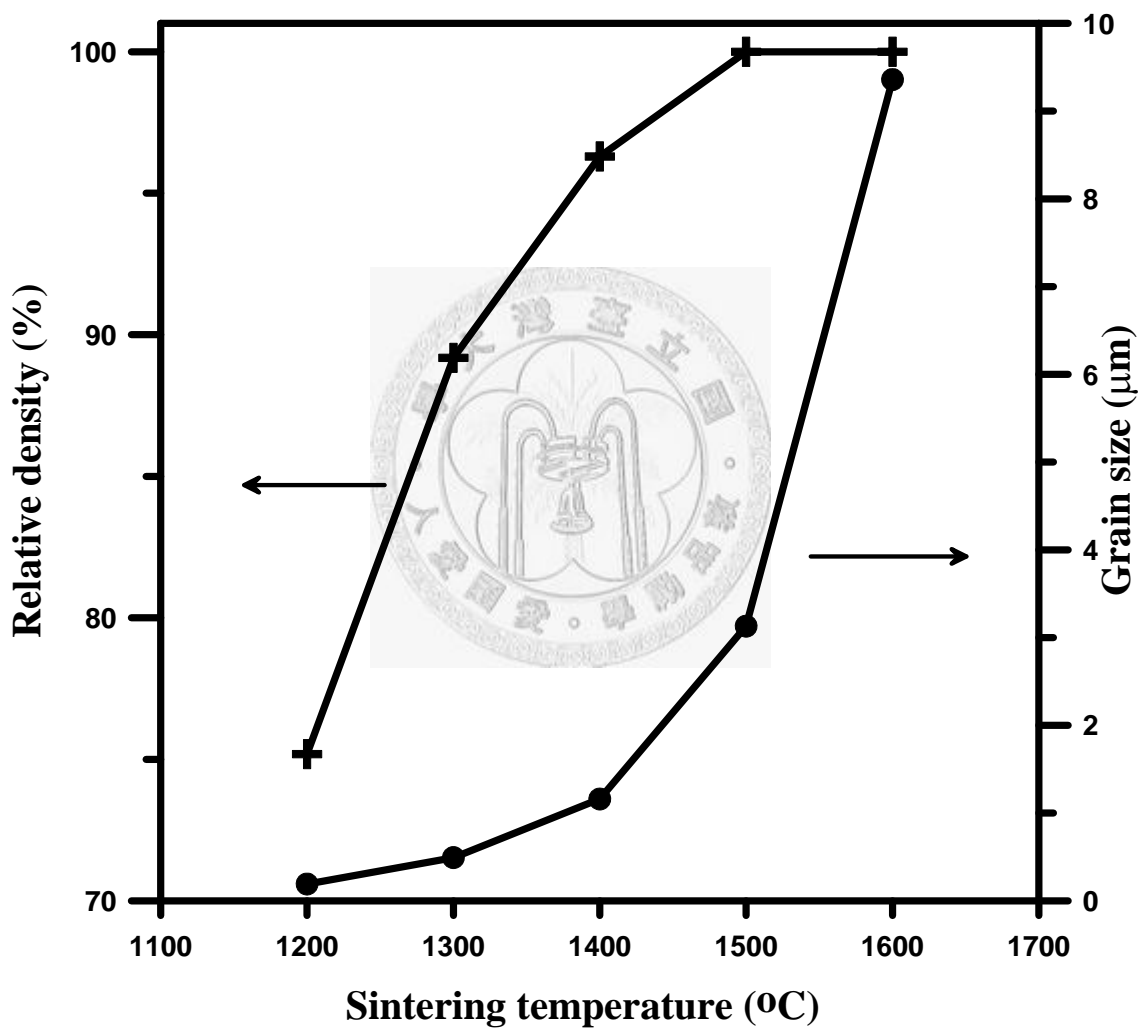
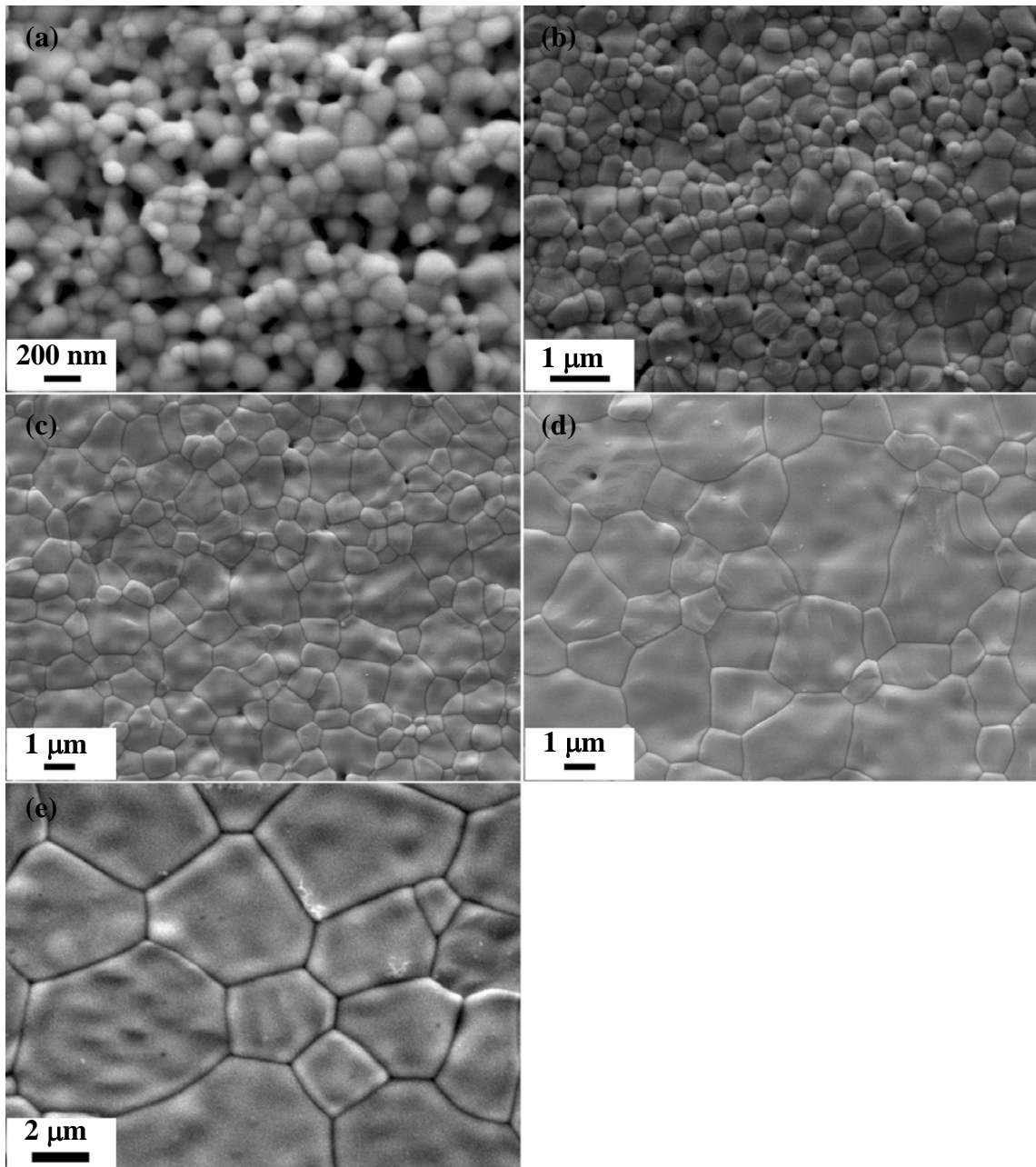


Fig. 4.29 Relative density and average grain size plotted against sintering temperature of YSZ tape.





**Fig. 4.30** SEM micrographs showing the top microstructures of 8Y-YSZ tape sintered at (a) 1200°C, (b) 1300°C, (c) 1400°C, (d) 1500°C, and (e) 1600°C for 1 hr in air.

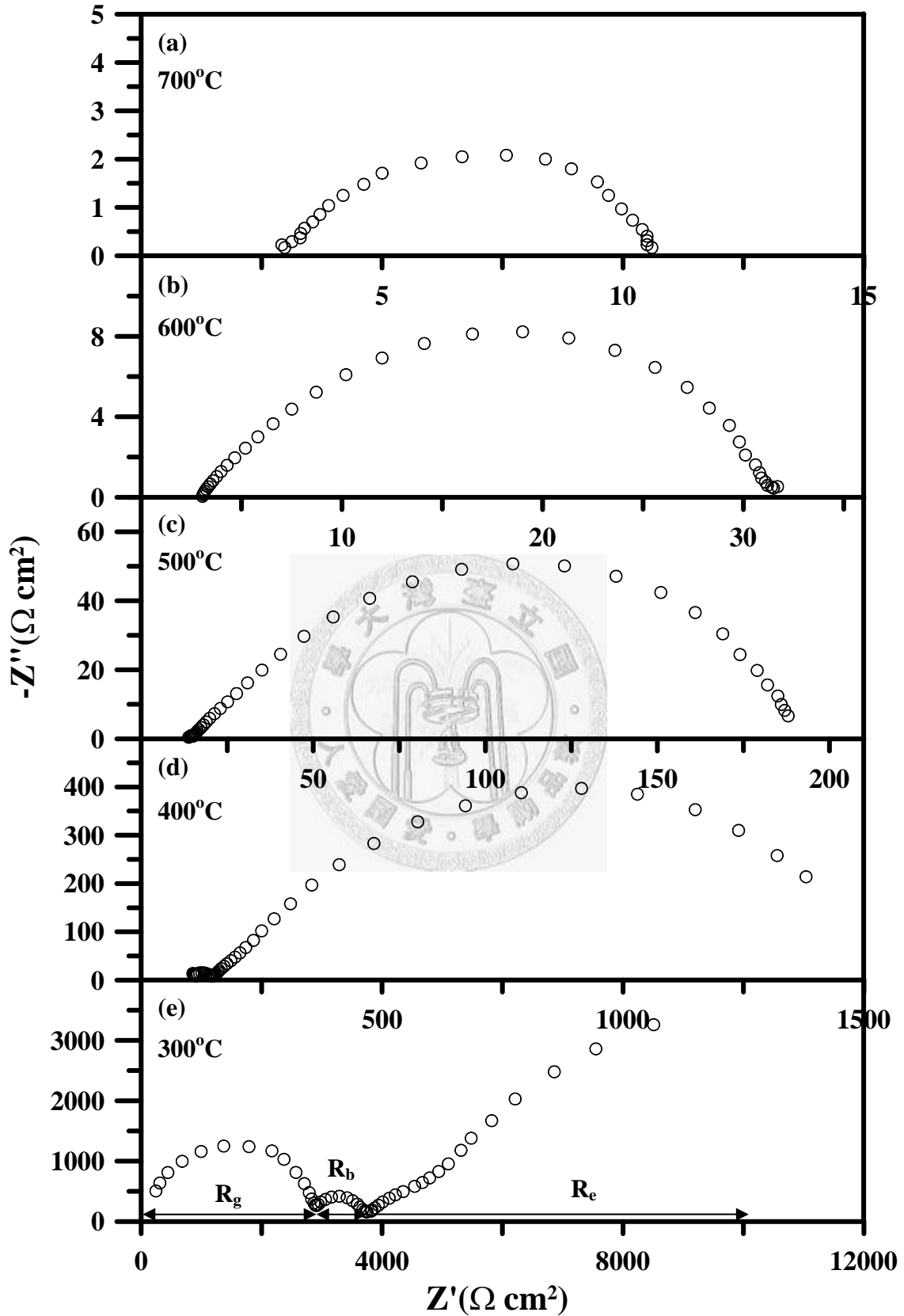


Fig. 4.31 AC impedance results of 1500°C sintered 8Y-YSZ plate in static flowing air at (a) 700°C, (b) 600°C, (c) 500°C, (d) 400°C, and (e) 300°C.



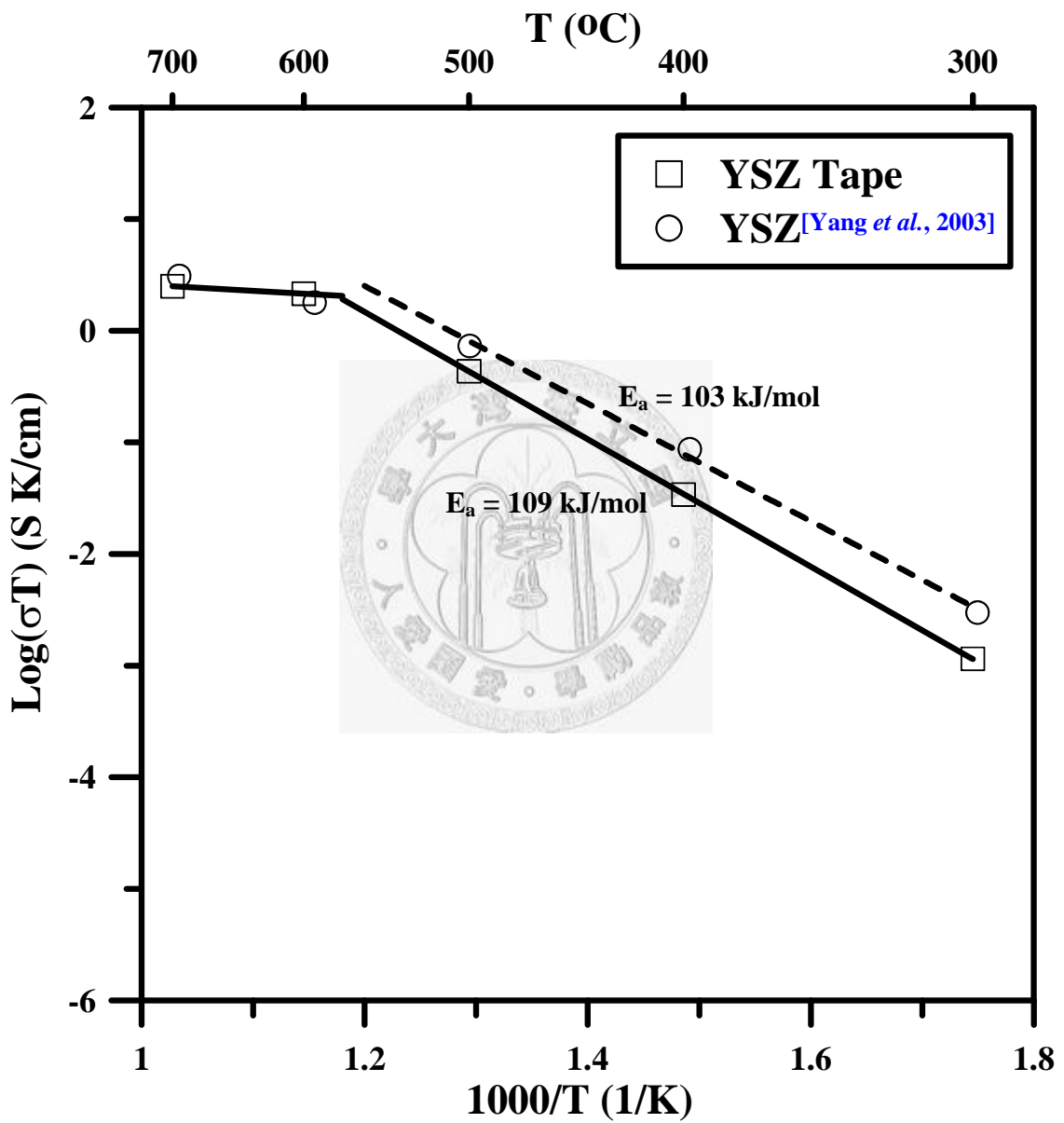
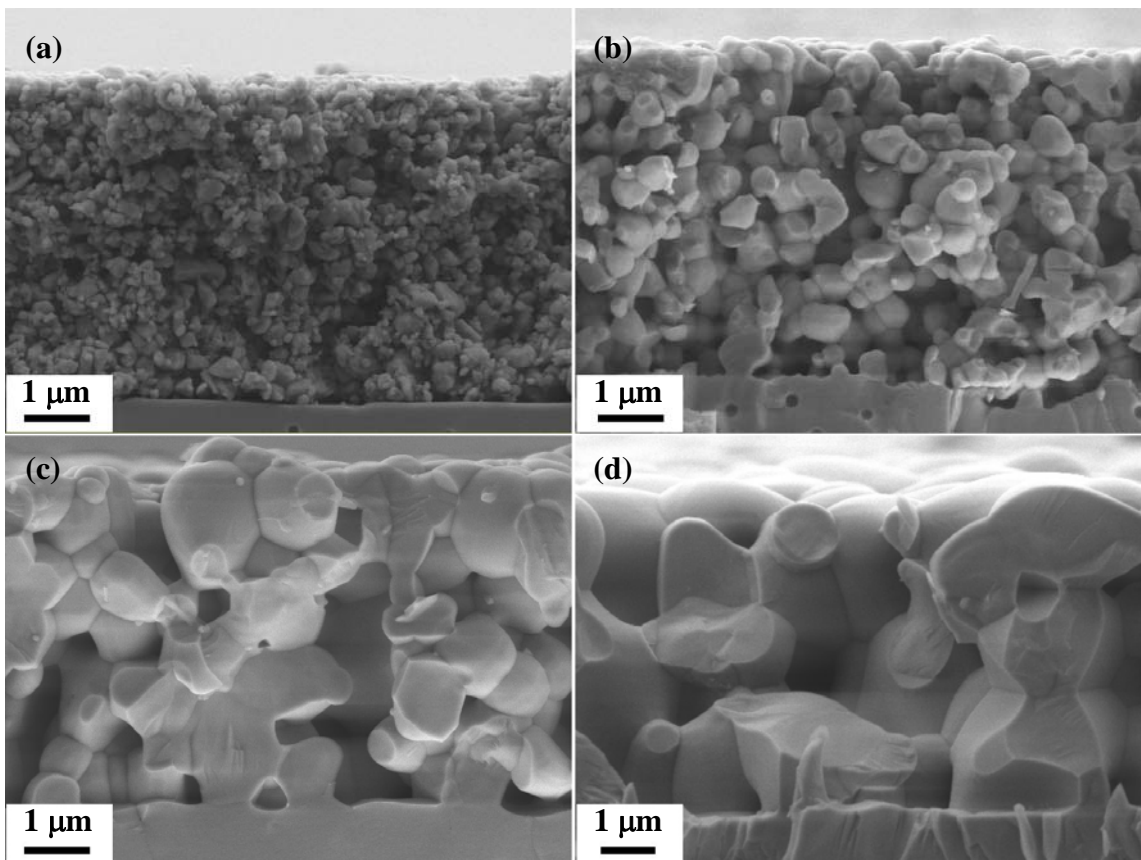


Fig. 4.32 Plot of electrical conductivity against reciprocal absolute temperature.



**Fig. 4.33** SEM microstructures of fractures of LSM/YSZ interface co-sintered at (a) 1000°C, (b) 1100°C, (c) 1200°C, and (d) 1300°C for 1 hr.

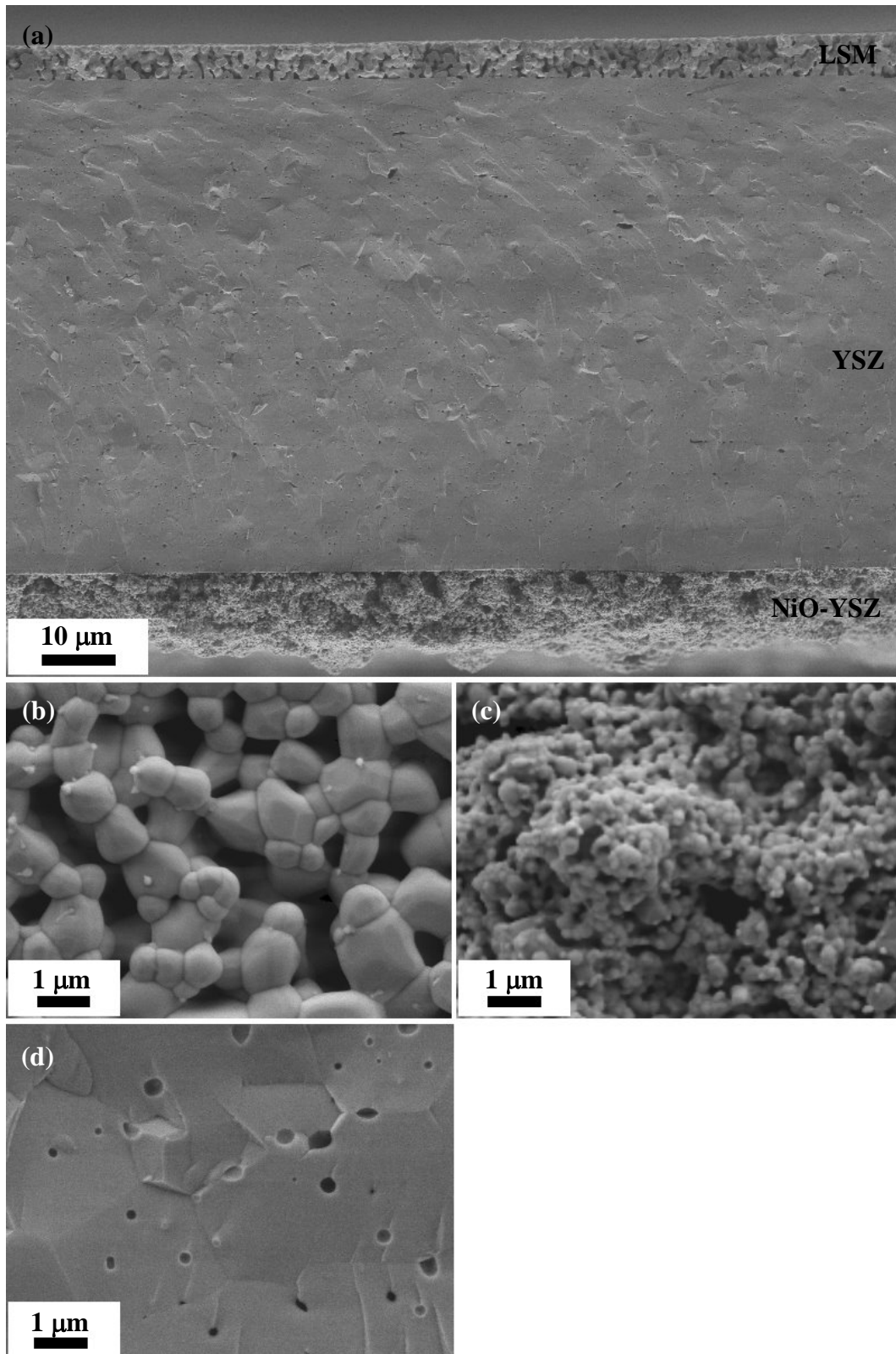


Fig. 4.34 SEM microstructures of (a) the fracture surface of LSM/YSZ/NiO-YSZ single cell final-treated at 1200°C for 1 hr, the top views of (b) LSM and (c) NiO-YSZ layers, and (d) closer-view of the fracture surface of YSZ electrolyte

## Chapter 5 Conclusions

### Properties of CeO<sub>2</sub> (GDC and SDC) Fibers

Gd<sub>2</sub>O<sub>3</sub> and Sm<sub>2</sub>O<sub>3</sub> doped ceria fibers with aspect ratio of 110 were synthesized by chemical co-precipitate method at 90°C with the addition of citric acid and sodium hydroxide. With different ratio of sodium hydroxide and citric acid, additional three types of Ce-contained precipitates were formed, including spherical colloidal particles, stick-in-bundle, and flakes.

The kinetic reaction of the fiber synthesis was analyzed by ICP-AES technology. Zero-order reaction of the fiber and stick-in-bundle synthesis was confirmed, in which the reaction rate coefficient were 1371 ppm/hr and 172 ppm/hr, respectively. With starting concentration of 0.1 m<sub>c</sub> of Ce<sup>3+</sup>, the reaction of fiber synthesis completed in less than 10 hr. Before the appearance of fiber, there were water soluble colloidal particles found in reaction bath. With calcination at temperature higher than 300°C, the cubic ceria phase formed. Crystallinity of the doped ceria fibers was identified by TEM technology.

### Properties of LSM Powders

Two LSM powders were synthesized either by sol-gel routs, including Pechini

method (P-LSM) and the method with PAA as gelling agent (A-LSM). For both cases, the LSM phase formed at calcination temperature higher than 600°C. A carbon contained phase of  $\text{La}_2\text{CO}_3$  was found in P-LSM that thermally treated at 500°C or 600°C. After 700°C calcination, pure LSM phase was obtained for both LSM powders. The quantitative analysis by SEM-EDS revealed a better chemical composition distribution and homogeneity of P-LSM powder. The microstructure, however, indicated a better grain size distribution of A-LSM due to carbon content.

Porous LSM layer with a thickness of 6  $\mu\text{m}$  was fabricated by spray coating. In order to offer enough interface strength between LSM and YSZ, the sintering temperature of LSM/YSZ half cell must be higher than 1200°C. The length of TPB was about 1.5  $\mu\text{m}/\mu\text{m}^2$  after the 1200°C thermal treatment. The residual carbon content was successfully reduced by careful control of thermal treatment procedure for P-LSM with thermal treatment at 900°C. After the 1200°C thermal treatment, the residual carbon content in all the LSM powders was reduced to less than 200 ppm. The ASR between LSM and YSZ is low, but does not show a strong correlation with the residual carbon..

### **Fabrication of Electrolyte Supported SOFC Single Cell**

A dense 8Y-YSZ electrolyte plate with thickness of 75  $\mu\text{m}$  could be obtained by

1500°C sintering. Its activation energy for the diffusion of oxygen was 109 kJ/mole.

Through screen printing, porous LSM cathode layer with 5  $\mu\text{m}$  in thickness and

NiO/YSZ anode in a thickness of 8  $\mu\text{m}$  could be fabricated on the YSZ electrolyte plate

by 1200°C sintering.



## References

- I. Abrahams, A. Kozanecka-Szmigiel, F. Krok, W. Wrobel, S.C.M. Chan, and J.R. Dygas, "Correlation of defect structure and ionic conductivity in  $\delta$ -phase solid solutions in the  $\text{Bi}_3\text{NbO}_7$ - $\text{Bi}_3\text{YO}_6$  system," *Solid State Ionics*, 177, 1761-65 (2006)
- A. Abreu Jr., S. M. Zanetti, M. A. S. Oliveira, and G. P. Thim, "Effect of urea on lead zirconate titanate- $\text{Pb}(\text{Zr}_{0.52}\text{Ti}_{0.48})\text{O}_3$ -nanopowders synthesized by the Pechini method," *J. Eur. Ceram. Soc.*, 25, 743-8 (2005)
- A-M. Azad, T. Matthews, and J. Swary, "Processing and characterization of electrospun  $\text{Y}_2\text{O}_3$ -stabilized  $\text{ZrO}_2$  (YSZ) and  $\text{Gd}_2\text{O}_3$ -doped  $\text{CeO}_2$  (GDC) nanofibers," *Materials science and engineering B*, 123, 252-8 (2005)
- G. B. Balazs, and R. S. Glass, "ac impedance studies of rare earth oxide doped ceria," *Solid State Ionics*, 76, 155-62 (1995)
- E. Barsoukov and J. R. Macdonald, *Impedance Spectroscopy Theory, Experiment, and Applications 2<sup>nd</sup> edition*, Wiley-Interscience, p.170-1, 2005
- F. Chen and M. Liu, "Preparation of yttria-stabilized zirconia (YSZ) films on  $\text{La}_{0.85}\text{Sr}_{0.15}\text{MnO}_3$  (LSM) and LSM-YSZ substrates using an electrophoretic deposition (EPD) process," *J. Eur. Ceram. Soc.*, 21, 127-34 (2001)
- K. Chen, Z. Lü, N. Ai, Z. Chen, J. Hu, X. Huang, and W. Su, "Effect of SDC-impregnated LSM cathodes on the performance of anode-supported YSZ films for SOFCs," *J. of Power Sources*, 167, 84-9 (2007)
- Y.-Y. Chen, and W.-C. J. Wei, "Processing and characterization of ultra-thin yttria-stabilized zirconia (YSZ) electrolytic films for SOFC," *Solid State Ionics*, 177, 351-7 (2006)
- Y.-M. Chiang, D. P. Birnie III, and W. D. Kingery, *Physical Ceramics Principles for Ceramic Science and Engineering*, John Wiley & Sons, Inc., 26, 1997
- Y.-M. Chiang, D. P. Birnie III, and W. D. Kingery, *Physical Ceramics Principles for Ceramic Science and Engineering*, John Wiley & Sons, Inc., 136-9, 1997
- B. D. Cullity and S. R. Stock, *Elements of X-Ray Diffraction, 3rd edition*, Prentice Hall, 167-71, 2001
- M. Gaudon, C. Laberty-Robert, F. Ansart, P. Stevens, and A. Rousset, "Preparation and characterization of  $\text{La}_{1-x}\text{Sr}_x\text{MnO}_{3+\delta}$  ( $0 \leq x \leq 0.6$ ) powder by sol-gel processing," *Solid State Sciences*, 4, 125-33 (2002)
- X. Guo, "Physical origin of the intrinsic grain-boundary resistivity of stabilized-zirconia: Role of the space-charge layers," *Solid State Ionics*, 81, 235-42 (1995)
- X. Guo, E. Vasco, S. Mi, K. Szot, E. Wachsman, and R. Waser, "Ionic conduction

- in zirconia films of nanometer thickness,” *Acta Materialia*, 53, 5161-6 (2005)
- X. Guo, S. Wilfried, and M. Joachim, “Blocking Grain Boundaries in Yttria-Doped and Undoped Ceria Ceramics of High Purity,” *J. Am. Ceram. Soc.*, 86 [1] 77-87 (2003)
  - A. Hagiwara, N. Hobara, K. Takizawa, K. Sato, H. Abe, and M. Naito, “Microstructure control of SOFC cathodes using the self-organizing behavior of LSM/ScSZ composite powder material prepared by spray pyrolysis,” *Solid State Ionics*, 178, 1123-34 (2007)
  - A. Hagiwara, N. Hobara, K. Takizawa, K. Sato, H. Abe, and M. Naito, “Preparation of LSM/ScSZ composite powder materials by spray pyrolysis for the pre-fabrication of SOFC cathodes,” *Solid State Ionics*, 178, 1552-62 (2007)
  - T. P. Harrigan and R. W. Mann, “Characterization of microstructural anisotropy in orthotropic materials using a second rank tensor,” *J. Mater. Sci.*, 19, 761-7 (1984)
  - D. C. Harris, *Quantitative Chemical Analysis (Fifth Edition)*, W. H. Freeman and Company, 74-81, 2001
  - W. Huang, P. Shuk, and M. Greenblatt, “Hydrothermal Synthesis and Properties of  $Ce_{1-x}Sm_xO_{2-x/2}$  and  $Ce_{1-x}Ca_xO_{2-x}$  Solid Solutions,” *Chem. Mater.*, 9, 2240-5 (1997)
  - H.-R. Hsu, *Fabrication and characterization of LSM electrode*, MS thesis, NTU (2003)
  - W. P. Hsu, L. Rönquist, and Egon Matijević, “Preparation and Properties of Monodispersed Colloidal Particles of Lanthanide Compounds. 2. Cerium(IV),” *Langmuir*, 4, 31-7 (1988)
  - H. J. Hwang, J. Moon, M. Awano, and K. Maeda, “Sol-gel route to porous lanthanum cobaltite ( $LaCoO_3$ ) thin films,” *J. Am. Ceram. Soc.*, 83 [11] 2852-4
  - H. Inaba, H. Tagawa, “Ceria-based solid electrolytes,” *Solid State Ionics*, 83, 1-16 (1996)
  - G.-B. Jung, T.-Jen. Huang, and C.-L. Chang, “Effect of temperature and dopant concentration on the conductivity of samaria-doped ceria electrolyte,” *J. Solid State Electrochem*, 6, 225-30 (2002)
  - J.A. Kilner, “Fast oxygen transport in acceptor doped oxides,” *Solid State Ionics*, 129, 13-23 (2000)
  - W. D. Kingery, H. K. Bowen, and D. R. Uhlmann, *Introduction to Ceramics (2<sup>nd</sup> Edition)*, Wiley, p.416-7, 1976
  - T. Kudo, and H. Obayashi, “Mixed Electrical Conduction in the Fluorite-Type  $Ce_{1-x}Gd_xO_{2-x/2}$ ,” *J. Electrochem. Soc.*, 123, 415-9 (1976)



- J. H. Kuo and H. U. Anderson, "Oxidation-Reduction Behavior of Undoped and Sr-Doped LaMnO<sub>3</sub>: Defect Structure, Electrical Conductivity, and Thermoelectric Power," *J. Solid State Chem.*, 87, 55-63 (1990)
- L. Minervini, M. O. Zacate, and R. W. Grimes, "Defect cluster formation in M<sub>2</sub>O<sub>3</sub>-doped CeO<sub>2</sub>," *Solid State Ionics*, 116, 339-49 (1999)
- N. Q. Minh, "Ceramic Fuel Cells," *J. Am. Ceram. Soc.*, 76 [3] 563-88 (1993)
- M. Mogensen, N. M. Sammes, and G. A. Tompsett, "Physical, chemical and electrochemical properties of pure and doped ceria," *Solid State Ionics*, 129, 63-94 (2000)
- M. Mori, Y. Hiei, T. Yamamoto, and H. Itoh, "Lanthanum Alkaline-Earth Manganites as a Cathode Material in High-Temperature Solid Oxide Fuel Cells," *J. Electrochem. Soc.*, 146 [11] 4041-7 (1999)
- M. Ohnuki, K. Fujimoto, and S. Ito, "Preparation of high-density La<sub>0.90</sub>Sr<sub>0.10</sub>Ga<sub>1-y</sub>Mg<sub>y</sub>O<sub>3-δ</sub> (y=0.20 and 0.30) oxide ionic conductors using HIP," *Solid State Ionics*, 177, 1729-32 (2006)
- M. J. L. Østergård, C. Clausen, C. Bagger, and M. Mogensen, "Manganite-Zirconia Composite Cathode for SOFC: Influence of Structure and Composition," *Electrochim Acta*, 40 [12] 1971-81 (1995)
- J. W. Patterson, "Conduction Domains for Solid Electrolytes," *J. Electrochem. Soc.*, 118, 1033-9 (1971)
- M. Pechini, "Method of Preparing Lead and Alkaline-Earth Titanates and Niobates and Coating Method Using The Same to Form A Capacitor," U.S. Pat. No. 3330697 (1967)
- R. Peng, C. Xia, Q. Fu, G. Meng, and D. Peng, "Sintering and electrical properties of (CeO<sub>2</sub>)<sub>0.8</sub>(Sm<sub>2</sub>O<sub>3</sub>)<sub>0.1</sub> powders prepared by glycine-nitrate process," *Materials Letters*, 56, 1043-7 (2002)
- S. Pignard, H. Vincent, J. P. Sénateur, and P. H. Giauque, "Chemical vapor deposition and structural study of La<sub>0.8</sub>MnO<sub>3-δ</sub> thin films," *Thin Solid Films*, 347, 161-6 (1999)
- F. W. Poulsen, "Defect chemistry modeling of oxygen-stoichiometry, vacancy concentrations, and conductivity of (La<sub>1-x</sub>Sr<sub>x</sub>)<sub>y</sub>MnO<sub>3+δ</sub>," *Solid State Ionics*, 129, 145-62 (2000)
- J. M. Ralph, J. Przydatek, J. A. Kilner, and T. Seguelong, "Novel Doping Systems in Ceria," *Ber. Bunsenges. Phys. Chem.*, 101, 1403-7 (1997)
- J. I. M. Rupp, A. Infortuna, and L. J. Gauckler, "Thermodynamic Stability of Gadolinia-Doped Ceria Thin Film Electrolytes for Micro-Solid Oxide Fuel Cells," *J.*

- Am. Ceram. Soc.*, 90 [6] 1792-7 (2007)
- R. D. Shannon, "Revised Effective Ionic Radii and Systematic Studies of Interatomic Distances in Halides and Chalcogenides," *Acta Cryst.*, A32, 751-67 (1976)
  - A. Sin, Yu. Dubitsky, A. Zaopo, A.S. Arico, L. Gullo, D. La Rosa, S. Siracusano, V. Antonucci, C. Oliva, and O. Ballabio, "Preparation and sintering of  $Ce_{1-x}Gd_xO_{2-x/2}$  nanopowders and their electrochemical and EPR characterization," *Solid State Ionic*, 175, 361-6 (2004)
  - S. C. Singhal, and K. Kendall, *High Temperature Solid Oxide Fuel Cells: Fundamentals, Design and Applications*, Elsevier Science, 81-94, 2003
  - S. C. Singhal, and K. Kendall, *High Temperature Solid Oxide Fuel Cells: Fundamentals, Design and Applications*, Elsevier Science, 91, 2003
  - S. C. Singhal, and K. Kendall, *High Temperature Solid Oxide Fuel Cells: Fundamentals, Design and Applications*, Elsevier Science, p.229-50, 2003
  - S. C. Singhal, and K. Kendall, *High Temperature Solid Oxide Fuel Cells: Fundamentals, Design and Applications*, Elsevier Science, 238, 2003
  - S. C. Singhal, "Advances in solid oxide fuel cell technology," *Solid State Ionics*, 135, 305-13 (2000)
  - S. J. Skinner, and J. A. Kilner, "Oxygen ion conductors," *Materials Today*, 6 [3] 30-7 (2003)
  - T. Suzuki, I. Kosacki, and H. U. Anderson, "Microstructure-electrical conductivity relationships in nanocrystalline ceria thin films," *Solid State Ionics*, 151, 111-21 (2002)
  - H. L. Tuller, and A. S. Nowick, "Doped Ceria as a Solid Oxide Electrolyte," *J. Electrochem. Soc.*, 2, 255-9 (1975)
  - U.S. Department of Energy, Office of Fossil Energy, and National Energy Technology Laboratory, *Fuel Cell Handbook (seventh Edition)*, EG&G Technical Services, Inc., p.1-12, 2004
  - J. A. M. van Roosmalen, P. van Vlaanderen, and E. H. P. Cordfunke, "Phases in the Perovskite-Type  $LaMnO_{3+\delta}$  Solid Solution and the  $La_2O_3$ - $MnO_3$  Phase Diagram," *J. Solid State Chem.*, 114, 516-23 (1995)
  - Y. Wang, T. Mori, J-G. Li, and Y. Yajima, "Low-temperature fabrication and electrical property of 10 mol%  $Sm_2O_3$ -doped  $CeO_2$  ceramics," *Science and Technology of Advanced Materials*, 4, 229-38 (2003)
  - H. Xu, D-H. Qin, Z. Yang, and H-L Li, "Fabrication and characterization of highly ordered zirconia nanowire arrays by sol-gel template method," *Mater. chem. phys.*,

- 80, 524-8 (2003)
- H. Yahiro, Y. Eguchi, K. Eguchi, and H. Aria, "Oxygen ion conductivity of ceria-samarium oxide system," *J. Appl. Electrochem.*, 18, 527-31 (1988)
  - H. Yahiro, Y. Eguchi, K. Eguchi, and H. Arai, "Oxygen ion conductivity of the ceria-samarium oxide system with fluorite structure," *J. Appl. Electrochem.*, 18, 527-31 (1988)
  - H. Yahiro, T. Ohuchi, K. Eguchi, and H. Arai, "Electrical properties and microstructure in the system ceria-alkaline earth oxide," *J. Mater. Sci.*, 23, 1036-41 (1988)
  - J. Yan, Z. Hou, and K.-L. Choy, "The electrochemical properties of LSM-based cathodes fabricated by electrostatic spray assisted vapour deposition," *J. Power Sources*, 180, 373-9 (2008)
  - C.-C. T. Yang, *Processing and Characterization of High Temperature Interfacial Reactions of Electrolytic Ceramics and Electrodes of Planar Solid Oxide Fuel Cells (SOFCs)*, PhD thesis, NTU (2003)
  - C-C. T. Yang, W-C. J. Wei, and A. Roosen, "Electrical conductivity and microstructures of  $\text{La}_{0.65}\text{Sr}_{0.3}\text{MnO}_3$ -8 mol% yttria-stabilized zirconia," *Mater. Chem. phys.*, 81, 132-42 (2003)
  - X. Yang, C. Shao, Y. Liu, R. Mu, and H. Guan, "Nanofibers of  $\text{CeO}_2$  via an electrospinning technique," *Thin solid films*, 478, 228-31 (2005)
  - H.-C. Yu and K.-Z. Fung, "Electrode properties of  $\text{La}_{1-x}\text{Sr}_x\text{CuO}_{2.5-\delta}$  as new cathode materials for intermediate-temperature SOFCs," *J. Power Sources*, 133, 162-8 (2004)
  - S. Zha, C. Xia, and G. Meng, "Effect of Gd (Sm) doping on properties of ceria electrolyte for solid oxide fuel cells," *J. Power Sources*, 115, 44-8 (2003)
  - H. B. Zhang, and M. J. Edirisinghe, "Electrospinning Zirconia Fiber From a Suspension," *J. Am. Ceram. Soc.*, 89 [6] 1870-75 (2006)
  - T. S. Zhang, J. Ma, H. Cheng, and S.H. Chan, "Ionic conductivity of high-purity Gd-doped ceria solid solutions," *Mater. Res. Bull.*, 41, 563-8 (2006)
  - X. Zhang, M. Robertson, C. Deêes-Petit, W. Qu, O. Kesler, R. Maric, and D. Ghosh, "Internal shorting and fuel loss of a low temperature solid oxide fuel cell with SDC electrolyte," *J. Power Sources*, 164, 668-77 (2007)
  - K. Zhou, X. Wang, X. Sun, Q. Peng, and Y. Li, "Enhanced catalytic activity of ceria nanorods from well-defined reactive crystal planes," *J. catal.*, 229, 206-12 (2005)